POLITECNICO MILANO 1863

MASTER THESIS

Multibody parafoil-payload model for SpaceRider trajectory and inflation loads analysis

Author:
Niccolò GLOUCHTCHENKO
858443

Supervisor:
Dr. Michèle LAVAGNA
TAS-I advisors:
Ing. Antonio SALUZZI
Ing. Cosimo CHIARELLI

A thesis submitted in fulfillment of the requirements for the degree in Space Engineering

in the

Dipartimento di scienze e tecnologie aerospaziali

in collaboration with

Thales Alenia Space Italia

July 4, 2018

POLITECNICO DI MILANO

Abstract

Dipartimento di scienze e tecnologie aerospaziali

Space Engineering

Multibody parafoil-payload model for SpaceRider trajectory and inflation loads analysis

by Niccolò GLOUCHTCHENKO

Parafoils have been of great interest for space and military applications. Their higher lift-to-drag ratio w.r.t ballistic parachutes allows to save mass and volume maintaining the same vertical touch-down velocity. The possibility to control the system, pulling the suspension lines, allows also to reduce the landing dispersion and to counter-act the wind disturbance. These are some of the reasons why in the aerodynamic decelerator system of SpaceRider a parafoil stage was selected.

The present work shows the parafoil-payload model developed in the frame of the SpaceRider program. The model represents a system consisting of a parafoil and a payload as two separate rigid bodies both with 6 DoFs (3 rigid rotations and 3 rigid translations). The representation is performed through time-domain state-space model. Particular care is posed on the definition of the model validity limits and its usage within them.

The main attractive feature of the model is the inflation loads analysis, useful to check whether the design requirements imposed by the system are met or not. The classical semi-empirical methods are coupled with a more complex dynamic (12 DoFs instead of 3) to have a more accurate representation of the inflation loads (especially during the pitch-down motion at cells inflation). The effect on the inflation analysis of some parameters (as the C_{m_q}) is investigated and the importance of some of them is outlined to perform the final design of the canopy. The possibility to optimize the reefing technique for parafoil is also analyzed, reducing as much as possible the inflation loads for a single stage reefing technique.

A small overview of the GNC system is also given. The guidance in the XY plane is a classical way-points T-based approach with a sine control law. Particular emphasis is given to the longitudinal control through the development of a non-linear Lyapunov stable rigging angle control, thus allowing to reduce the landing error during the terminal guidance phase. The GNC robustness is checked imposing navigational errors, winds disturbances (gusts and turbulence) and limitations in the control action.

The model developed is suitable to design the aerodynamic decelerator system (canopy, reefing strategy, connection lines) and the GNC system. Due to its high-fidelity it can be also used for validation purposes.

Acknowledgements

Questa tesi rappresenta il conseguimento della laurea specialistica in ingegneria spaziale, il traguardo di un percorso durato anni che non è la fine quanto l'inizio di un'altra eccitante esperienza. Tutto ciò non è ovviamente solo merito mio ma anche delle persone che mi hanno supportato e mi sono state accanto in tutti questi anni.

Dapprima vorrei ringraziare le persone che hanno reso possibile la mia esperienza di tesi in azienda: la mia relatrice Michèle Lavagna e i miei tutors aziendali Antonio Saluzzi e Cosimo Chiarelli. Sono stati guide preziose che mi hanno sempre spronato con i loro consigli affinché facessi del mio meglio in questo lavoro di tesi; mi hanno inoltre permesso di realizzare una tesi che non fosse propriamente incentrata sull'ambito spaziale così da conservare la mia vocazione di ingegnere sia spaziale che aeronautico.

Un ringraziamento speciale va ovviamente ai miei genitori che hanno sempre assecondato i miei sogni e le mie vocazioni, permettendomi di diventare l'uomo che sono adesso: pronto a dare il 110% per i propri sogni e obbiettivi.

Non si può nemmeno trascurare il contributo della mia sorellona Giulia che con la sua esperienza e il suo esempio mi ha mostrato la via da seguire. Mi ha inoltre sempre strappato un sorriso anche nei momenti più bui di questi anni ed è sempre stata una persona con cui potersi confidare senza paura di pregiudizi.

Un'enestimabile fonte di gioia e tranquillità è stata la mia ragazza Caterina. Lei è sempre stata paziente con me, mi ha sempre fornito supporto e incoraggiamento, anche se c'erano 150 km a separarci è come se fosse sempre stata al mio fianco anche mentre ero al PC in azienda.

Mi sento di ringraziare anche gli amici che ci sono stati da sempre (Andre Prev, Blanco, Fiumi, Luca, Ricardo...) e quelli che ultimamente ho perso un po' di vista per ragioni logistiche ma che comunque sono sempre presenti nei miei pensieri (Beatrice, Morze, Martina, Linda, Andrea S. e R., Camilla, Laura, Alice). In questi anni sono sempre riusciti a farmi svagare facendomi dimenticare gli esami e lo studio anche solo per una sera o due a settimana.

Nonostante si possa pensare che il Polimi sia solo fonte di studio e sofferenza è riuscito in realtà anche a darmi l'occasione di conoscere persone con cui ho legato moltissimo. Colleghi che hanno avuto la sventura di dover seguire i corsi o consegnare progetti con me come: Rocco, Team SAGITTA (Ibra, Andrea Bavetta, Big1), Jack, Aelsio Alò, Ilaria, Matheiu Peeeeetittttt, Mary Paul, Cao, Fra Lisi, Ubi e tutto il Team ECLIPSIS.

A TAS-I non solo ho avuto modo di avere i primi assaggi di vita lavorativa ma anche di conoscere straordinari colleghi con cui scambiare battute in pausa pranzo e alle pause caffè, come i tesisti/stagisti di "The Cactus" o agli internisti dei vari uffici (il mio, Recycle lab e l'ufficio di Mariano).

Contents

List of Figures

List of Tables

List of Abbreviations

DoF	**D**egree **o**f **F**reedom
JPADS	**J**oint **P**recision **A**irdrop **S**ystem
AoA	**A**ngle **o**f **A**ttack
FpA	**F**light **p**ath **A**ttack
LZ	**L**anding **Z**one
EM	**E**nergy **M**anagement
L1	**L**oiter **1**
L2	**L**oiter **2**
GS	**G**lide **S**lope
CEP	**C**ircular **E**rror **P**robability

List of Symbols

AR	aspect ratio	$-$
b	parafoil wingspan	m
c	parafoil chord	m
$\mathbf{c}$	damping coefficient	m
C_i	aerodynamic i-coefficient	$-$
d	diameter	m
D	drag	N
e	Euler's number	$-$
$\underline{F}$	force vector	N
h	altitude	m
I_{ij}	moment of inertia w.r.t. ij-axes	km^2
k	stiffness	$\mathrm{N\,m^{-1}}$
l	line length	m
L	lift	N
$\underline{L}_{ij}$	rotation matrix from i to j	$-$
m	mass	k
$\underline{M}$	moment vector	N m
$\underline{\underline{M}}$ mass matrix	k	
p	roll angular velocity	$\mathrm{rad\,s^{-1}}$
P	power	W ($\mathrm{J\,s^{-1}}$)
q	pitch angular velocity	$\mathrm{rad\,s^{-1}}$
$\underline{q}$	quaternion vector	$-$
r	yaw angular velocity	$\mathrm{rad\,s^{-1}}$
R	parafoil radius	m
$\mathbf{R}$	turning radius	m
S	surface	m^2
$\underline{t}$	parafoil thickness	m
t	time	s
u	control action	rad or $^\circ$
V	velocity modulus	$\mathrm{m/s}^2$
$\underline{v}$	velocity vector	$\mathrm{m/s}^2$
x, y, z	spatial coordinates	m
$\overline{x}$	mean value of the x-variable	depending on the quantities considered
$\underline{x}$	spatial vector	m
α	angle of attack	rad or $^\circ$
β	sideslip angle	rad or $^\circ$
γ	flight path angle	rad or $^\circ$
δ	aileron angular deflection	rad or $^\circ$
ϵ_0	semi-aperture angle of the canopy	rad
ζ	normalized chord wise coordinate	$-$
η	angular lateral error	rad
θ	pitch angle	rad or $^\circ$

μ	rigging angle	rad or $^\circ$
ρ	density	$\mathrm{kg\,m^{-3}}$
$\overline{\rho}$	CEP correlation factor	$-$
σ	standard deviation	depending on the quantities considered
τ_0	adimensional inflation time	$-$
ϕ	roll angle	rad or $^\circ$
ψ	yaw angle	rad or $^\circ$
$\underline{\omega}$	angular velocity vector	$\mathrm{rad\,s^{-1}}$

Chapter 1

Introduction

The success of IXV mission proved at European level the possibility to safely re-enter the atmosphere. The next step ESA required was the possibility to exploit the knowledges gained from IXV to built a reusable space vehicle, SpaceRider. SpaceRider is a low cost re-usable multipurpose European space platform to be launched on the top of a Vega C in 2020. Payloads will be ferried to space by SpaceRider, then payloads will work in a space environment for a period up to some months and finally they will survive to the atmospheric re-entry thanks to SpaceRider. Thus it will allow to safely retrieve the payloads which will be analyzed on Earth. During the first phases of the program, configuration studies concluded that, in order to reuse the spacecraft, it would be advisable to exploit a parafoil in the last stage of the aerodynamic decelerator system instead of a splash-down with ballistic parachutes [1]. The parafoil also allows to save mass with respect to a classical winged configuration [2]. Although NASA with the X-38 program got insights of how parafoil works for a space application [19] [5] [4] [15], European knowledge in this field remains confined to military cargo delivery or university studies.

The parafoil main benefit is the possibility to steer the system, allowing to reduce the dispersion of the landing point, thanks to a control logic [22] [29] [11] [23] [28] [16]. Also, the higher lift-to-drag ratio, with respect to ballistic parachutes, allows parafoil to have the same vertical velocity with a lower canopy area, thus lightening the system. The total velocity will be higher (due to the horizontal component) so the system will need to land in the same fashion of an aircraft or to be retrieved in air (MAR) [2]. This total velocity can be even be reduced more if a flare strategy is employed at landing [29], Appendix B. The controllability combined with a higher flight velocity allows the parafoil also to be much more robust to the wind disturbances than a ballistic parachute. With respect to a traditional winged configuration, the parafoil allows not only to save mass but also to reduce complexity due to the lower terminal velocity at landing [2].

The aim of the present work is to develop a multi-body model that can accurately represent the behavior of the parafoil-payload system in its all flight phases: from inflation to landing. The model is designed to be used in the frame of the SpaceRider mission [2], to size the aerodynamic decelerator system, the connection lines and the GNC algorithms. Therefore the most important quantities that must be computed correctly are the loads experienced at the inflation and the trajectory of the system [4].

There are several models developed for a parafoil-payload system. The most simple one considers a three degrees of freedom (DoFs) representation: the parafoil is therefore considered only as an added inertia and with its aerodynamic properties. These kinds of model are very useful to design and test GNC algorithms due to their computational speed. More complex models add more DoFs: parafoil and payload are treated as two separate elements. For example 9 DoFs model considers

FIGURE 1.1: SpaceRider mission concept

decoupled angular dynamic of parafoil and payload but the same linear dynamic. [13] [29]

In the present work a 12 DoFs model is developed and analyzed, its structure is presented in Figure 1.2. A so high number of DoFs have never been implemented so far. Usually models are limited to a 9 DoFs system representation [22] [29] [11] [23] [28] [16] [26] [21] [20] [6] [18], because it is enough to represent in an accurate way the dynamic behavior of the parafoil-payload system [22] (roll and skid-steering modes). The addition of the 3 DoFs is of course an additional computational burden, due to decouple the linear dynamic of the parafoil and the payload. Anyway it is needed because of the particular SpaceRider connection lines system with four bridles, Section 2.3. The modular design of the model allows also to use it to design separately the parafoil and the GNC or even to test parafoil applications in different environments from the Earth one, Figure 1.2.

Particular emphasis is posed on representing accurately the inflation loads. The usual approach is to use empirical models coupled with a very simple (3 DoFs) dynamic [13] [29], the exploitation of additional DoFs of the presented model should allow a more realistic trend of the loads.

PID controller are used in the longitudinal control even if the parafoil-payload system is a very non-linear system [29] [25]. In the present work new approach of non-linear Lyapunov stable rigging control will be developed, demonstrated and characterized to see whether it performs better than a linear PID controller.

The present work is divided in 6 Chapters. In Chapter 1 an overview of the state of the art and the aim of this work are presented. In Chapter 2 is reported the mathematical model to deal with the parafoil physic; the assumptions and the validity limits of the model are presented too. The model is then validated in Chapter 3, in order to ensure its physical meaning both at steady-state and at the inflation. Once the model has been validated a control strategy can be applied to it, the control logic and its analytic demonstration are shown in Chapter 4. Chapter 5 shows how the model can be used to size both the GNC system and to design the aerodynamic decelerator system. In Chapter 6 achievements are critically analyzed with respect to

the proposed objectives and possible starting points for further studies to be presented.

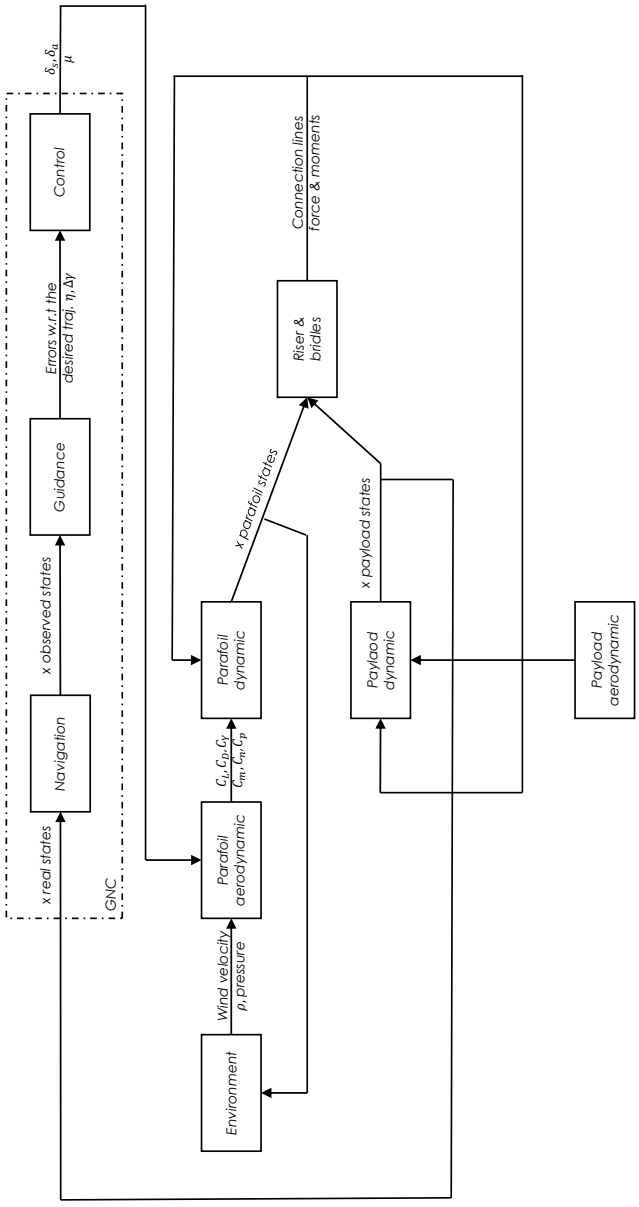

FIGURE 1.2: Physical structure of the model

Chapter 2

Modeling

The model represents a parafoil-payload system. There are two rigid bodies: parafoil and payload, each of them has 6 DoFs. The three rigid body rotations and translations are allowed in 3D space. The overall degrees of freedom are 12. In Figure 2.1 is visualized the system.

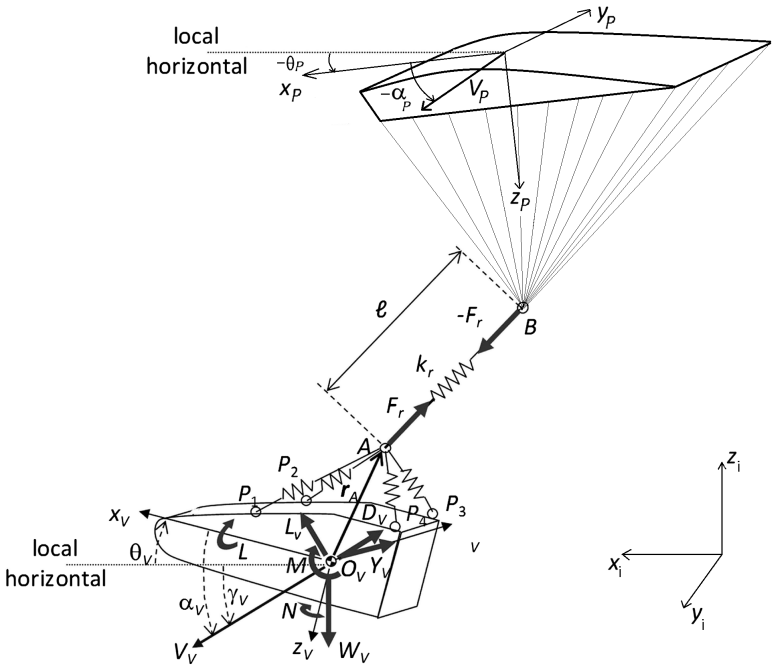

FIGURE 2.1: Parafoil-payload system

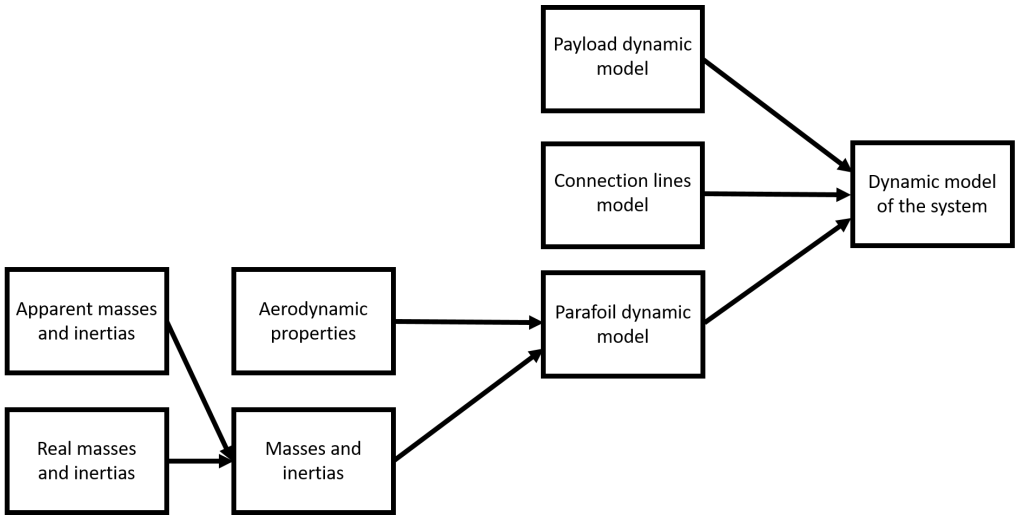

FIGURE 2.2: Chapter 2 flow chart

The system is presented in this Chapter as shown in Figure 2.2: it is decomposed in its three main constituting components (parafoil, payload and suspension lines). A more detailed analysis of the parafoil element is presented, being divided in the main components that make up the dynamic model.

2.1 Parafoil model

As stated previously the parafoil has been modeled as a rigid body with 6 DoFs. The representation has some limitations that must be acknowledged. Most importantly the fluid-structural interaction characterizing lightweight parafoil structures is not completely modeled. No total or partial collapse of the parafoil or cells is therefore considered, even if X-38 drop tests show these phenomena occur quite often [4]. This limitation could demand some limits in the flight envelope, especially during control or maneuver (i.e.an incidence angle can not be lowered more than -12 degrees because it could lead the canopy leading edges to collapse [13]).

The aim of this thesis is not to design the parafoil canopy in details: fabric of the canopy, position and dimensions of the inlets and so on. The rigid body assumption is therefore acceptable. [25]

The sole interaction between structure and aerodynamic loads is considered during the inflation, as it will be shown in Section 2.1.3.

The parafoil is a light wing load structure ($lessthan50\frac{N}{m^2}$), so the effect of the added masses must be taken into account and modeled accurately. In these particular applications inertia effects due to added masses can be in the same order of magnitude or even higher than the ones generated by system real masses. Considerations about added masses also affect the position of the body reference frame of the parafoil itself, Section 2.1.1.

2.1.1 Added mass and inertia model

The added mass effects are related to the change of body motion generating changes in the surrounding fluid flow, so that the acceleration of the body requires additional forces because of fluid opposing this acceleration. [14] As reported by G. Kowaleczko apparent masses and inertias *"are not the real mass and moment of inertia of the fluid moving with the body but represents an additional energy transported to*

the fluid during body acceleration". [10] How to compute the trapped air masses and inertias is shown in Section 2.1.2.

Before showing the way to compute added inertias and masses, the orientation and position of the reference system must be taken into consideration. T.M. Barrows demonstrates that in parafoils *"may not be possible to find a single point at which the rotational and translational motions are decoupled"* [3], it means that the smartest approach is to impose the system reference in center of solid mass, and consequently to take into account the displacement of added masses centers using the moment transport.

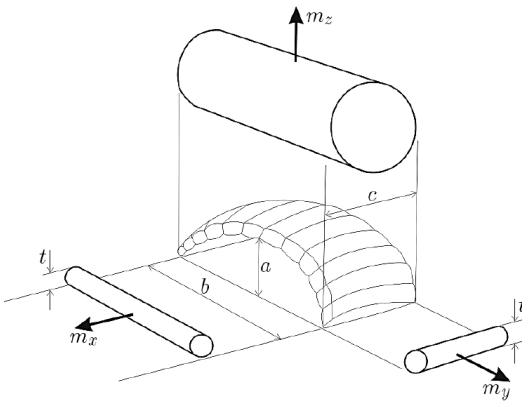

FIGURE 2.3: Added masses

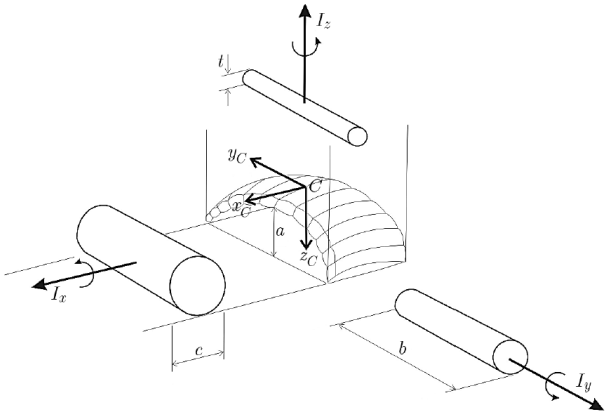

FIGURE 2.4: Added inertia moments

The apparent mass centers are defined as points where is experienced less resistance to rotational acceleration around the axis considered [10]. So the point C_1 is the apparent mass center of m_x while the point C_2 is the apparent mass center of m_y and m_z.

To find the position of these points some guidelines are given by G. Kowaleczko. The y coordinates are equal to zero for symmetry along the XZ-plane. Coordinates x are equal to zero being the reference system z-axis passing along the joining between C_2 and C_1. [3] While the coordinates z_{C_1} and z_{C_2} can be computed using Equations from 2.1 to 2.5.

$$z_{C_1} = R - a_1 \qquad z_{C_2} = R - a_2 \tag{2.1}$$

$$a_1 = \frac{Rsin\epsilon_0}{\epsilon_0} \qquad a_2 = \frac{a_1 m_{y-flat}}{m_{y-flat} + \frac{I_{app_{x-flat}}}{R^2}} \tag{2.2}$$

$$\epsilon_0 = sin^{-1}\left(\frac{b}{2R}\right) \tag{2.3}$$

$$I_{app_{x-flat}} = \rho 0.84 \frac{AR}{1+AR}\frac{\pi}{48} c^2 b^3 \tag{2.4}$$

$$m_{y-flat} = \rho k_B \frac{\pi}{4} t^2 c \tag{2.5}$$

G. Kowaleczko reports how the value of k_B changes depending on the tip shape of the parafoil: 0.33 is a good value for an ellipsoid parafoil with $AR = 3$, $k_B = 1.0$ for a rectangular parafoil with ellipsoidal end caps, $k_B = 1.24$ for a rectangular

parafoil with flat end caps. [10] This value will be fixed once the SpaceRider parafoil is designed.

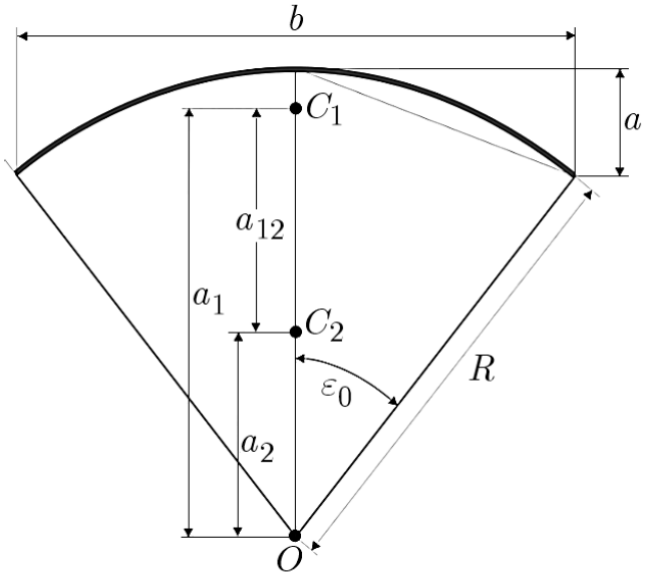

FIGURE 2.5: C_2 and C_1 positions

Being impossible to decouple the rotational and translational motions, the apparent inertia matrix is not-diagonal and it can be written as shown in Equation 2.6. This matrix will be then added to the real inertia matrix of the parafoil.

$$\underline{\underline{J}} = \begin{bmatrix} \underline{\underline{M}} & \underline{\underline{J}}_{off-diagonal} \\ \underline{\underline{J}}^T_{off-diagonal} & \underline{\underline{I}} \end{bmatrix} \tag{2.6}$$

Where the matrices that constitute the inertia matrix are expressed by the Equations from 2.7 to 2.9.

$$\underline{\underline{M}} = \begin{bmatrix} m_x & 0 & 0 \\ 0 & m_y & 0 \\ 0 & 0 & m_z \end{bmatrix} \tag{2.7}$$

$$\underline{\underline{J}}_{off-diagonal} = \begin{bmatrix} 0 & m_x z_{C_1} & 0 \\ -m_y z_{C_2} & 0 & m_y x_{C_2} \\ 0 & -m_z x_{C_2} & 0 \end{bmatrix} \tag{2.8}$$

$$\underline{\underline{I}} = \begin{bmatrix} I_{app_{xx}} + m_y z_{C_2}^2 & 0 & -m_y z_{C_2} x_{C_2} \\ 0 & I_{app_{yy}} + m_x z_{C_2}^2 + m_z x_{C_2}^2 & 0 \\ -m_y z_{C_2} x_{C_2} & 0 & I_{app_{zz}} + m_y x_{C_2}^2 \end{bmatrix} \tag{2.9}$$

The terms in Equations from 2.7 to 2.9 can be computed as stated by T.M. Brown [14] using Equations from 2.15 to 2.20. Terms depend on apparent masses and inertias values computed under the flat parafoil assumption, Equations 2.10 to 2.13. Computed values are then corrected taking into account the thickness of the parafoil.

$$m_{x-flat} = 0.848 \rho \frac{\pi}{4} \underline{t}^2 b \tag{2.10}$$

$$m_{z-flat} = \frac{AR}{1+AR} \rho \frac{\pi}{4} c^2 b \tag{2.11}$$

$$I_{app_{yy-flat}} = 1.161 \frac{AR}{1+AR} \rho \frac{4\pi}{48} c^4 b \tag{2.12}$$

$$I_{app_{zz-flat}} = 0.848 \rho \frac{\pi}{48} \underline{t}^2 b^3 \tag{2.13}$$

$$\bar{a} = \frac{R(1-cos(\epsilon_0))}{b} \tag{2.14}$$

$$m_x = m_{x-flat} \left(1 + \frac{8}{3}\bar{a}^2\right) \tag{2.15}$$

$$m_y = \frac{1}{a_1^2}(R^2 m_{y-flat} + I_{app_{xx-flat}}) \tag{2.16}$$

$$m_z = m_{z-flat} \sqrt{1 + 2\bar{a}^2 \left(1 - \left(\frac{t}{c}\right)^2\right)} \tag{2.17}$$

$$I_{app_{xx}} = \frac{(a_1 - a_2)^2}{a_1^2} R^2 m_{y-flat} + \frac{a_2^2}{a_1^2} I_{app_{xx-flat}} \tag{2.18}$$

$$I_{app_{yy}} = I_{app_{yy-flat}} \left(1 + \frac{\pi}{6}(1+AR)AR \quad \bar{a}^2 \left(\frac{\underline{t}}{c}\right)^2\right) \tag{2.19}$$

$$I_{app_{zz}} = (1 + 8\bar{a}^2) I_{app_{zz-flat}} \tag{2.20}$$

Equation 2.21 shows the values of apparent masses and inertias computed with this procedure at 0 height, using as reference the geometrical values of the parafoil used in simulations, Table 2.1.

$$\underline{\underline{J}}_{app} = \begin{bmatrix} 71 & 0 & 0 & 0 & 181 & 0 \\ 0 & 486 & 0 & -7426 & 0 & 0 \\ 0 & 0 & 1749 & 0 & 0 & 0 \\ 0 & -7426 & 0 & 120654 & 0 & 0 \\ 181 & 0 & 0 & 0 & 22081 & 0 \\ 0 & 0 & 0 & 0 & 0 & 5914 \end{bmatrix} \tag{2.21}$$

TABLE 2.1: Geometric values of the parafoil used

Parameter	Value
S [m^2]	100
b [m]	17.32
c [m]	5.77
AR [-]	3
$\underline{t}$/c [-]	0.18
R [m]	0.6 b

The present computation must be nested inside the model: in this way added masses can be computed in real time during the inflation, Section 2.1.3. This shrewdness is needed above all when analyzing the inflation loads. Results can be quite different: depending on added masses and inertias considered constant or computed in real time, as shown in Figure 2.6.

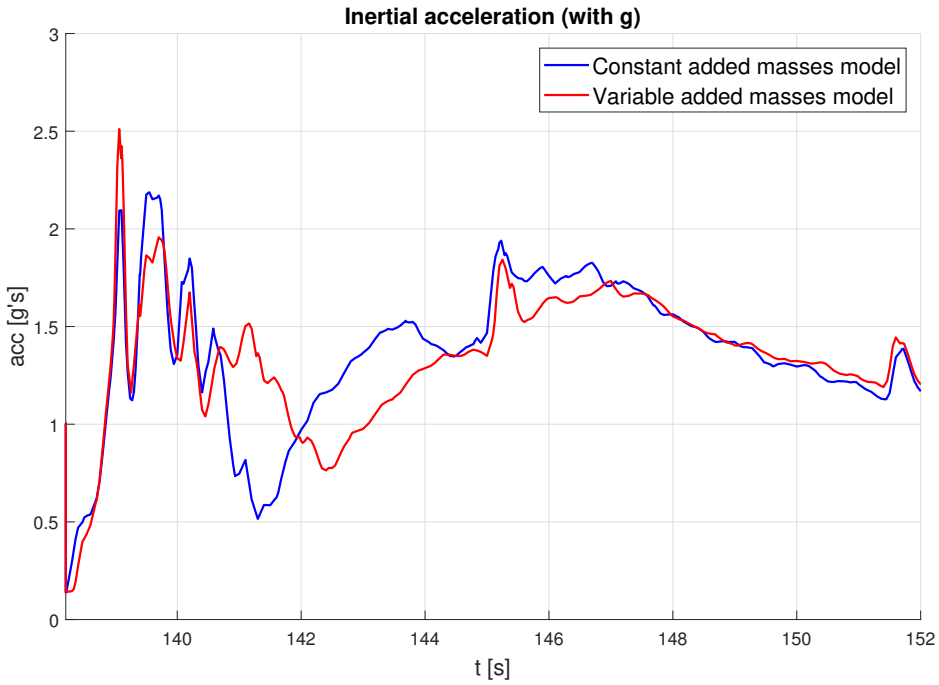

FIGURE 2.6: Inflation loads assuming constant or variable added masses

2.1.2 Real and trapped masses and inertias

To be flexible the model can compute by itself the real mass of the parafoil canopy and the trapped air mass. The model used is the one presented by O. Yakimenko in [29]. The limits of the model are also presented: the parafoil used in simulations fits all the applicability limits.

$$m = \rho \underline{t} c \epsilon_0 (2R + (1 - 2\zeta)\xi) \tag{2.22}$$

Equation 2.22 is useful to compute both the air mass trapped inside the canopy and the canopy mass itself, depending on the ρ used. The dependence on the air density make mandatory to implement these computations inside the model due to the changes of ρ that the system will experience during descent.

The parameter ζ in Equation 2.22 is the x-coordinate normalized of the intersection between the mean chord and its normal passing through confluence point of the suspension lines. Being a normalized coordinate its value can range from 0 to 1, usually is equal to 0.25 or 0.5. The parameter ξ is defined as $\xi = c(1 + \mu^2)^{-0.5}$

$$
\begin{aligned}
I_{xx} &= \rho \underline{t} c \left(\epsilon_0 - \frac{1}{2} sin(2\epsilon_0)\right) \left(R^3 + \frac{3}{2} R^2 \mu (1-2\zeta)\xi + R\mu^2(1-3\zeta+3\zeta^2)\xi^2 \right. \\
&\left. + \frac{1}{4}\mu^3(1-4\zeta+4\zeta^2-4\zeta^3)\xi^3\right) + 2\epsilon_0 \left(\frac{1}{3} R(1-3\zeta+3\zeta^2)\xi^2 + \frac{1}{4}\mu(1-4\zeta+4\zeta^2-4\zeta^3)\xi^3\right) \\
I_{yy} &= \rho \underline{t} c \left(\epsilon_0 + \frac{1}{2} sin(2\epsilon_0)\right) \left(R^3 + \frac{3}{2} R^2 \mu (1-2\zeta)\xi + R\mu^2(1-3\zeta+3\zeta^2)\xi^2 \right. \\
&\left. + \frac{1}{4}\mu^3(1-4\zeta+4\zeta^2-4\zeta^3)\xi^3\right) + 2\epsilon_0 \left(\frac{1}{3} R(1-3\zeta+3\zeta^2)\xi^2 + \frac{1}{4}\mu(1-4\zeta+4\zeta^2-4\zeta^3)\xi^3\right) \\
I_{zz} &= \rho \underline{t} c \epsilon_0 \left(2R^3 + 3R^2\mu(1-2\zeta)\xi + 2R\mu^2(1-3\zeta+3\zeta^2)\xi^2 + \frac{1}{2}\mu^3(1-4\zeta+4\zeta^2-4\zeta^3)\xi^3\right) \\
I_{xz} &= \rho \underline{t} c \xi 2 sin(\epsilon_0) \left(\frac{1}{2} R^2(1-2\zeta)\xi + \frac{2}{3} R\mu(1-3\zeta+3\zeta^2)\xi + \frac{1}{4}\mu^2(1-4\zeta+4\zeta^2-4\zeta^3)\xi^2\right)
\end{aligned}
\tag{2.23}
$$

Equations from 2.22 to 2.23 allow to compute the mass and inertia properties of the parafoil knowing its geometry.

It is notable how the μ is going to affect these computations, in case of rigging control the masses and inertias will change in time, thus computations must be nested inside the model that will be time-integrated.

Equation 2.24 shows the values found with this model at sea-level for the parafoil data reported in Table 2.1.

$$
\begin{aligned}
\underline{\underline{J}}_{real} &= \begin{bmatrix} 161 & 0 & 0 & 0 & 0 & 0 \\ 0 & 161 & 0 & 0 & 0 & 0 \\ 0 & 0 & 161 & 0 & 0 & 0 \\ 0 & 0 & 0 & 11281 & 0 & 3579 \\ 0 & 0 & 0 & 0 & 4156 & 0 \\ 0 & 0 & 0 & 3579 & 0 & 15238 \end{bmatrix} \\
\underline{\underline{J}}_{trapped} &= \begin{bmatrix} 171 & 0 & 0 & 0 & 0 & \\ 0 & 171 & 0 & 0 & 0 & 0 \\ 0 & 0 & 171 & 0 & 0 & 0 \\ 0 & 0 & 0 & 12011 & 0 & 3812 \\ 0 & 0 & 0 & 0 & 4420 & 0 \\ 0 & 0 & 0 & 3812 & 0 & 16232 \end{bmatrix}
\end{aligned}
\tag{2.24}
$$

2.1.3 Inflation model

As reported by J.S. Lingard, experimental analyses of the parafoil inflation show how during the first moments of the inflation the parafoil behaves like a ballistic parachute. There is no cell inflation until the surface reaches the value 0.8 of the nominal fully-inflated surface. Therefore the parafoil doesn't generate lift and it doesn't behave like a wing until this condition occurs. [13] In case of inflation control techniques (reefing), it is assumed that the ballistic approximation is true only until the surface reaches 0.8 of the first reefed stage.

From a dynamical point of view, as far as parafoil is similar to a ballistic parachute, it means that the DOFs of the system must be temporary reduced. Ballistic parachutes indeed have not a lateral-directional dynamic comparable to the parafoil one. In the present thesis the choice is to reduce the DoFs of the parafoil from 6 to 5 until the surface reaches the cell inflation value. Imposing the dynamic around the pitch axis

equal to zero, it will not affect results in a negative way. Being the inflation time very reduced with respect to the overall simulation time, the trajectory will not be affected by significant errors. The loads experienced by the system will be eventually higher than a 6 DoF simulation because the motion around one axis is limited. The result is thus conservative and acceptable.

It is also possible to use the same inflation model with different parameters. The model foresees the numerical integration of the dynamic equations while having the surface evolution in time expressed by an exponential law 2.25.

$$S(t) = \%_{reef} S_{ref} \frac{e^{\frac{(t-t_{in})n}{\Delta t}} - 1}{(e^n - 1)} \tag{2.25}$$

Where Δt is found with Knacke equation, 2.26. D_0 is the nominal diameter of the parafoil computed as if it has a circular shape, Equation 2.27. V_S is the snatch velocity: the velocity of the parachute at the beginning of the inflation and it is obtained by the dynamic simulation. τ_0 is the dimensionless inflation time, a parameter that changes depending on the type of parachute considered, on the shape of the section and on the presence or absence of reefing. For ballistic parachutes τ_0 is generally 10, while for parafoils is equal to 14 if there is slider reefing (suitable only for small personal parafoils) otherwise can be assumed equal to 3.5 if there is no reefing.

$$\Delta t = \frac{\tau_0 d_0}{V_S} \tag{2.26}$$

$$d_0 = \left(\frac{4 S_{parafoil}}{\pi} \right)^{0.5} \tag{2.27}$$

The $C_{D_{Nom}}$ of ballistic parachutes and parafoil at high angles of attack is close to 1, as shown in graphs in Section 2.1.4.

When the parafoil surface is about the nominal value, there is a pitch down maneuver. During this movement cells begin to inflate. Thus the value of the angle of attack begins to rise, the lift begins to be generated and the peak load is reached, Figure 2.7. This is correct as reported by J.S. Lingard [13].

In the model was implemented the possibility to have multiple reefed stages in order to reproduce the X-38 drop tests, Chapter 3, and to be more flexible too.

Reefing is a peculiar technique to limit inflation loads avoiding to deploy all the canopy at the same time. In this way the aerodynamic loads will be reduced with respect to the free-inflation case.

The reefing strategy analyzed in the present work is a span-reefing one, due to its flight heritage. It was exploited by Pioneer in the X-38 test campaign. It helps to compute the added mass evolution with respect to time: only the span will change and it can be related to the surface evolution in time with Equation 2.28. The time variant b will then be used in Section 2.1.1.

$$b(t) = \frac{S(t)}{c} \tag{2.28}$$

Simulations showed that the reefing strategy of a parafoil is not straight forward as for the ballistic parachutes. In the latter, as a rule of thumb, if the parachute is reefed at 33% of the nominal area decelerations experienced will be 1/3 of the free-inflation case. In parafoils this rule isn't true because the behavior of the aerodynamic coefficients at high angle of attack are the main parameters affecting aerodynamic loads.

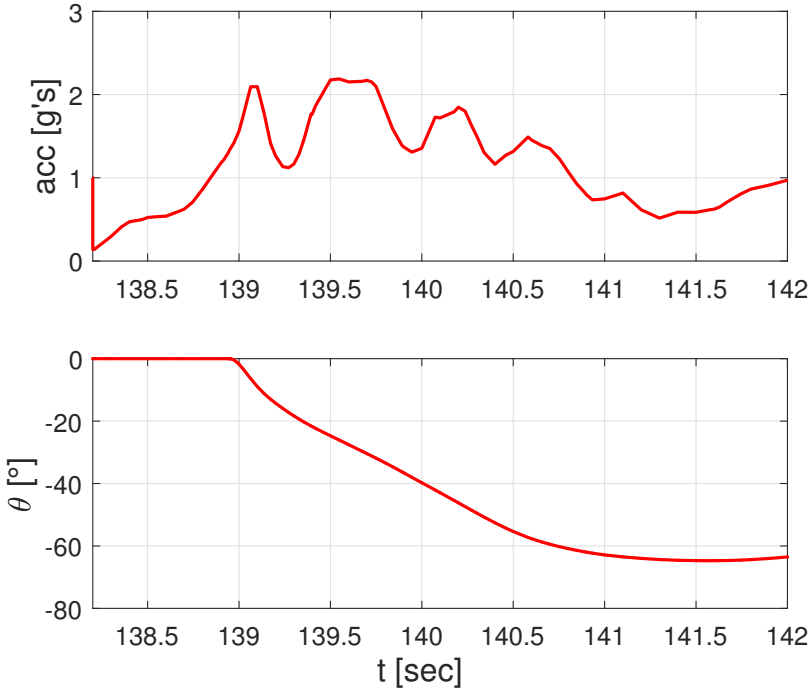

FIGURE 2.7: Parafoil pitch down

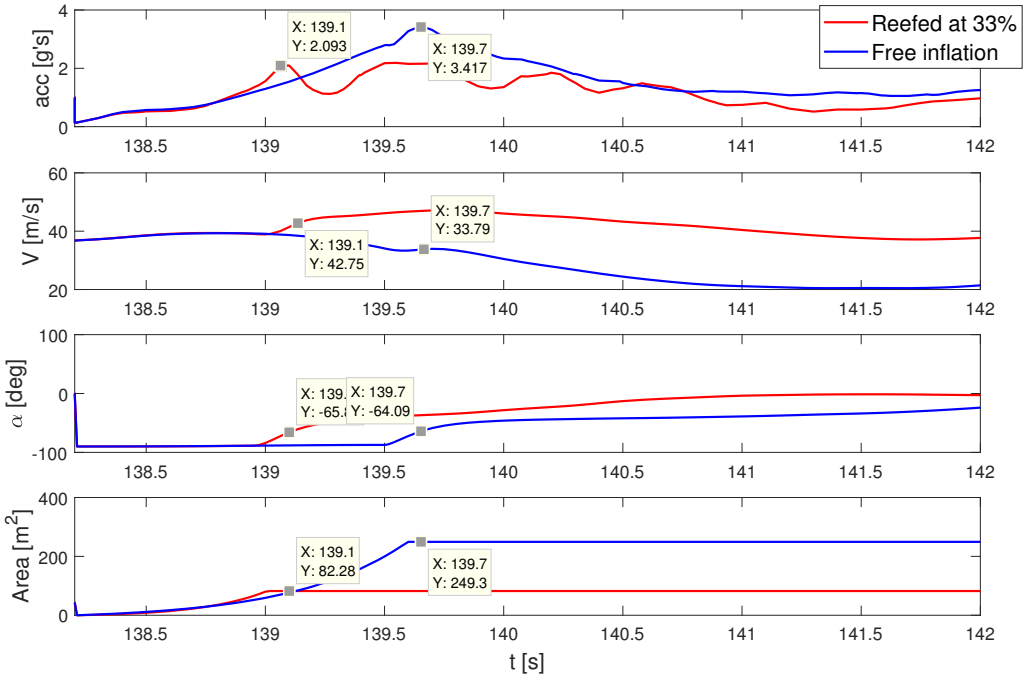

FIGURE 2.8: Parameters comparison free-inflation vs 33% reefed case

As shown in Figure 2.8 the peak load in the reefed case is not 1/3 as it would be in a ballistic case (reefing percentage is equal to 33%). Instead it is only reduced of a factor 1.88. This is due to the aerodynamic loads generated by the parafoil once its cells inflate: the α at the peak load is the same value for both cases (C_L and C_D

having the same aerodynamics). Although due to the limited size of the canopy, before the peak load the reefed case increases its velocity, so it experiences a higher value of deceleration than expected, Figure 2.9.

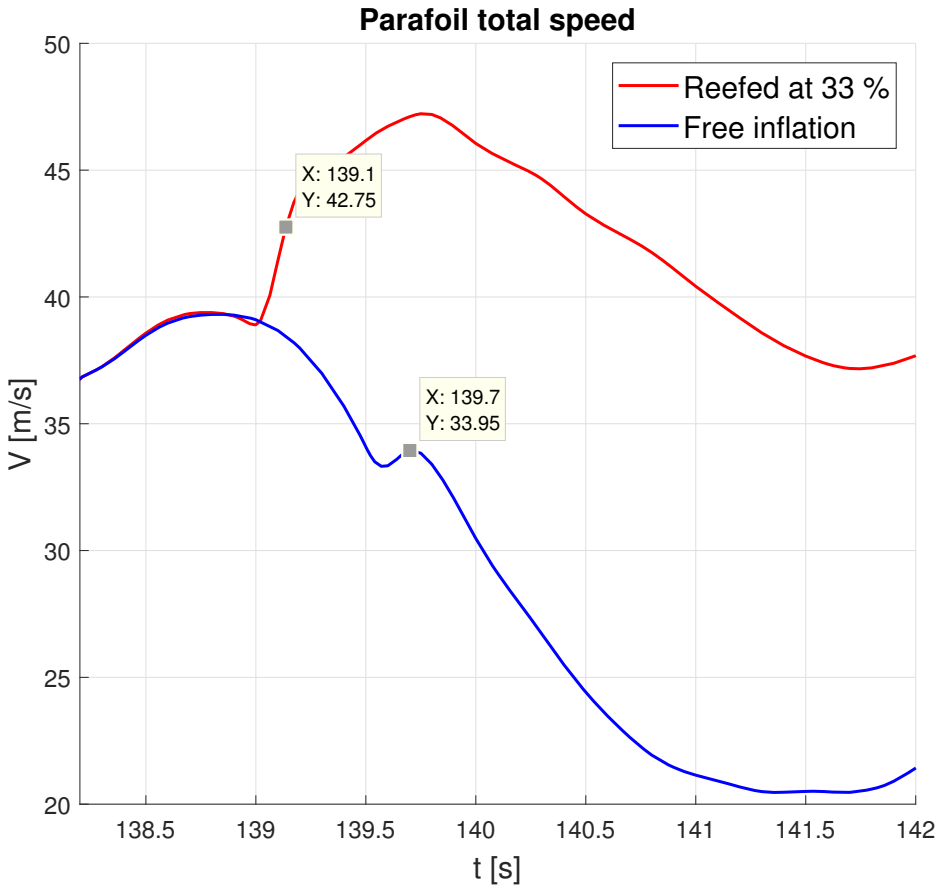

FIGURE 2.9: Velocity increases in the case of reefed case

2.1.4 Aerodynamic forces

In comparison with airplane wings, parafoil aerodynamic characteristics must be modeled accurately in the non-linear regime because they usually work at higher angle of attack. This is particularly true for the C_L, C_D and C_m, because they are responsible for the angle of attack at which the system will trim itself. Examples of behaviors of aerodynamic coefficients at angle of attacks ranging from 0 to 90 degrees are reported in Figures from 2.10 to 2.13. Referring to these graphs it is possible to extrapolate the aerodynamic coefficient values knowing α. [15] [4] [5]

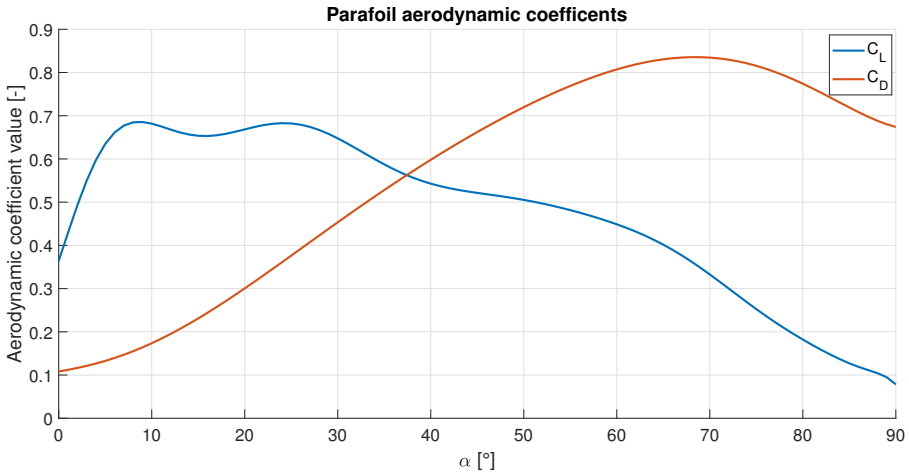

FIGURE 2.10: Lingard reported aerodynamic coefficient values [13]

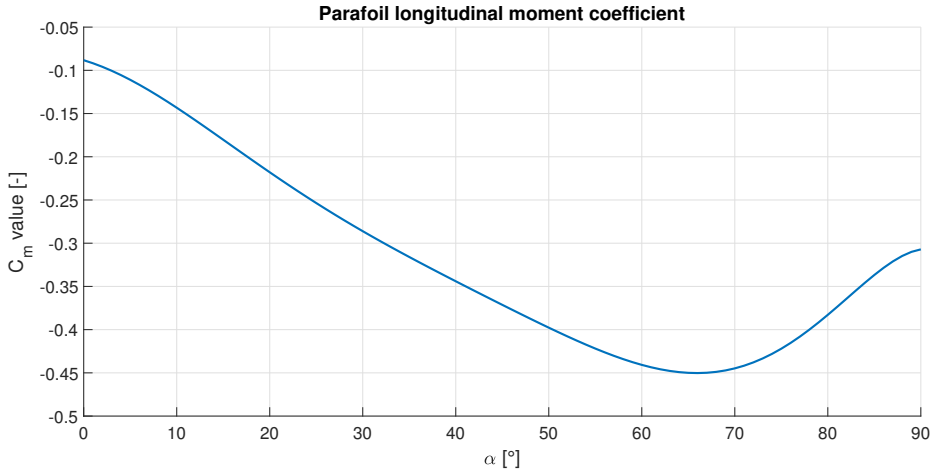

FIGURE 2.11: Lingard reported C_m value at $\frac{c}{4}$ [13]

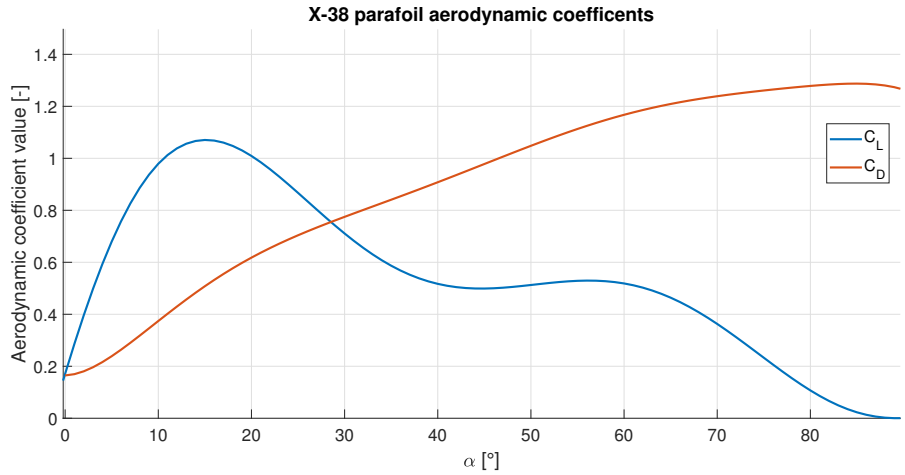

FIGURE 2.12: X-38 parafoil reported aerodynamic coefficient values [19]

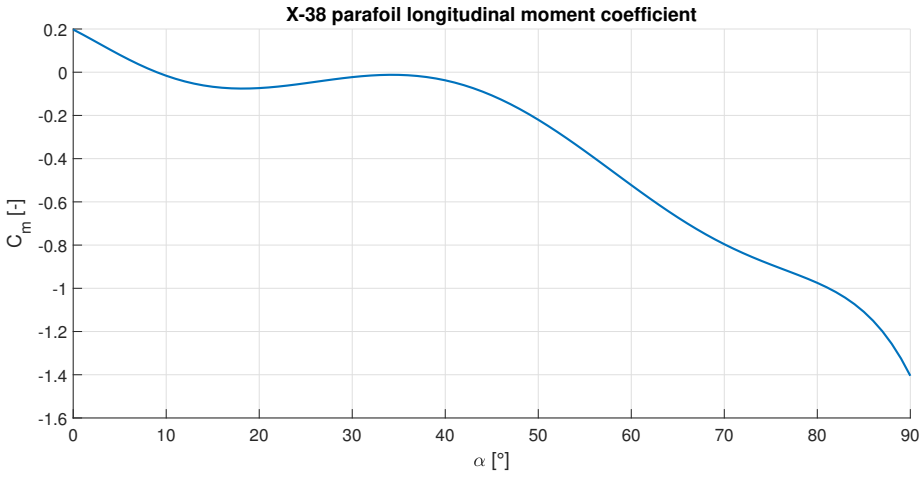

FIGURE 2.13: X-38 parafoil C_m values evaluated at the confluence point [19]

As stated in the inflation model Section 2.1.3, parafoil begins to behave as a wing when it is almost fully inflated. It implies that other aerodynamic characteristics C_Y, C_n, C_l can be considered in their linearized form.

$$\begin{aligned} C_L &= C_{L_0} + C_{L_\alpha}\alpha \\ C_D &= C_{D_0} + C_{D_\alpha}\alpha^2 + C_{D_{lines}} \\ C_Y &= C_{Y/\beta}\beta \\ C_m &= C_{m_q} q \frac{c}{2V} + C_{m_0} + C_{m_\alpha}\alpha \\ C_n &= C_{n_r} r \frac{b}{2V} \\ C_l &= C_{l_p} p \frac{b}{2V} \end{aligned} \tag{2.29}$$

The term $C_{D_{lines}}$ in Equation 2.29 is the drag generated by connection lines. While it is supposed the lift generated is negligible, the drag could be considerable. In

order to be flexible the model compute the $C_{D_{lines}}$ with an empiric law depending on the parameters which characterize the connection lines, Equation 2.30.

$$C_{D_{lines}} = \frac{num \quad R \quad d \quad cos(\alpha)^3}{S} \tag{2.30}$$

In Equation 2.30 d is the diameter of the suspension lines (must be given as an input) while num is the number of connection lines. As rule of thumb, it can be assumed there is one line each $1.11m^2$ of canopy surface [13].

Once the aerodynamic coefficients are computed, it is possible to find the value of the aerodynamic forces and moments with Equation 2.31. They are aligned with the wind axis so they must be rotated in the body axis with the rotation matrix 2.32. The term μ is the rigging angle that can be set and maintained constant or changed during flight, as shown in Section 4.3.2.

$$\begin{aligned} \underline{F}_{aer} &= \frac{1}{2}\rho V^2 S \begin{bmatrix} -C_D \\ C_Y \\ -C_L \end{bmatrix} \\ \underline{M}_{aer} &= \frac{1}{2}\rho V^2 S \begin{bmatrix} C_l & b \\ C_m & c \\ C_n & b \end{bmatrix} \end{aligned} \tag{2.31}$$

$$\underline{\underline{T}}_{w/b} = \begin{bmatrix} cos(\alpha+\mu)cos(\beta) & cos(\alpha+\mu)sin(\beta) & -sin(\alpha+\mu) \\ -sin(\beta) & cos(\beta) & 0 \\ sin(\alpha+\mu)cos(\beta) & sin(\alpha+\mu)sin(\beta) & cos(\alpha+\mu) \end{bmatrix} \tag{2.32}$$

In the present work two different aerodynamic data of the SpaceRider parafoil have been considered. First the X-38 non-linear aerodynamic data reported in [19] and shown in Figure 2.12 and 2.13. Secondly, to test the robustness of the model, the aerodynamic data reported in Table 2.2 and 2.3 were used. Lateral aerodynamic data are taken from O. Yakimenko book [29].

TABLE 2.2: Aerodynamic data considered for the linear parafoil

Aerodynamic coefficient	Value
C_{L_0} [-]	0.24
C_{L_α} [1/rad]	2.14
C_{D_0} [-]	0.12
C_{D_α} [1/rad]	0.33
C_{m_0} [-]	-0.175
C_{m_α} [1/rad]	0

TABLE 2.3: Damping and lateral aerodynamic coefficient considered for both parafoils

Aerodynamic coefficient	Value
C_{Y_β} [1/rad]	-1
C_{m_q} [1/rad]	-2.5
C_{n_r} [1/rad]	-0.27
C_{n_p} [1/rad]	-0.082
C_{n_β} [1/rad]	-0.0015
C_{l_p} [1/rad]	-0.84
C_{l_r} [1/rad]	-0.082
C_{l_β} [1/rad]	-0.036

The X-38 data are very useful not only because they are represented in non-linear range of α (from 0 to 90) but also because they refer to a parafoil of aspect ratio 3 with a Clark-Y airfoil section. This kind of parafoil is the most used type so, probably, they will be the most representative data of the real behavior of the SpaceRider parafoil.

2.1.5 Dynamics model

The representation of the system is performed in time domain with a non-linear state-space model obtained by considering the conservation of the angular and linear momentum, in this way Equation 2.33 may be written.

After modeling all the forces and moments as described in Sections 2.1.1 and 2.1.4, it is possible to solve the dynamic system thus obtaining the evolution in time of the states, namely the linear and angular velocities. Having a coupled system, Section 2.1.1, the vectorial system described in Equation 2.33 must be solved at each iteration step at the same time.

$$\begin{bmatrix} \underline{\dot{v}} \\ \underline{\dot{\omega}} \end{bmatrix} = \underline{\underline{I}}^{-1} \left(\begin{bmatrix} \underline{F} \\ \underline{M} \end{bmatrix} - \begin{bmatrix} \underline{\omega} \wedge \underline{\underline{M}}\underline{v} \\ \underline{\omega} \wedge \underline{\underline{I}}\underline{\omega} \end{bmatrix} - \begin{bmatrix} \underline{\omega} \wedge \underline{\underline{J}}_{off-diagonal}\underline{\omega} \\ \underline{0} \end{bmatrix} - \begin{bmatrix} \underline{0} \\ \underline{M}_{app-C1} \end{bmatrix} - \begin{bmatrix} \underline{0} \\ \underline{M}_{app-C2} \end{bmatrix} \right) \tag{2.33}$$

Terms $\underline{M}_{app-C2}$ and $\underline{M}_{app-C1}$ in Equation 2.33 refer to added masses moments that are written as stated in Equation 2.34 and 2.35. [10]

$$\underline{M}_{app-C1} = \underline{x}_{C_1} \wedge (\underline{\omega} \wedge (\underline{\underline{M}}\underline{v} + \underline{\underline{J}}_{off-diagonal}\underline{\omega})) + \underline{x}_{C_2} \wedge (\underline{\omega} \wedge (\underline{\underline{M}}\underline{v} + \underline{\underline{J}}_{off-diagonal}\underline{\omega})) \tag{2.34}$$

$$\underline{M}_{app-C2} = (\underline{\omega} \wedge \underline{x}_{C_1}) \wedge (\underline{\underline{M}}\underline{v} + \underline{\underline{J}}_{off-diagonal}\underline{\omega}) + (\underline{\omega} \wedge \underline{x}_{C_2}) \wedge (\underline{\underline{M}}\underline{v} + \underline{\underline{J}}_{off-diagonal}\underline{\omega}) \tag{2.35}$$

Kinematics model

The representation of the parafoil attitude kinematic is performed by means of quaternions, Equation 2.36. This choice is due to avoid the singularity that afflicts the Euler angles representation. Singularity that could be experienced during parafoil inflation. Depending on the value of C_{m_q}, the pitch angle could get very close to $-\frac{\pi}{2}$.

Computational speed is also affected positively by the presence of sole algebraic relations during integration.

The signs of the matrix in Equation 2.36 are related to the relative orientation of the inertial and body axes, Figure 2.1.

$$\underline{\dot{q}} = \frac{1}{2}\begin{bmatrix} 0 & -\omega_3 & -\omega_2 & -\omega_1 \\ \omega_3 & 0 & -\omega_1 & \omega_2 \\ \omega_2 & \omega_1 & 0 & -\omega_3 \\ \omega_1 & -\omega_2 & \omega_3 & 0 \end{bmatrix} \underline{q} \tag{2.36}$$

The quaternion representation of the attitude allows to get results closer to the reality than using the Euler angles. As shown in Figure 2.14 the model oscillates more and peak values are closer to the real ones.

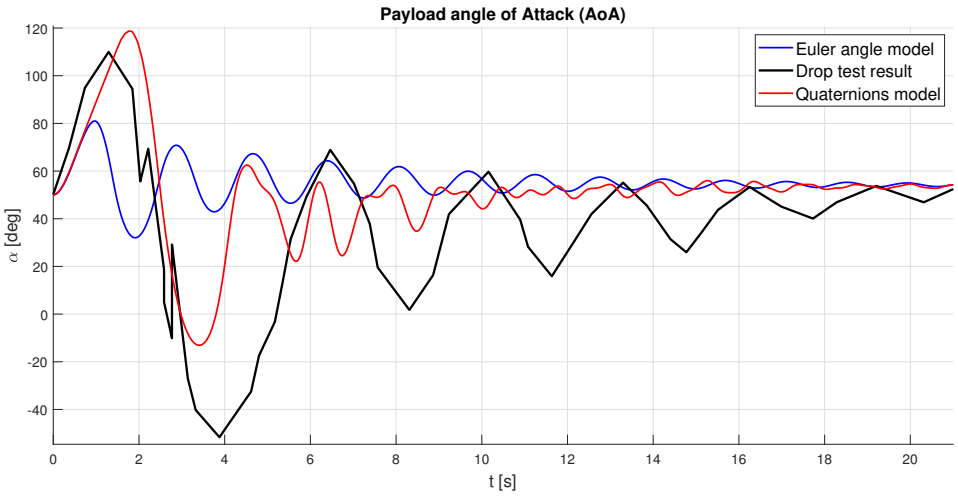

FIGURE 2.14: Model comparison with real drop test data

As far as the position in the inertial frame is concerned, it is possible to retrieve its behavior with respect to time from the body velocity, Equation 2.37. The $\underline{\underline{L}}_{IB}$ matrix is the direct cosine matrix representation of the attitude and it is retrieved at each time step from the quaternions.

$$\underline{\dot{x}} = \underline{\underline{L}}_{IB}\underline{v} \tag{2.37}$$

Kinematic model plus dynamic model give the evolution in time of all the 6 DOFs of the parafoil.

2.2 Payload

The payload is represented as a rigid body. The main difference from the parafoil model is the absence of added masses effects: being the wing load higher than $50\frac{N}{m^2}$ the added mass can be neglected. It allows not to consider the terms $\underline{M}_{app-C2}$ and $\underline{M}_{app-C1}$ and also to decouple the translational and rotational dynamic, Equation 2.38.

$$\begin{aligned} \underline{\underline{M}}\dot{\underline{v}} &= \underline{F} \\ \underline{\underline{J}}\dot{\underline{\omega}} &= \underline{M} - \underline{\omega} \wedge \underline{\underline{J}}\underline{\omega} \end{aligned} \tag{2.38}$$

The inertia properties and the aerodynamic forces generated by the payload are not listed in the present work because they represent the SpaceRider vehicle, thus they are subjected to secrecy policy of Thales Alenia Space. The only known data is the mass of the vehicle of 2550 kg as reported in [2].

In Section 3 several studies are presented: the payload inertia properties will be retrieved from References, while aerodynamic data will be considered only if they are clearly stated in References, otherwise the dead-mass assumption (payload generates only weight) is considered.

Kinematics are treated in the same way described in Section 2.1.5.

2.3 Connection lines

The connection between payload and parafoil consists of a riser and four bridles in a swivle configuration Figure 2.1, in order to re-use the same connection lines strategy of the precedent mission IXV, lowering costs in this way. The suspension lines are not accounted as connection lines because they are modeled as part of the parafoil rigid body.

Due to the presence of four bridles, the loads on the system will not be evenly divided on each bridle: at some instants one or more of them could be slacked and the loads transmitted only through one or two bridles. This phenomenon can be represented only with a 12 DoFs representation, Figure 2.15.

Because of the present connection lines design, it is not possible to determine in an analytic way the tension in the bridles, id est to do a projection of the riser force in bridle directions. Thus a numerical approach is followed: a Newton-Raphson zero-search algorithm is employed to find the equilibrium in S_1. The unknown data is the S_1 position while the equilibrium is obtained by means of riser and bridles tension. It is worth noting that bridles and riser have been modeled as elastic springs (Table 2.4) working only when they are pulled because they can not sustain loads in compression. A check is done to control that each bridle is in tension, if not, its force is not accounted in the equilibrium search.

$$F_{tension} = k \quad \Delta l + \mathbf{c} \quad \frac{\Delta l - \Delta l_{previous}}{\Delta T} \tag{2.39}$$

TABLE 2.4: Connection lines parameters

	Riser	Bridles
k [$\frac{N}{m}$]	220000	220000
c [-]	0.2 $\mathbf{c}_{critical}$	0

The term $\mathbf{c}_{critical}$ shown in Table 2.4 is the critical damping coefficient and it is computed with the assumption of spring-mass system: $\mathbf{c}_{critical} = 2 \quad \sqrt{mk}$.

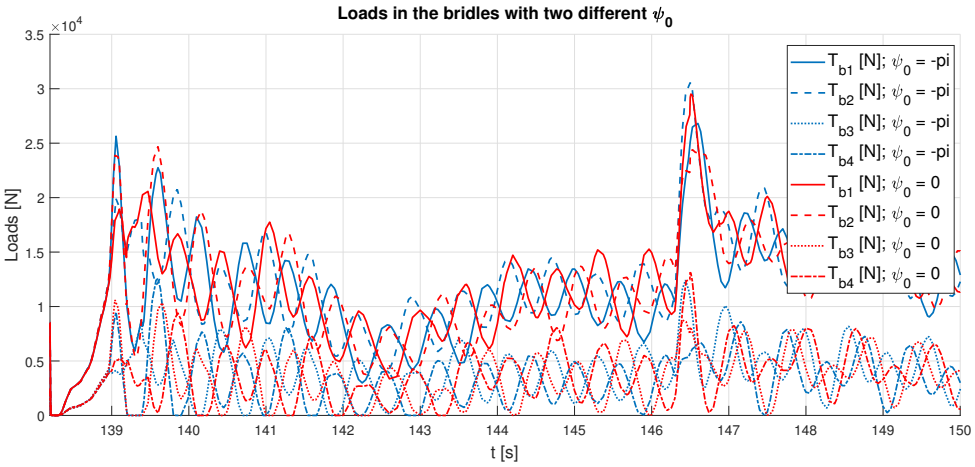

FIGURE 2.15: Tension in the bridles

Figure 2.15 shows how different bridles of the same simulation are subjected to different loads (lines of the same color). It is also shown how different initial ψ_0 induce different loads at the deployment, considering the same bridle (same line format but different colors).

2.4 Parachute extraction

During extraction the parachute is completely decoupled from the payload. Indeed they are moving like two separate objects because there is not a line taut by now, so there is no tension along the lines. Instead of neglecting this phase, imposing a time step *a priori*, a reduced DoFs dynamic model is implemented. While the parachute is still in its bag, the whole system parachute-bag can be modeled as a point mass, where the mass will be only the real one of fabric plus suspension lines and bag (no apparent mass effect). In this way the DoFs of the system are reduced to the translational motions, Equations 2.40 and 2.41. Note that the initial conditions of the velocity could be different from zero. This can be useful in order to study a mortar ejection (i.e. to eject the first parachute stage) so that an initial ΔV can be imposed. Alternatively an impulse force can be imposed.

$$m_{BP}\dot{\underline{v}} = \underline{F}_{aer} + \underline{F}_g + \underline{T}_{pp} \tag{2.40}$$

$$\dot{\underline{x}}_{BP} = \underline{\underline{L}}_{IB_{BP}}\underline{v} \tag{2.41}$$

The term $\underline{T}_{pp}$ in Equation 2.40 refers to the tension that the previous parachute exerts on the bag to pull out the next parachute stage.

TABLE 2.5: Extraction model values

	Time to line taut [s]		Relative velocity at line taut [m/s]		Previous parachute pulling force [N]	
	No bag extraction	Bag extraction	No bag extraction	Bag extraction	No bag extraction	Bag extraction
Supersonic drouge	0.1	0.411	5	58.64	0	0
Subsonic drouge	0.5	0.123	0	23.44	0	7572.6
Main chute	0.5	0.498	0	96	0	12327

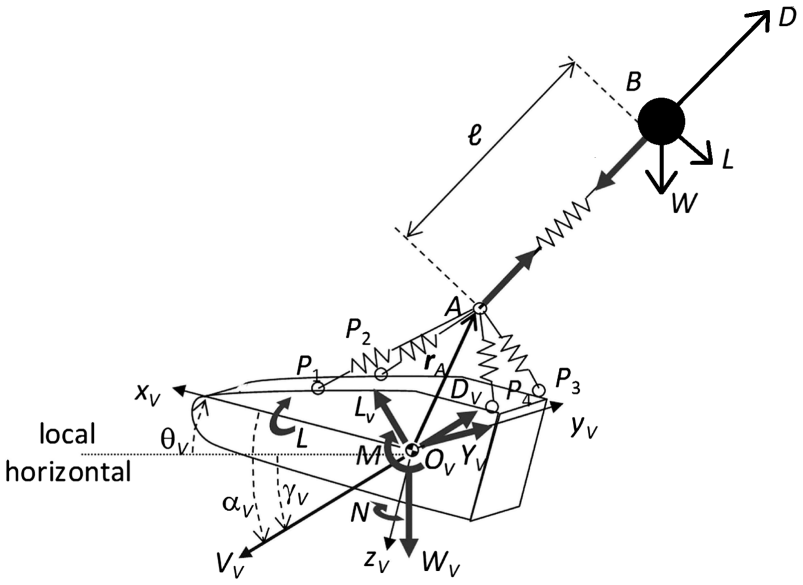

FIGURE 2.16: Bag extraction representation

The integration of the separate parachute and payload dynamic equations is performed when line taut is reached. Line taut is obtained when the difference between the point mass position and the payload position is equal to the connection line plus suspension line lengths, Equation 2.42. Right now the two bodies begin to interact and a peak load is usually experienced at line taut. When using this model the line taut peak is neglected but it is acceptable because the major peak loads are always experienced at the inflation of the parachute/parafoil so the sizing of the connection lines on these loads guarantees the integrity at the line taut loads.

$$||\underline{x}_{BP} - \underline{x}_v|| \geq l_{riser} + l_{susp-lines} \tag{2.42}$$

The present approach allows to have a more flexible and precise model: the simulation is re adapted at the change of the boundary conditions (i.e. initial conditions, characteristics of the parachutes, deployment logic). Of course these additional simulations increase the overall computational burden.

In Table 2.5 the values of extraction times and the supersonic drouge parachute velocity at line taut are consistent with the experimental data of the IXV mission [1], while the value of the relative velocity at the last line taut is too high to have physical meaning. It is due to the limitation of the present model which assumes the force of the previous parachute acting with constant modulus on the bag-parachute. The force indeed changes its value because it is a dynamic problem involving three bodies: the previous parachute stage, the bag-parachute and the payload. In order to avoid additional computational burden and since extraction times are acceptable, no further bodies were added to the simulation.

Chapter 3

Validation of the model

The simulator is a tool ensuring realistic data, therefore a check on the quality of the results must be done. Not having the possibility to test the algorithms and the model in flight, the validation was performed reproducing the data given by other thesis, works or space programs. Being the simulator focused on reproducing accurately both trajectory and loads two validations will be done and presented in this Chapter: one at steady-gliding and the other at the inflation dynamic, Figure 3.1. If both the analyses estimate correctly the expected values within a certain threshold of error, then the simulator can be considered *"validated"*.

FIGURE 3.1: Validation logic flow chart

The aim is to validate the 12 DoFs dynamic model, it means that the control action has not yet been applied. It worths noting that all the analyzed studies are models with less DoFs (usually 9 or 6 [23] [6] [20]), thus the present validation can not be considered enough to directly apply the simulator to the design of the SpaceRider parafoil. A drop test with a flight model is mandatory to validate the model.

In some cases not all the data needed to perform a simulation were available, so sensitivity analyses on the unknown parameters were performed.

3.1 Steady-glide validation

Most of works are centered on the post inflation flight analysis of the parafoil-payload system, because they are mainly focused on implementing a GNC algorithm and testing it. For example in Scheuermann's work [20] the flight test isn't performed with a drop test but, having an engine attached to the payload which is turned off at a determined altitude, the inflation and transitory phase can not be checked.

On the basis of the data reported in Scheuermann's work [20], some simulations were performed in order to have a sensitivity analysis on the parameters not reported and related to the suspension lines. The following data are not given:

- length of riser and bridles
- connection points position
- rigidity of the bridles and riser

A simplification of Scheuermann's model was also made: the payload does not generate any aerodynamic force, it only acts as a dead-mass.

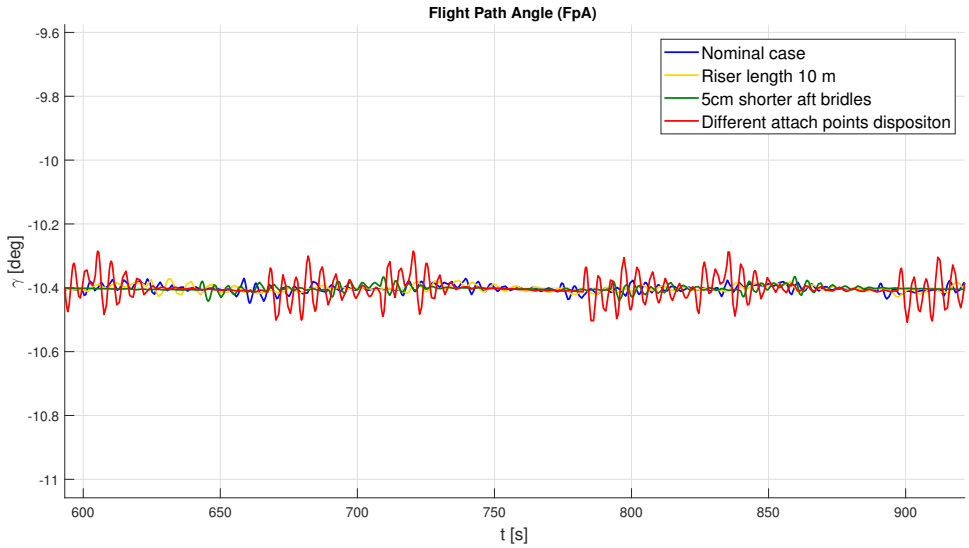

FIGURE 3.2: Flight path angle comparison

TABLE 3.1: Results comparison between simulation and steady state values of van der Kolf

Parameter	Reported value	Simulation result	Relative error [%]
$\|\|V\|\|$ [m/s]	13.94	14.21	1.93
V_h [m/s]	12.99	13.11	0.92
V_v [m/s]	5.14	5.49	6.8
γ [deg]	21.63	22.73	5
Payload α [deg]	15.52	16.57	6.7
Payload θ [deg]	-6.11	-6.16	0.8

The simulations show how the connection lines do not affect the attitude of the parafoil and thus the trajectory, Figure 3.2.

Of course this is true only if the previous assumption of dead mass payload is true. Indeed the attitude of the payload is strongly affected by the connection lines disposition, as shown in Figure 3.3.

The most important parameter reported by Scheuermann is the nominal flight path angle, the value of $10deg$ [20] is checked with simulation results. The difference between them is 3.85% and it is acceptable knowing the assumption.

Another sensitivity analysis was performed using the CIMNE data as Reference [8]. Knowing that the suspension lines do not affect the trajectory under assumption of dead-mass payload, the focus of this sensitivity analysis was upon longitudinal dynamic. Indeed the C_L and C_D are given but the C_m is not. The sensitivity analysis is necessary to have an insight of how much the C_m is going to affect results.

As shown in Figures 3.6 and 3.5 the value of C_m greatly affects results, because it changes the AoA at which the system trims itself.

Figures from 3.7 to 3.9 show the results reported by [23] compared to the ones obtained by the simulator developed in the frame of the present work.

To perform an additional check, the thesis [6] was reproduced. As shown in Table 3.1 the values reported by Gideon van der Kolf are well represented by the simulator: with a maximum error well below 10%.

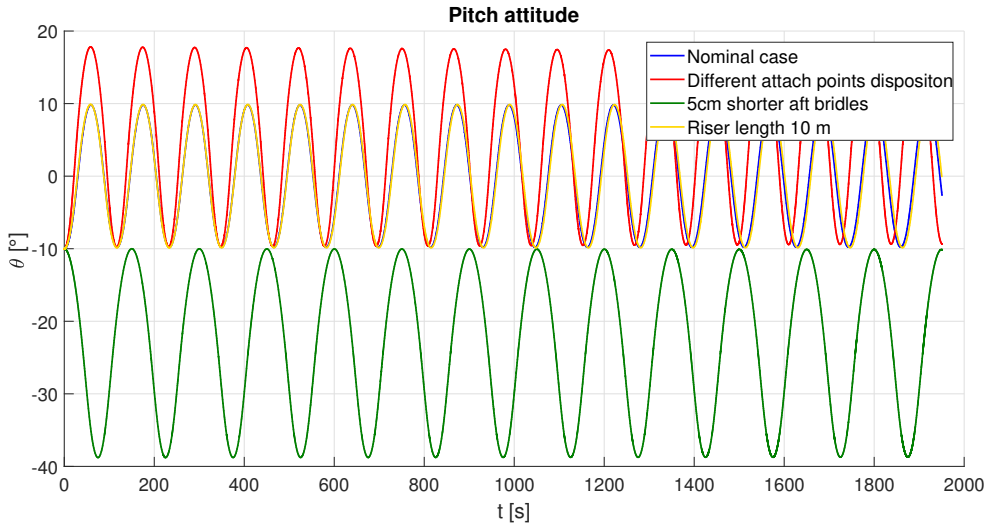

FIGURE 3.3: Payload attitude sensitivity analysis results

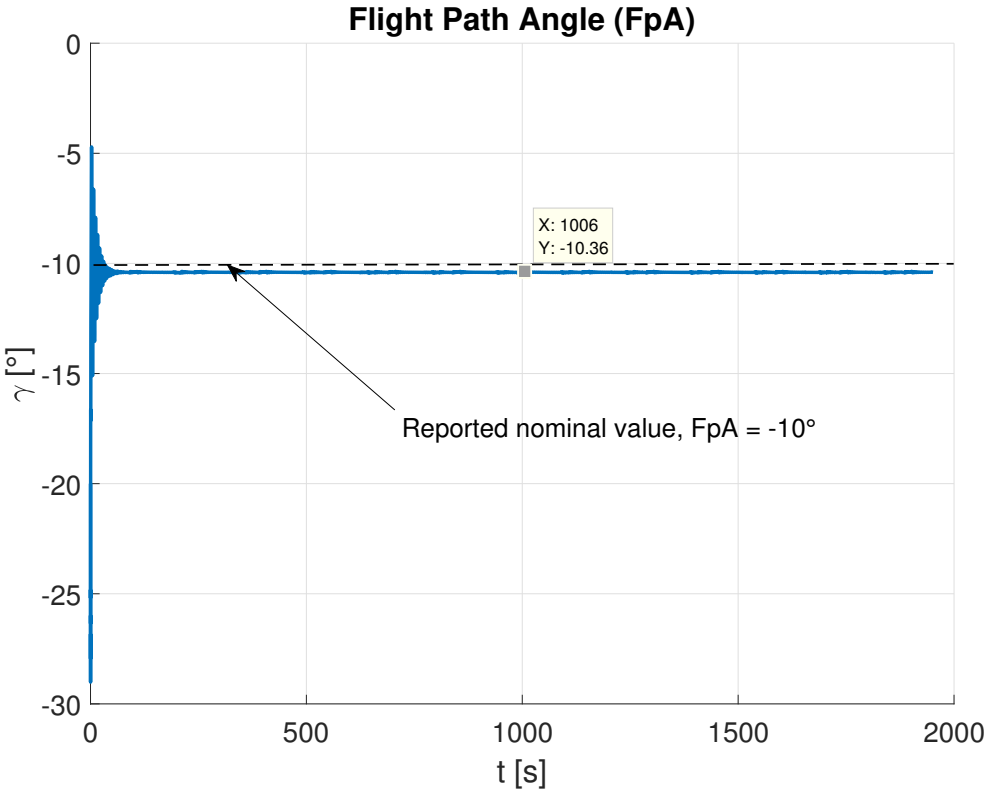

FIGURE 3.4: Flight path angle comparison

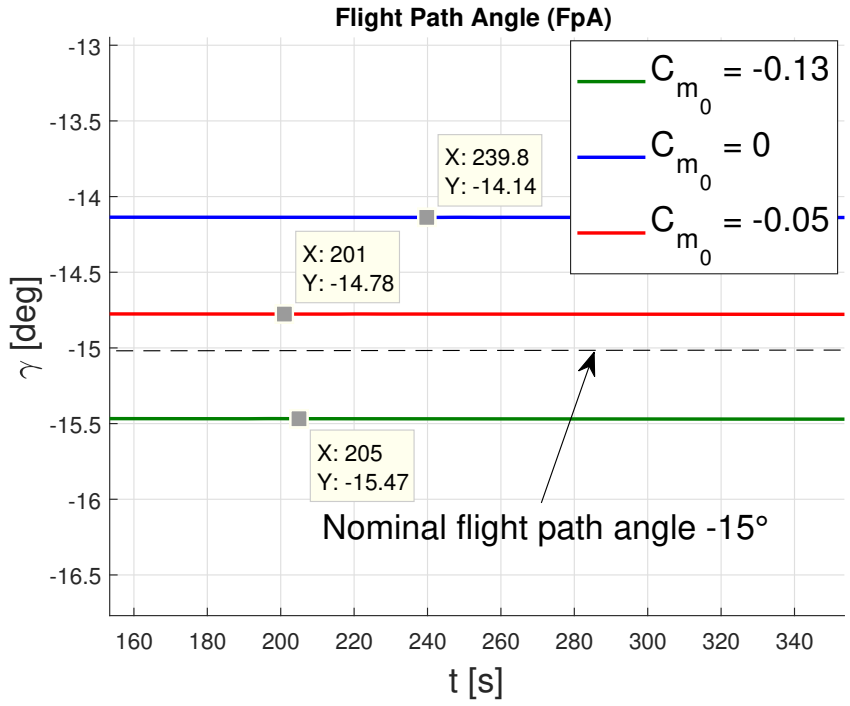

FIGURE 3.5: Flight path angle sensitivity analysis

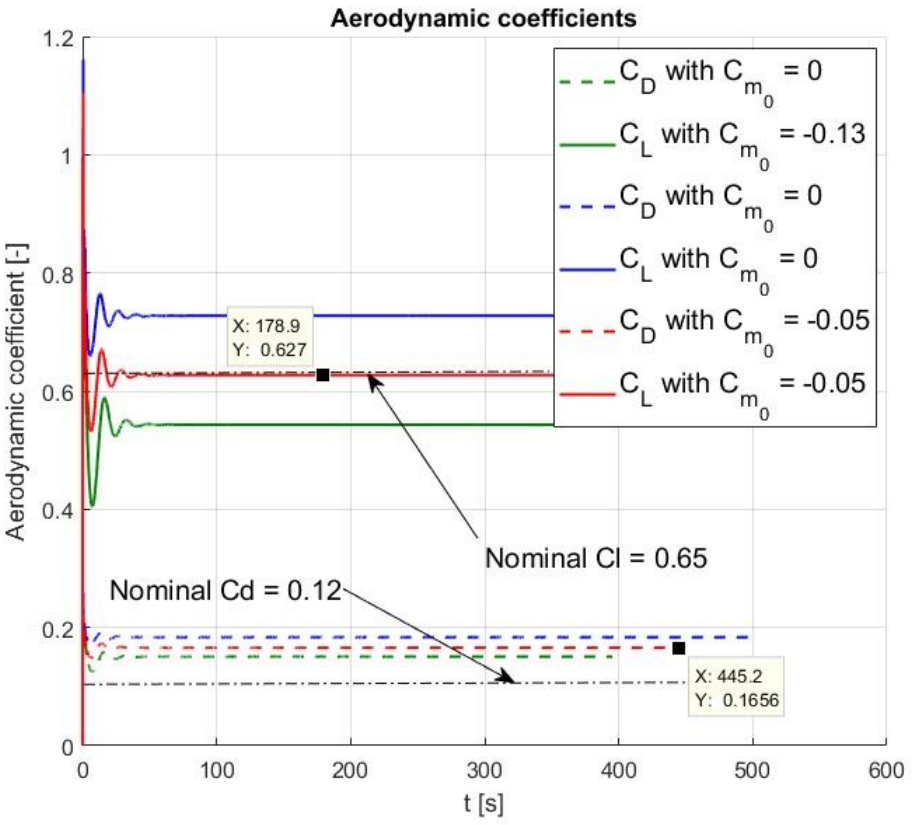

FIGURE 3.6: Aerodynamic coefficient sensitivity analysis at steady state

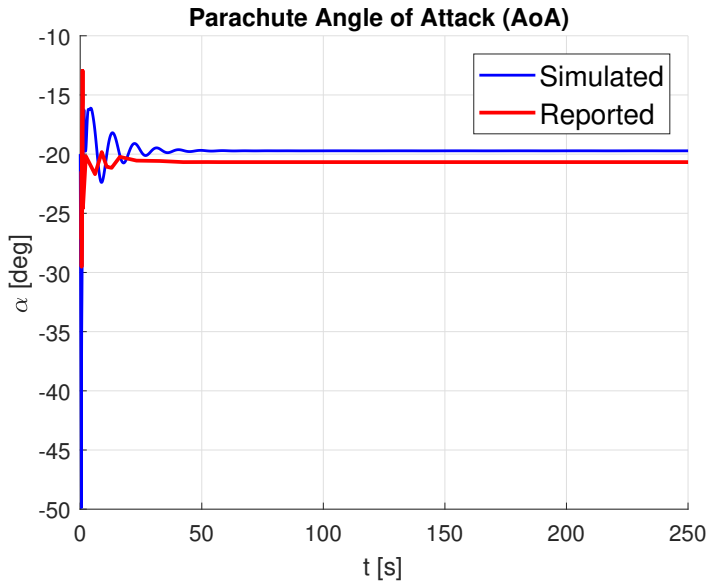

FIGURE 3.7: AoA time evolution reported and simulated

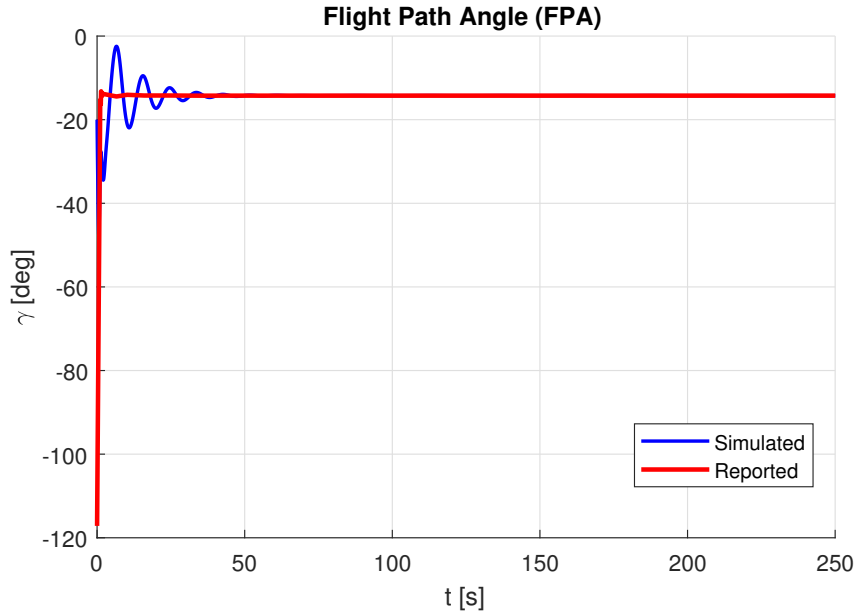

FIGURE 3.8: γ time evolution reported and simulated

3.2 Inflation validation

Previous reported cases were all focused on the trajectory analysis. To validate dynamics at the inflation, an analysis was made comparing simulation results and flight data of the X-38 drop tests.

This kind of analysis is very important in order to use the simulator to size the riser and bridles. The main loads are experimented during inflation and the highly dynamic nature of the event make them very difficult to be correctly represented.

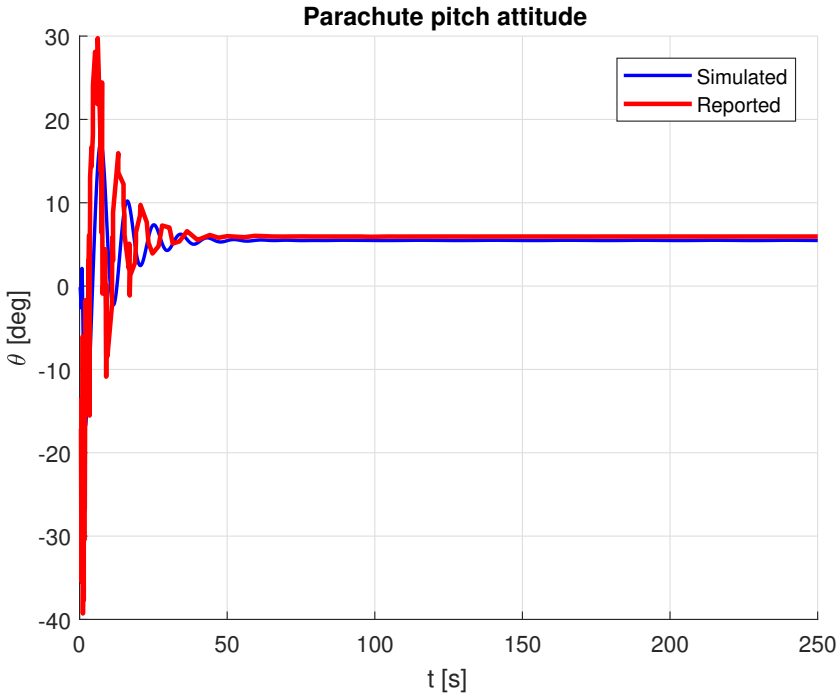

FIGURE 3.9: θ parafoil time evolution reported and simulated

3.2.1 X-38 drop tests $7500 ft^2$ parafoil

The reference drop test is P3D5, above all because its aerodynamic data are deeply analyzed and reported in [4].

In flight tests, during inflation, the transition from an angle of attack of 90 deg to 0 deg occurred in 2 seconds [4]. As shown in Figure 3.10 the transition time is equal to $2.13s$.

After full inflation parafoil trims itself to a nominal value of $-8.5deg$ [4], Figure 3.11 shows how the simulation result is very close to the real value: an error of less than 2%.

The full inflation of the X-38 parafoil is reported to last from 20 to 30 sec [4], in the simulation the deployment takes $18.91s$ as shown in Figure 3.12.

Oscillations experienced by the X-38 model during inflation are reported to be within $-70/35deg$ [4]. The simulation overestimated these oscillations as reported in Figure 3.13. Figure 3.13 also shows that X-38 in simulation oscillates with a higher frequency compared to the one of the real drop test experiment. It can be related to unknown values of the riser damping coefficient or C_{m_q}, as shown in Figure 3.14.

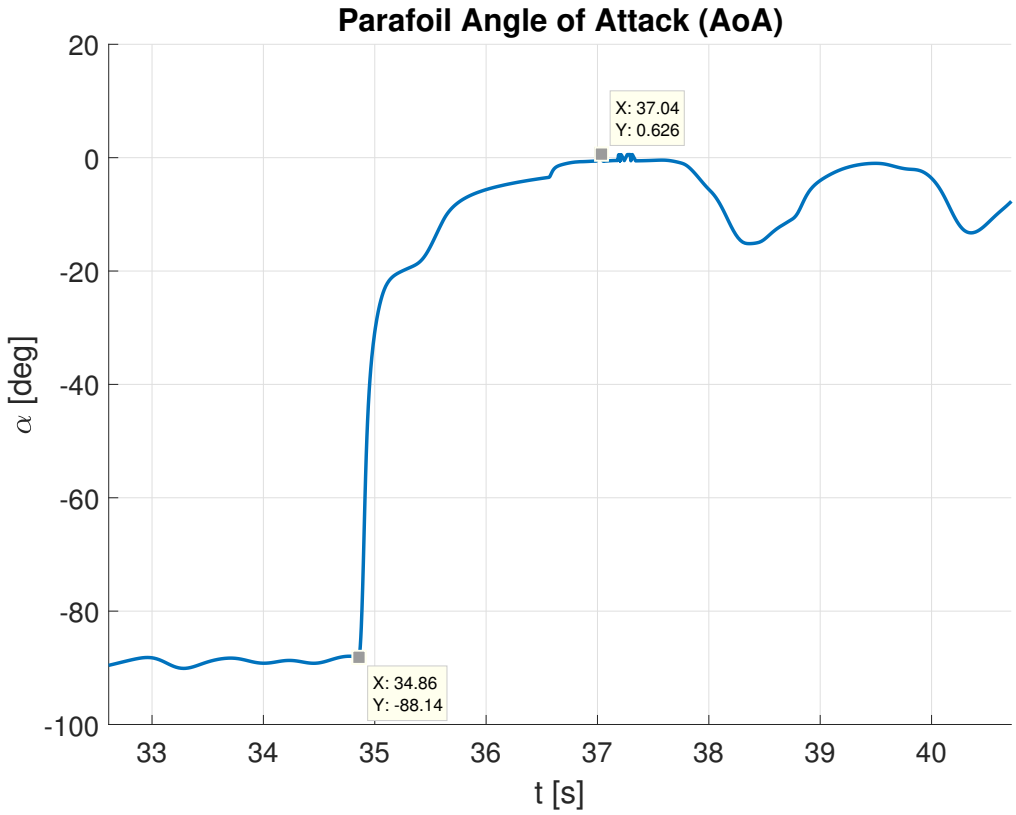

FIGURE 3.10: AoA transitory

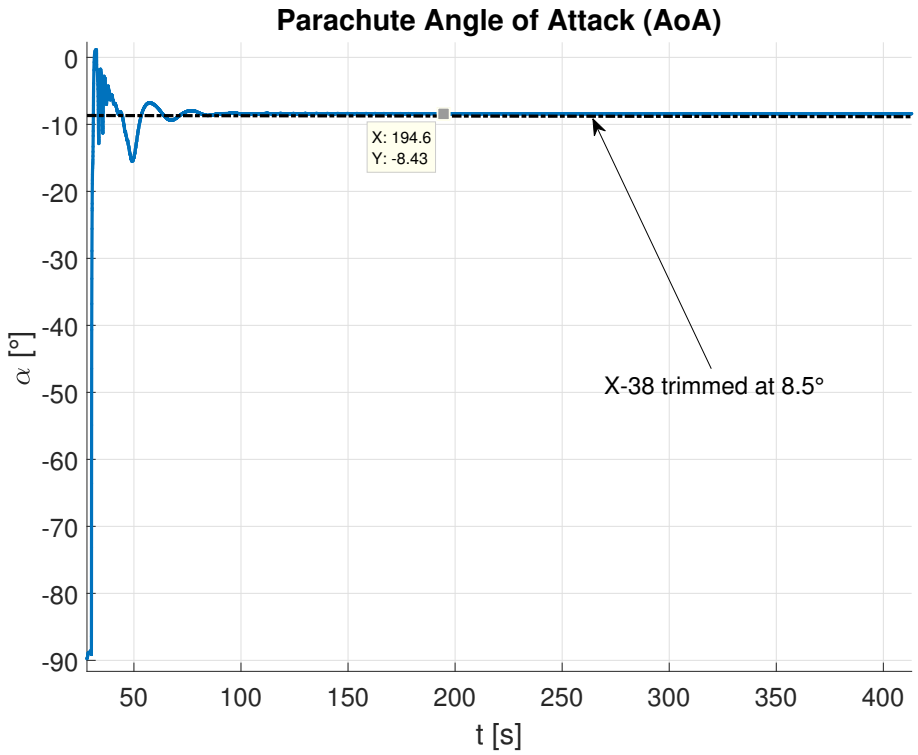

FIGURE 3.11: AoA steady state value

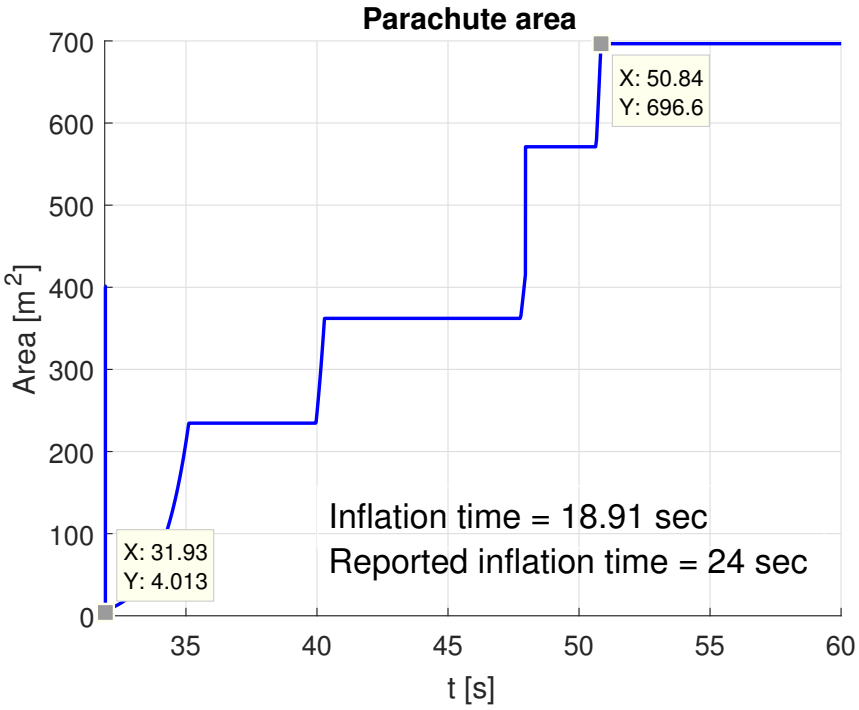

FIGURE 3.12: Parafoil area inflation

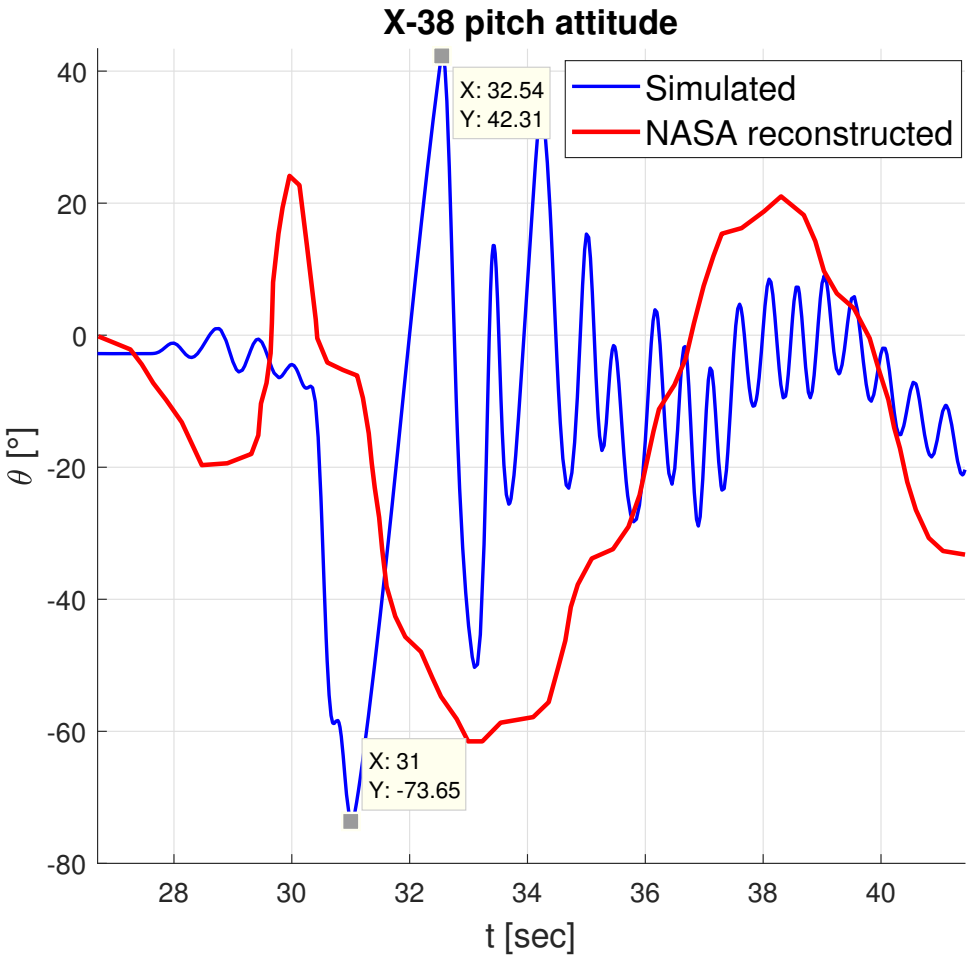

FIGURE 3.13: X-38 pitch oscillations

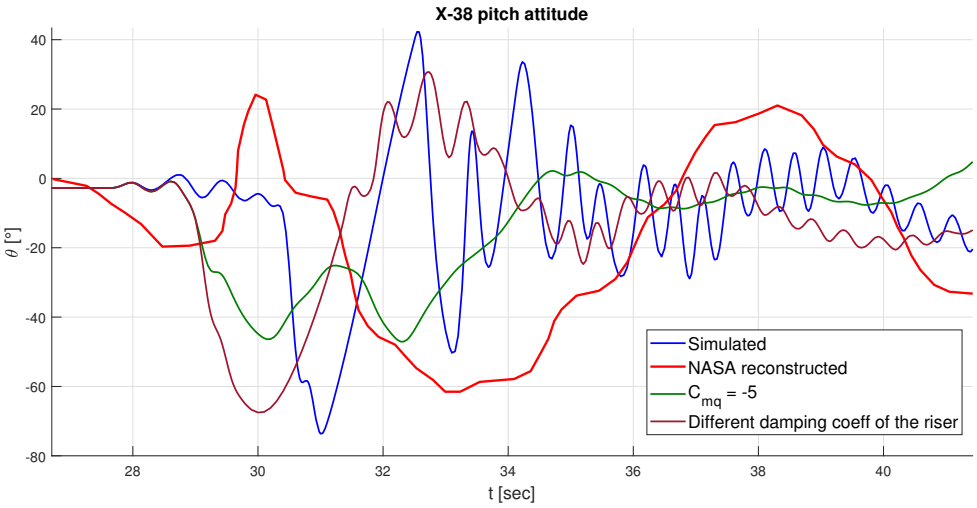

FIGURE 3.14: X-38 pitch oscillations sensitivity analysis

The most critical values overestimated by simulations are the accelerations experienced by the payload. They are reported to be 4 g's for the first reefing stage and from 2.5 to 1.5 g's for other stages [15]. In simulations instead a value of 4.2 g's is computed for the first stage and from 2.4 to 2.2 g's for other stages, Figure 3.15.

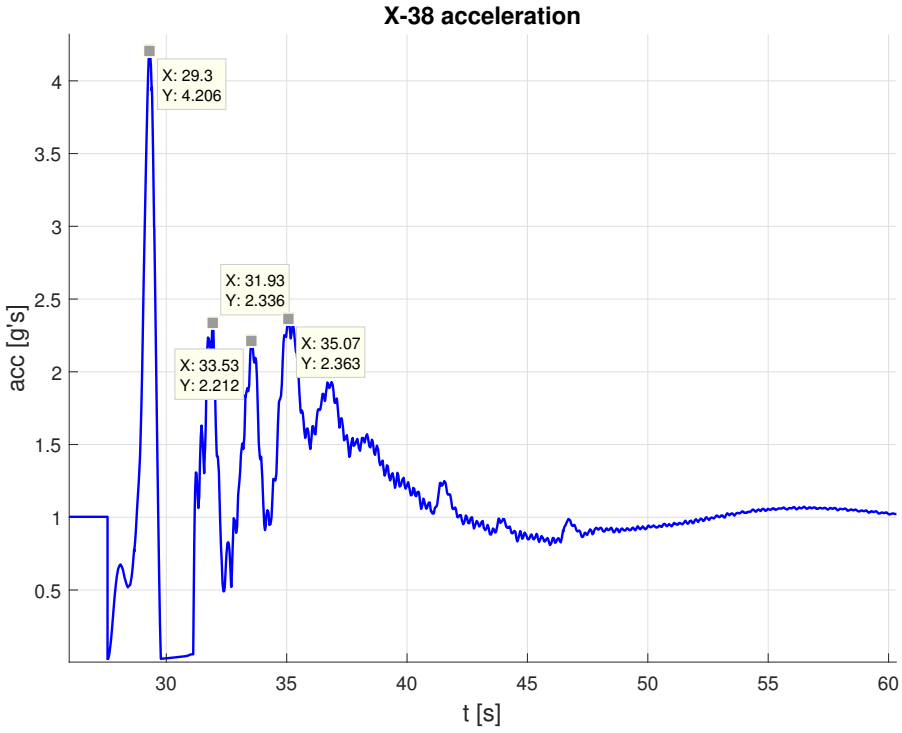

FIGURE 3.15: X-38 accelerations

The simulator correctly represents the steady state but it overestimates accelerations during inflation. This is probably due to both the differences of the the payload drag data and the density value.

3.2.2 US Army 4200 parafoil drop test

The drop test LCWW-2 done by Pioneer for the US Army in the frame of the JPADS program is here reproduced.

The focus of the validation is again on the reproduction of the inflation loads. Knowing that the payload in this case was a cradle plus a mock-up of a military vehicle, the entire test was reproduced: both drogue and parafoil are reefed in multiple stages.

Loads depend on how much drag the payload generated, mainly for two reasons: firstly a bigger drag slows down all the system to lower velocities before parafoil openings, secondly a bigger drag reduces the velocity increment during the free-fall phase between drogue cut and parafoil deployment, Figure 3.16.

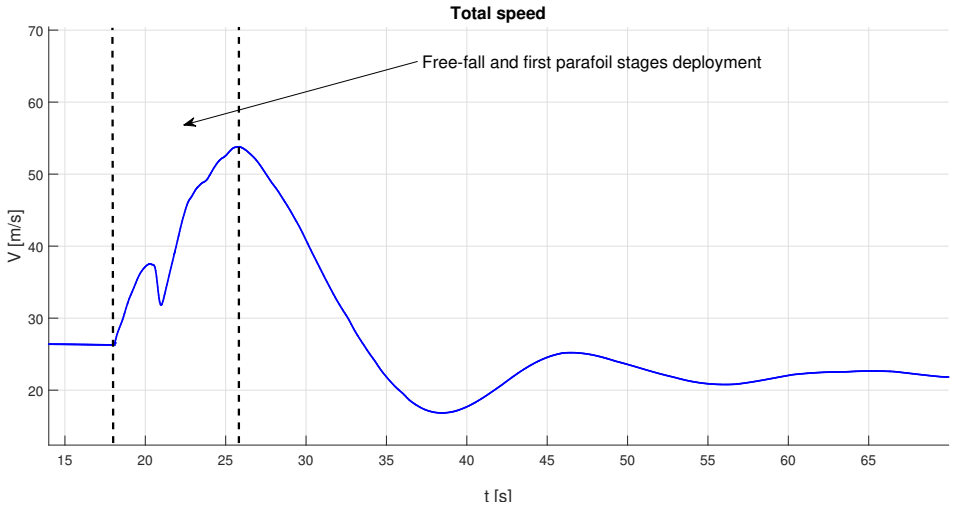

FIGURE 3.16: Payload total velocity

In order to have a correct representation of the drag, Equation 3.1 was used to compute the drag area. This is a standard formula for cradles.

$$C_D S_{AoA} = C_D S_{front} cos(\alpha) + S_{bottom}(1.1(sin(\alpha))^3 + 0.02) \tag{3.1}$$

The flight time is a little overestimated: almost 11 minutes instead of 10 minutes from the deployment. Mainly the error is due to the parafoil trajectory, being the drogue parachute cut at the correct altitude of 5029 meters after 18.1 seconds from aircraft release (instead of the 16 seconds reported [15]).

Some parameters are not known and their effect on the dynamic behavior of the system must be considered. A sensitivity analysis was carried out.

As shown in Figure 3.17 an important parameter which highly affects the inflation loads is the dimensionless time τ_0. As stated in Section 2.1.3 usually for free inflation parafoils τ_0 is equal to 3.5 but it was found out in the literature that this value can drop even to 2. The value of 2 allows to get a more comprehensive representation of the real drop test data.

Parameters characterizing the connection lines are the rigidity k and the damping coefficient $\mathbf{c}$. They are unknown data in the drop test reported in [5]. The effects on the loads by changing them are shown in Figure 3.18.

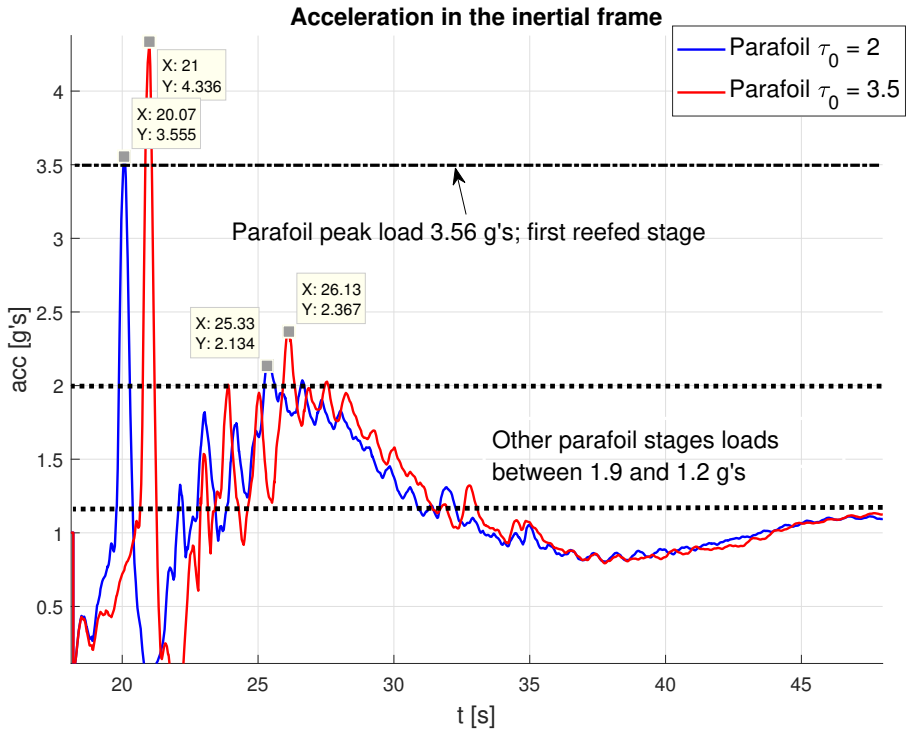

FIGURE 3.17: Payload accelerations

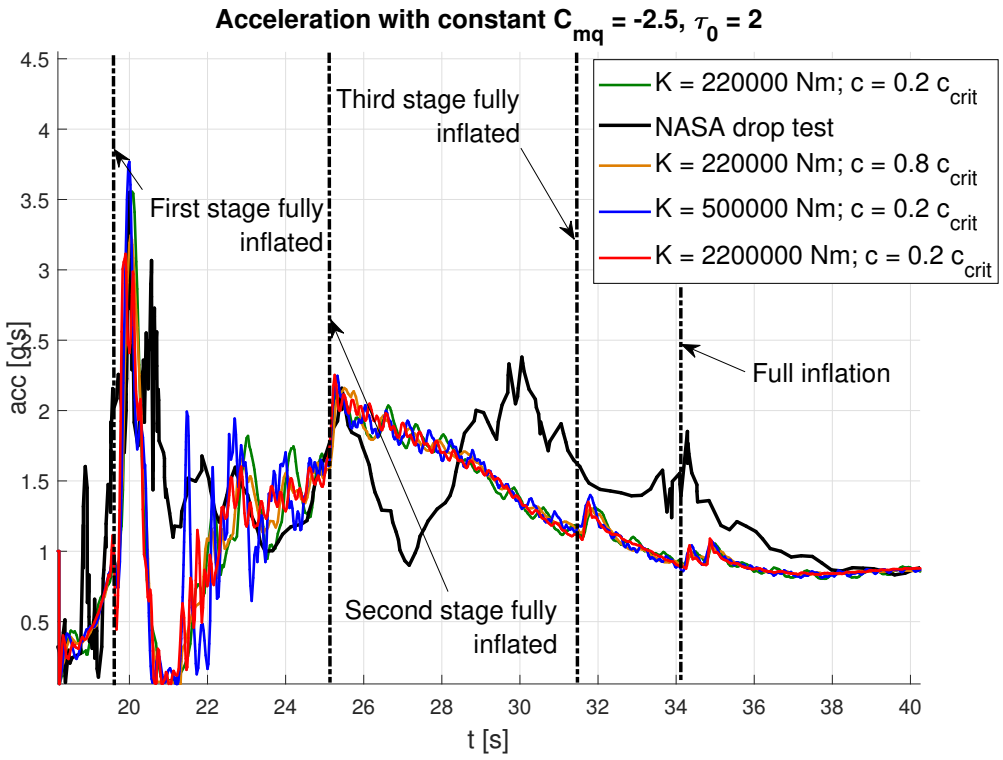

FIGURE 3.18: Connection line sensitivity analysis

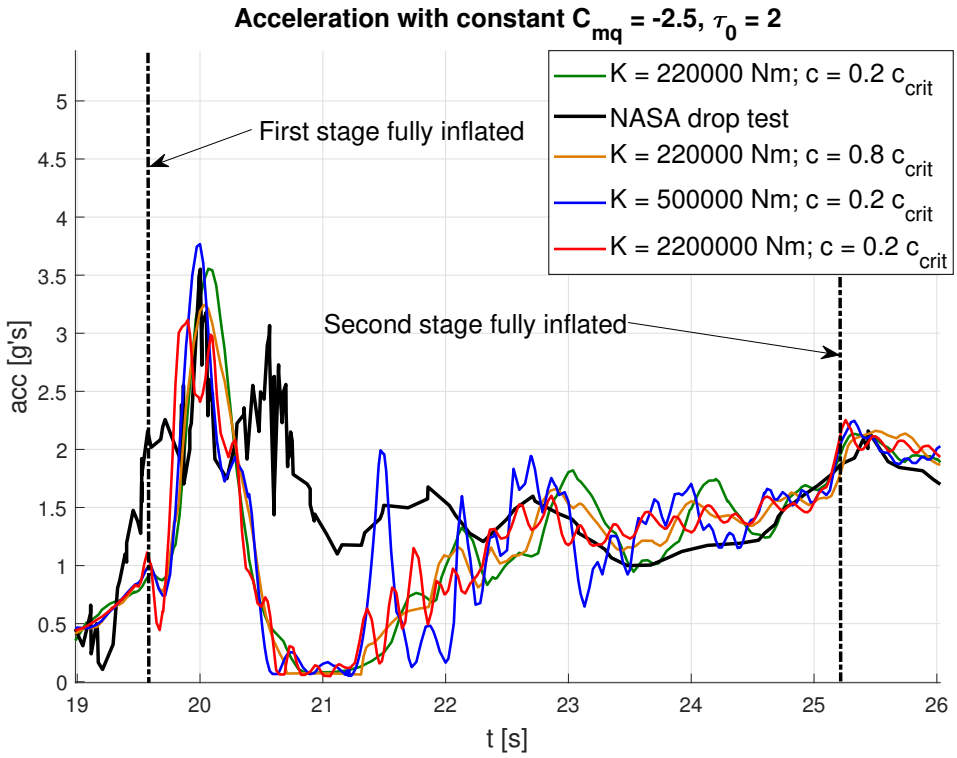

FIGURE 3.19: Connection line sensitivity analysis, zoomed on the first two stages

In the sensitivity analysis reported in Figure 3.18 the constant values are $\tau_0 = 2$ and $C_{m_q} = -2.5$. It can be noted how, increasing the value of K, it does not imply an increase of the loads experienced but it allows the generation of more spikes.

Figures 3.18 and 3.19 show that loads approach zero after the pitch down movement of the parafoil canopy; it is due to the lines slack, not experienced in the drop test, so the canopy should oscillate less. That's why a sensitivity analysis of the longitudinal damping coefficient variation was carried out maintaining τ_0, K and c costant, Figure 3.20. In case of $C_{m_q} = -5$ the lines do not slack because the parafoil does not reach an excessive pitch down attitude, but it can be noted how the peak load reaches a lower value.

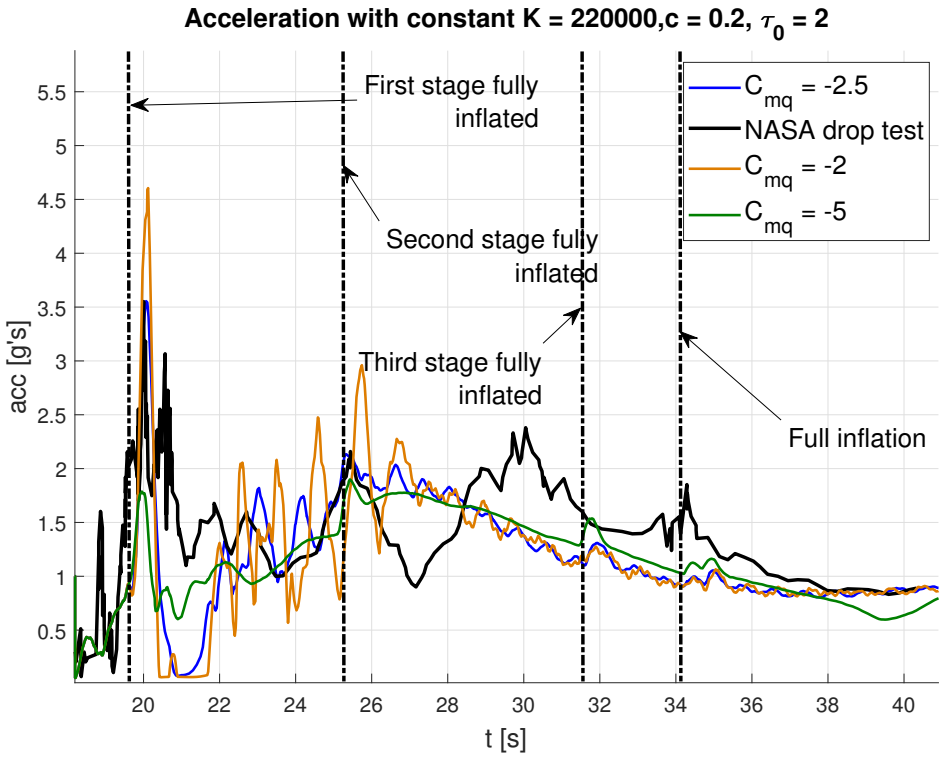

FIGURE 3.20: C_{m_q} sensitivity analysis

After completing these analyses, a tuning of the parameters can be done in order to reproduce the exact dynamic of the drop test, checking that all parameters remain in a physical feasible range of values. The result is shown in Figure 3.21.

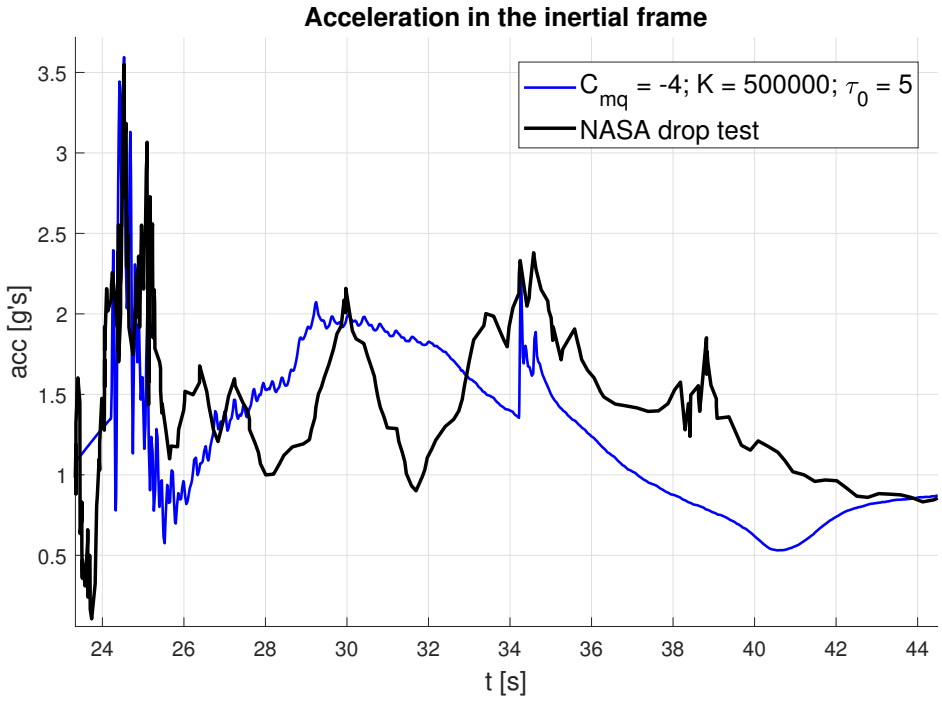

FIGURE 3.21: Closest result to the real drop test

Figure 3.21 shows that at the beginning the real values are well represented but, before reaching steady state, the simulated values are different from the real ones. The reason is probably related to the value of C_{m_q}. Indeed in the simulation C_{m_q} is supposed to be constant while in reality it probably changes. Unfortunately no aerodynamic studies were carried out on the topic, NASA studies [19] proved that static aerodynamic coefficients like C_L, C_D, C_m change during inflation, so it is possible to suppose that even aerodynamic damping coefficients change their values.

Chapter 4

Guidance Navigation & Control

In this chapter the GNC system will be dealt with. The possibility to steer the parafoil-payload system, applying a control action, is the real attractive feature of the parafoil respecting to a ballistic parachute.

The system logic flows like shown in Figure 4.1. In the same manner it will be shown in the following pages.

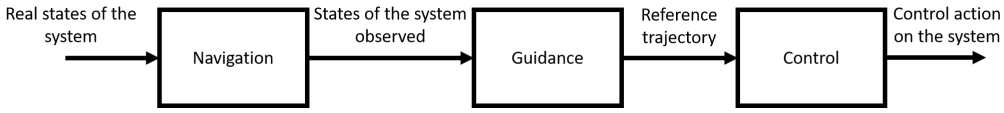

FIGURE 4.1: GNC flow chart

Firstly the Navigation gives an estimate of the states of the system that are needed to the Guidance, Section 4.1. Then the Guidance elaborates a feasible trajectory to get to the landing target or (if not possible) as close as possible to it, Section 4.2. Lastly the Control tries to make the system follow the trajectory given by the Guidance, Section 4.3.

Two types of control are possible in a parafoil: the longitudinal one and the lateral-directional one. The lateral-directional control allows the system to steer itself in the XY-plane. The longitudinal control allows to manage the FpA, the GS and so the remaining time of the flight.

4.1 Navigation

Having not yet available the system architecture of the SpaceRider, a set of instruments must be supposed to model the Navigation subsystem.

Looking also at other works [20] and also reasoning on the topic, it is straight forward to assume that the most important quantities to be used by the Guidance will be an estimation of:

- Position of the system and of the target in the 3D space, it can be provided by a GPS unit
- Velocity, both in modulus and direction, it can be retrieved by a GPS unit or by a Inertial Unit (IMU) or a combination of both

It is supposed that the measurements are affected by white Gaussian noise. So the estimated states will be a superposition of the real ones plus the noise contribution, Equation 4.1.

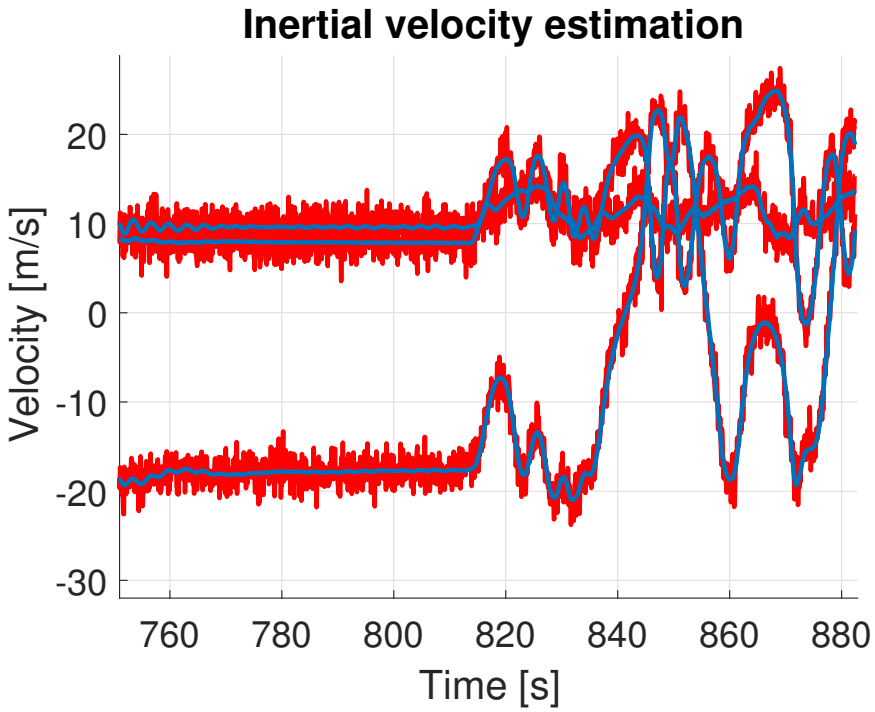

FIGURE 4.2: On board estimated inertial velocity, in blue the real states, in red the estimated ones with $\sigma = 2m/s$

$$\underline{x}_{obs} = \underline{x}_{real} + \underline{x}_{noise} \tag{4.1}$$

The parameter $\underline{x}_{noise}$ used in Equation 4.1 is related to the accuracy of the instruments on board. Supposing to have a GPS unit, the parameter values used in the simulations are Table 4.1.

TABLE 4.1: Standard deviation values used

	Position [m]	Velocity [m/s]
σ value	10	0.2

If multiple instruments are used, a method to combine the informations must be implemented and used. It could be useful to combine the IMU with the GPS in order to filter out the noise of GPS measurements.

The value of σ for the velocity estimation in Table 4.1 is the one expected for a SpaceRider-like mission, the white Gaussian noise is going to act differently on each component: meaning that this will going to affect not only the magnitude of the velocity estimated but also its direction. Figure 4.4 shows a sensitivity analysis that demonstrates the accuracy of the GNC algorithm is not compromise until the σ_{vel} value remains below $2.1m/s$, that is approximately 10% the value of the flight velocity.

The wind is supposed to be estimated on board by the system, this will have some consequences as shown in Section 5.2.

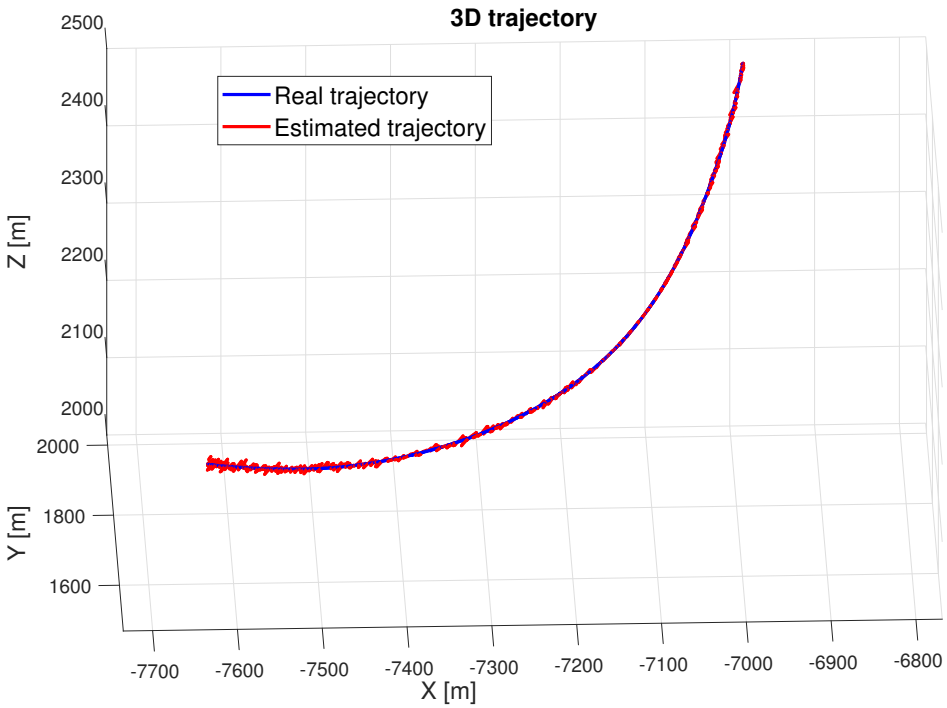

FIGURE 4.3: On board estimated trajectory

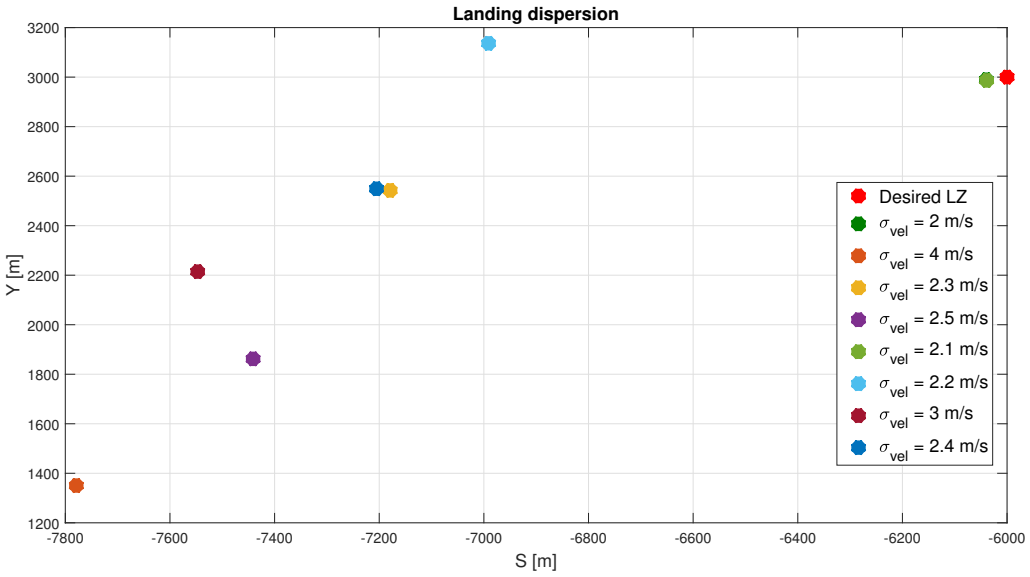

FIGURE 4.4: Sensitivity analysis changing σ_{vel}

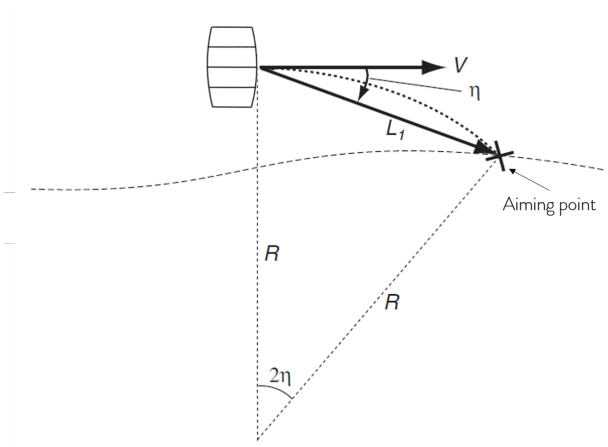

FIGURE 4.5: Lateral angular error definition [17]

4.2 Guidance

The Guidance can be considered decoupled in the lateral-directional plane and in the longitudinal plane in case of large canopies that are turn-rate limited. This was the case for example of X-38. [26] In case of small canopies, steep turns are going to affect also the FpA, thus the lateral motion will be coupled with the longitudinal one.

SpaceRider case can be well assumed to be a large-canopy one.

4.2.1 Lateral-directional Guidance

The lateral-directional Guidance has the aim to compute a trajectory to be followed in the XY-plane. In the present work two possibilities are given to the model user:

- to insert directly a 3D trajectory to be followed
- to let the system compute its own trajectory giving only the wanted landing point

The first option is important in the frame of the SpaceRider mission. Not only because there are multiple industrial actors, each of them with a specific task (the mission analysis and the control system could be assigned to a different companies) but also because, due to its practical application, it could be necessary to make some considerations on the path to be followed: i.e. to avoid populated areas or to have multiple possible landing points, as back up alternatives. In this case the Guidance will be limited to a path-following technique: the error to be given at Control will be computed as the angular displacement between the actual position and the wanted one at the next time instant.

The choice of the position of the point to be aimed is very important in this kind of strategy: a too close point could lead the Control to overreact continuously, a too far point could make the system to "cut short" on the path to be followed. In the present work the aiming point was chosen at a distance of 200 meters from the actual position.

The second option is the classical approach used for parafoil-payload systems: an adaptive Guidance allowing the system to be flexible and to compute its own trajectory depending on the wind direction. There are lots of possible adaptive guidance algorithms: Dubins paths [7], LQR aimed to minimize control effort, spiral loiter [23]

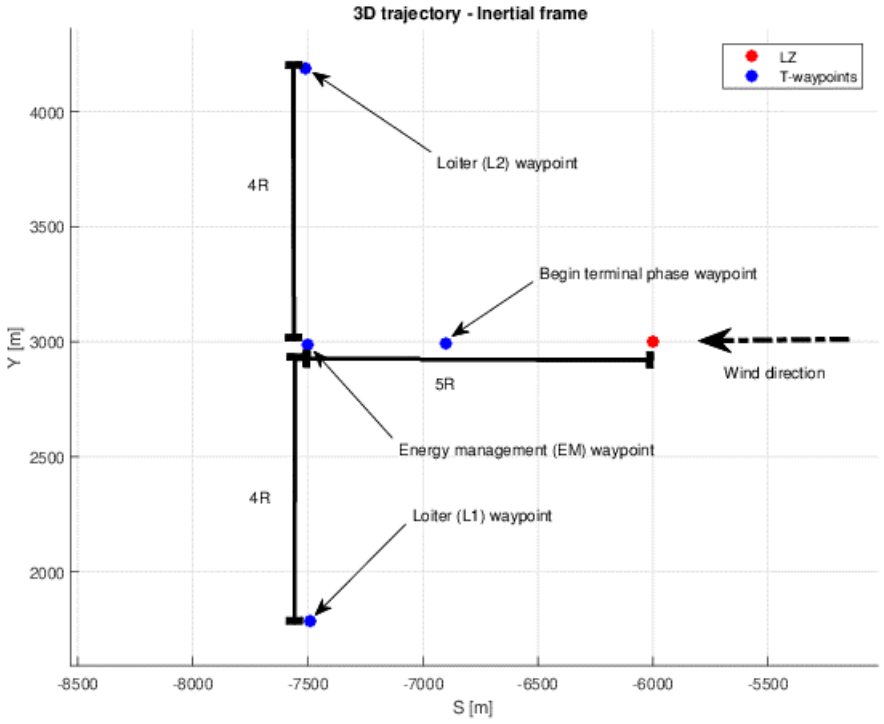

FIGURE 4.6: T-based approach

and so on [12]. All of them divide the flight path into four segments: homing, loiter, terminal guidance and flare.

The Guidance algorithm used in the present work is a T-based Guidance [11]. It is a simple and robust Guidance algorithm that can easily be implemented on board. It is a Guidance that is based on the definition of 4 way-points, the position of these way-points is computed with the information of the wind and of basic properties of the system.

First an initialization phase is needed. It can be a free-flight phase or usually an open loop full circle. In this phase an estimation of the wind velocity is performed looking at the drifting, due to the wind action. In the present work the initialization phase is considered through a free-flight time interval after inflation, in this way also oscillations due to inflation are let to damp.

After the initialization of the Control, the first control mode is homing: the system aims to the energy management way-point (EM). It is positioned at a distance of 5 standard radius of turning from the landing point in a downwind direction. The standard turning radius is computed as $\mathbf{R} = V/\omega_{std}$. Where flight velocity V and angular turning velocity ω_{std} must be known or estimated by the dynamic properties of the system.

After EM way-point is reached, the energy management phase is initialized: a check is done if the actual altitude of the system is more than the one needed to get to the landing point. If the actual altitude is equal or less than the one needed to get to the landing zone, a direct approach to the LZ is activated. Otherwise a loiter strategy is employed to lose altitude without getting too far from the LZ. The loiter phase consists of the system switching its aim between way-point L1 and way-point L2, Figure 4.6. This strategy is better than a simple circular loiter, Figure 4.7, because the circular shape of the pattern could lead to an uncontrollable parafoil situation

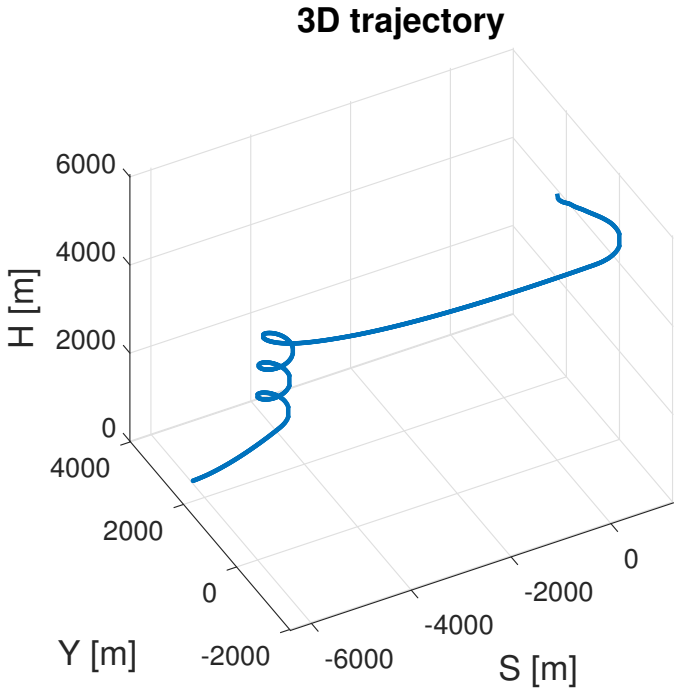

FIGURE 4.7: Example of circular loiter technique, landing error 500 meters

and also because it could be difficult for the energy management to decide whether to initialize another turn or not. [11]

During loiter phase a continuous computation of the residual energy (in form of altitude) is done, Equation 4.2. When this condition is met, the system triggers the terminal guidance phase. This is one of the most critical points: if the terminal guidance is switched on too early the target will be overshot, while if it is switched on too late the system will fall short of the LZ. Some margin must be taken into account: that is the reason why a $180deg$ turn is considered in the altitude margin. This is possible only if the possibility to have a longitudinal control is foreseen: decreasing γ will tackle residual altitude.

$$h_{capsule} \leq (-tan(\gamma)||\underline{x}_{LZ} - \underline{x}_{capsule}|| + \pi/\omega_{st}||v_{Z_I}||) \tag{4.2}$$

The terminal guidance phase is an homing phase aiming directly to the landing point, it is the last opportunity to do corrections in the XY-plane in order to get as close as possible to the LZ.

4.2.2 Longitudinal Guidance

The objective pursued by the longitudinal guidance is to follow a given FpA profile. The FpA profile maybe be based on the following considerations: maximizing the time of flight or tuning to have a direct landing approach thus skipping the loiter part.

In the model the FpA profile is supposed to be an input, except for the terminal guidance and flare phase. These phases are indeed the ones where FpA control can be most useful in order to reduce the landing error, Equation 4.3 shows how the γ is computed to land exactly in the right position.

$$GS = \frac{||\underline{x}_{LZ} - \underline{x}_{system}||}{h_{system}}$$
$$\gamma = -tg^{-1}\left(\frac{1}{GS}\right) \tag{4.3}$$

4.3 Control

Knowing the errors given by the Guidance, the Control outputs the control action that will act on the dynamic of the system.

From a system point of view the control is actuated pulling or releasing the suspension lines using hinges. Depending on the number of lines pulled and on their position along the canopy, the effect on the system will be different.

To model realistically the actuators rate limits and saturation were imposed. The values were chosen to simulate the hinges functioning, but, these limitations help to have a smoother variation. When the suspension lines are released it is supposed that the variation of δ is faster due to aerodynamic pressure pushing the canopy to its natural position, Table 4.2.

TABLE 4.2: Limitation on the control variables

	Rate limits [deg/sec]	Saturation [deg]
δ_a / δ_s	+5 / -90	90 / 0
μ	+5 / -90	0 / -12

4.3.1 Lateral-directional Control

The lateral-directional control is obtained by means of pulling or releasing the suspension lines connected to the trailing edges at the outer sections of the parafoil. The effect will be a canopy local curvature, that can be modeled as if there is an aileron located there.

Costello demonstrates how two dynamic modes of control are possible for parafoil: roll and skid steering. He also reports that is necessary to account for the tilt of the canopy to correctly characterize the dynamic response of the system to the control input. This is ensured by the employment of a 12 DoFs model. [22]

The control action u is equal to δ, namely the angular deflection of the aileron. In order to turn right and left, two ailerons are needed: one on the left side of the canopy and the other one on the right side. The control action will not affect directly the dynamic of the system, it will change the aerodynamic properties as shown in Equation 4.4. The values of δ_{asymm} and δ_{symm} used in Equation 4.4 are defined as Equation 4.5.

$$\begin{aligned} C_L &= C_{L_{withoutcontrol}} + C_{L_\delta}\delta_{asymm} + C_{L_{\delta_s}}\delta_{symm} \\ C_D &= C_{D_{withoutcontrol}} + C_{D_\delta}\delta_{asymm} + C_{D_{\delta_s}}\delta_{symm} \\ C_n &= C_{n_{withoutcontrol}} + C_{n_\delta}\delta_{asymm} \\ C_l &= C_{l_{withoutcontrol}} + C_{l_\delta}\delta_{asymm} \end{aligned} \tag{4.4}$$

$$\begin{aligned} \delta_{asymm} &= min(\delta_{left}, \delta_{right}) \\ \delta_{symm} &= \delta_{right} - \delta_{left} \end{aligned} \tag{4.5}$$

TABLE 4.3: Control aerodynamic derivative values

Control aerodynamic derivative	Value [1/deg]
$C_{n_{\delta a}}$	0.0115
$C_{l_{\delta a}}$	-0.0035
$C_{L_{\delta s}}$	0.0037
$C_{D_{\delta s}}$	0.0039
$C_{m_{\mu}}$	0.01846

Modeling through aerodynamic derivatives allows the model to be flexible: in this way the control technique employing air bleeds can be represented too. [20]

Two possible control laws were analyzed:

- a classical proportional law $\delta = u = K\eta$
- a sine law $\delta = u = Ksin(\eta)$

The second law is an adaptation of the law developed by Sanghyuk Park. [17] It is not possible to adopt directly his control law because he foresees the control action to act directly on the dynamic of the system as a lateral acceleration, while in this more complex model the control law acts as aileron deflection, thus it can not have the dimensions of an acceleration. S. Park law is also limited to a forward facing way-point. To overcome this limitation a saturation of η at values of $\pi/2$ and $-\pi/2$ is imposed. In this way the system will not see a control action equal to zero in case of $\eta = \pi$.

As far as $sin(\eta) = \eta$ are equal for small angles in small perturbation conditions, the two laws will perform approximately in the same way. Therefore the difference is quite visible for large angular displacements coupled with small turning radius, as shown in Figure 4.8. The sine follows more accurately the wanted path than the proportional one.

Therefore the sine law was selected for the lateral-directional control.

4.3.2 Longitudinal Control

Literature reports to halve the landing error if there is the possibility to exploit longitudinal control. [29] This was observed also in the simulations performed, even if their number is too small to be considered a real trend, an example is given in Figure 4.10.

The longitudinal control can be achieved in two ways: firstly by means of symmetric ailerons deflection and secondly by rigging control. The first control strategy depends on the aerodynamic of the parafoil. Indeed if $C_{D_{\delta_s}}$ and $C_{L_{\delta_s}}$ have the same modulus and sign, the increment of lift and drag will be similar in case of ailerons deflection. It means that the lift-to-drag ratio will be approximately unaffected and the FpA too, their dependency is expressed in Equation 4.6.

$$\gamma = -\frac{1}{tan^{-1}(\frac{L}{D})} \tag{4.6}$$

Rigging control is a viable way for every kind of parafoil, independently on the aerodynamic. It consists in a rigid rotation of the canopy front part pulling or releasing all the lines attached to the leading edge of the parafoil, Figure 4.11. As Lingard states in his work [13], the rigging angle affects the dynamic of the parafoil in multiple ways.

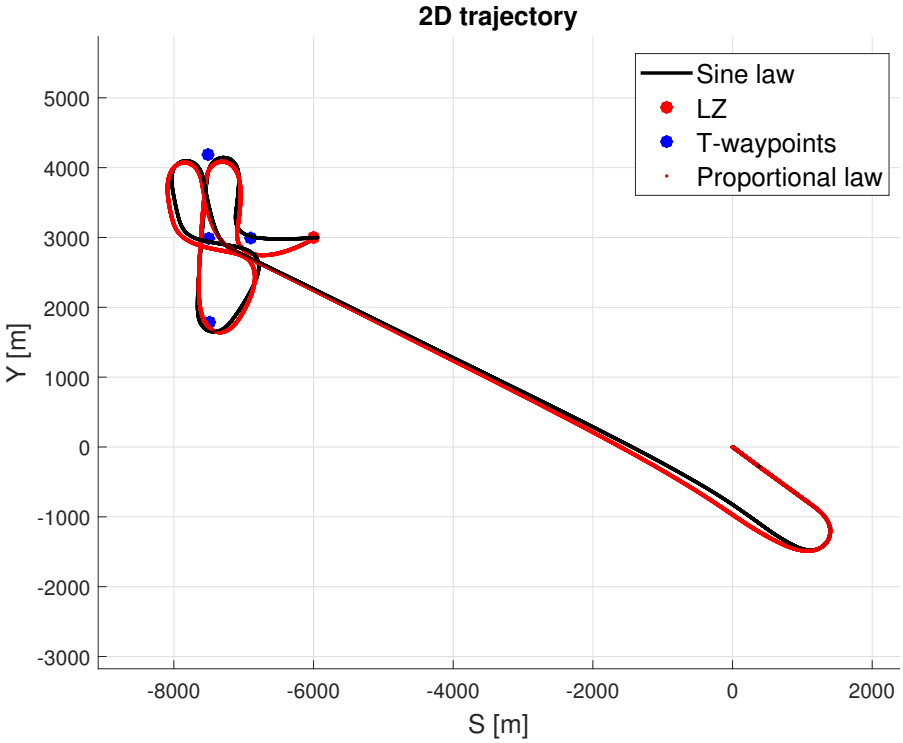

FIGURE 4.8: Different control laws 3D trajectories

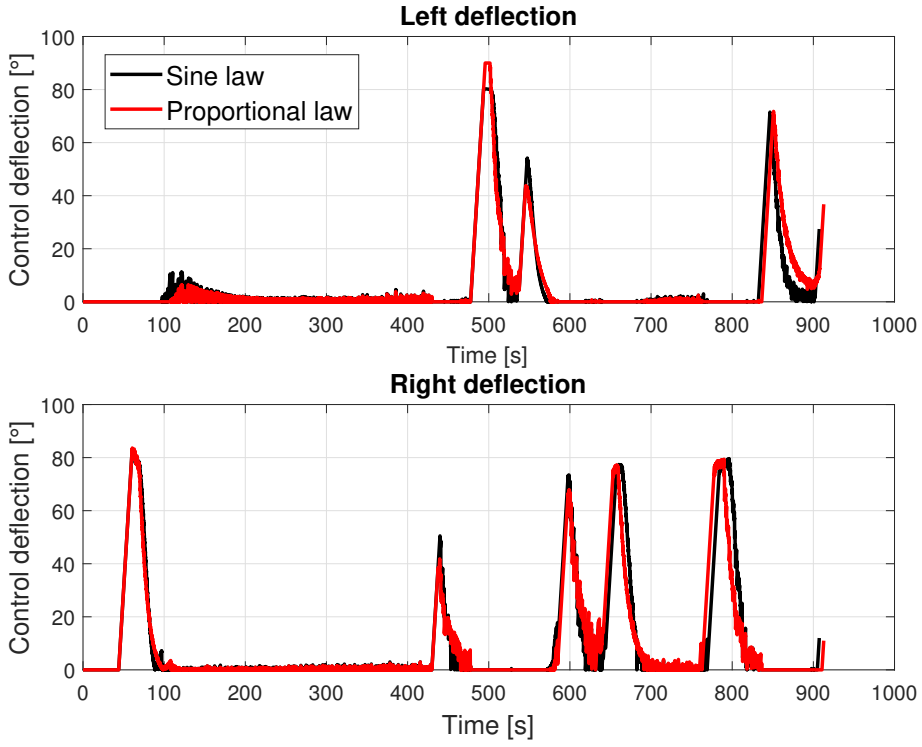

FIGURE 4.9: Different control laws ailerons deflection

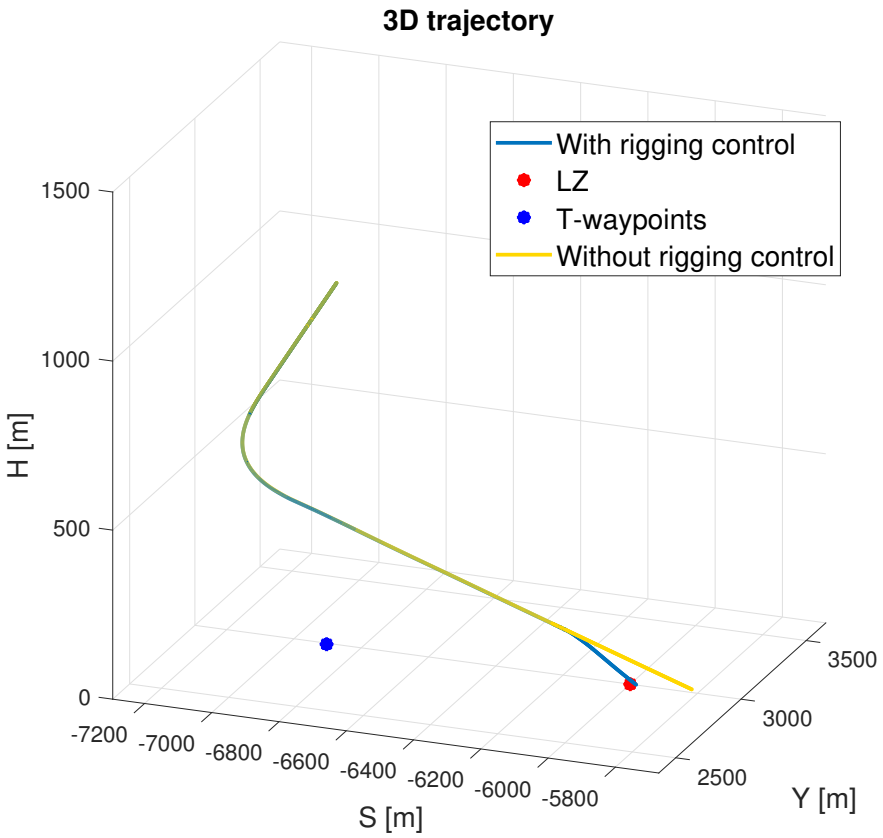

FIGURE 4.10: Landing accuracy with and without longitudinal control

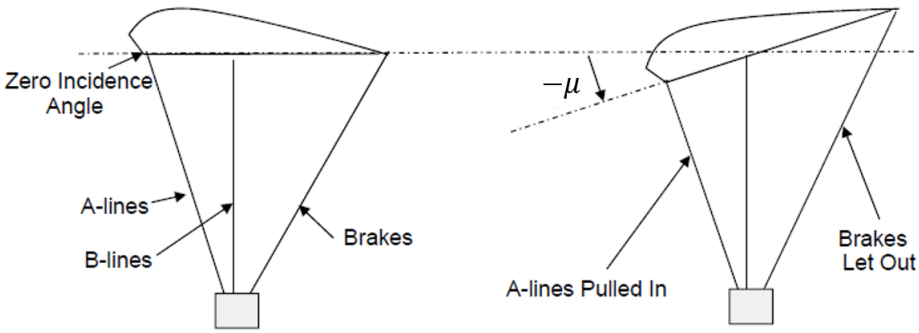

FIGURE 4.11: Rigging control actuation [27]

There is relation between μ (rigging angle) and C_m, as shown in Figure 4.12.

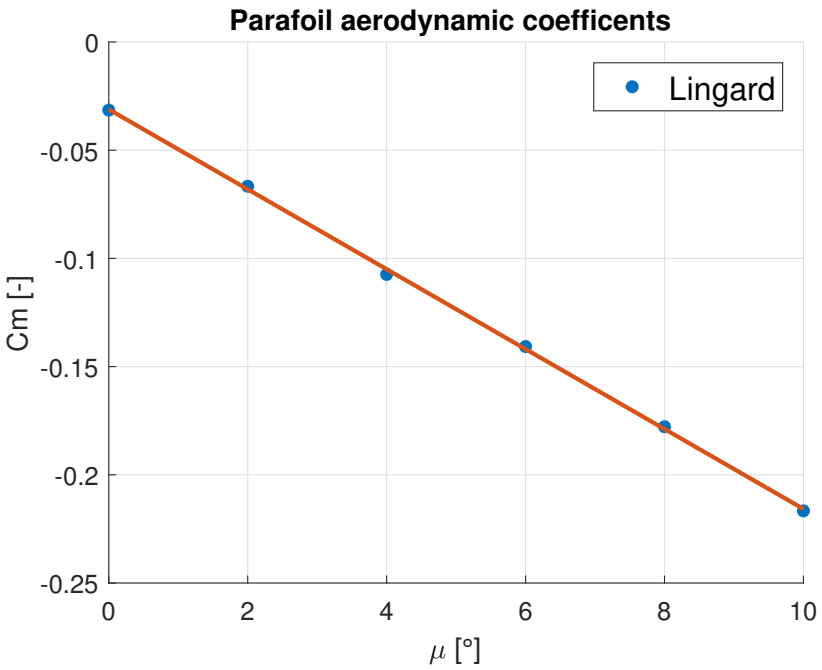

FIGURE 4.12: $C_{m/\mu}$ slope

In this way a linearized additional term can be added to the usual formulation of the longitudinal moment coefficient. The value of $C_{m/\mu}$ used in Equation 4.7 can be retrieved from the slope of the curve in Figure 4.12: $C_{m/\mu} = 0.018461/deg$. The sign is inverted with respect to the one of the Figure 4.12 because Lingard considers the rigging angle to be positive, while in this work is considered negative to be consistent with the right-hand rule and the reference system taken, Section 2.

$$C_m = C_{m_0} + C_{m/\alpha}\alpha + C_{m/\mu}\mu \tag{4.7}$$

The other effect of the rigging angle on the dynamic is its presence in the rotation matrix from wind to body axes, as shown in Equation 2.32. In the same way the incidence angle is modeled for an airplane wing.

As shown in Reference [13] the interaction between rigging angle and the dynamic of the system is more complex than the actual model presented in the present work. There is a cross interaction between symmetric ailerons deflection and rigging angle with C_m. μ also affects the C_L and C_D dependence from α. These effects will be implemented once the design of the SpaceRider parafoil will be more detailed.

The effects considered are sufficient to study the feasibility of the non-linear longitudinal control law analyzed in the present work, Equation 4.8.

$$\begin{aligned} \dot{\mu} &= K_\mu(\gamma_{desired} - \gamma)^2 sign(\gamma_{desired} - \gamma) + \dot{\theta} \\ \mu_k &= \mu_{k-1} + \dot{\mu}\Delta t \end{aligned} \tag{4.8}$$

To be implemented in the model, Equation 4.8 must be coupled with a user-specified initial condition. In simulations the μ_0 considered is always equal to 0 deg.

As said at the beginning of this Section the other possibility to actively control the FpA is by means of symmetric aileron deflection. This possibility is also analyzed and the control law presented in Equation 4.9 is used.

$$u = \dot{\delta} = K_{\delta_s}(\gamma - \gamma_{des}) \tag{4.9}$$

How δ_s is going to affect the dynamic of the system it is presented in Equation 4.4 with the values reported in Table 4.3. The Lyapunov stability of the symmetric brake deflection is shown in Section A.

It worths noting that both the longitudinal control strategies can only decrease the γ value, not increase it, because suspension lines can only be pulled or released to their natural conditions, not pushed to a controlled value.

Lyapunov stability demonstration of rigging angle control

To ensure the control Lyapunov stability the following conditions must be met:

- $V(x) > 0$ for every x different from the x_{eq}
- $V(x_{eq}) = 0$
- $\dot{V}(x) < 0$ for every x

Equation 4.10 can be selected as Lyapunov function. This is going to respect the first two conditions considering the way it was written.

$$V(x) = \frac{1}{2}(\gamma_{desired} - \gamma)^2 \tag{4.10}$$

Now, taking the derivative, Equation 4.11 is obtained.

$$\dot{V}(x) = (\gamma_{desired} - \gamma)(\dot{\gamma}_{desired} - \dot{\gamma}) \tag{4.11}$$

It can be supposed, without loosing of generality, that the $\gamma_{desired}$ profile is going to vary slower than the dynamic of the system itself (it could be a constant value or slowly varying). In this way the derivative of $\gamma_{desired}$ is zero.

$$\dot{V}(x) = -\dot{\gamma}(\gamma_{desired} - \gamma) \tag{4.12}$$

By definition of the angles the Equation 4.13 holds.

$$\gamma + \theta = \mu + \alpha \tag{4.13}$$

Thus γ can be rewritten as Equation 4.14.

$$\gamma = \mu + \alpha - \theta \tag{4.14}$$

Substituting in the derivative, the Equation 4.15 is obtained.

$$\dot{V}(x) = -(\dot{\mu} + \dot{\alpha} - \dot{\theta})(\gamma_{desired} - \gamma) \tag{4.15}$$

Focusing on $\dot{\alpha}$ and using the properties of the partial derivatives Equation 4.16 can be written.

$$\dot{\alpha} = \frac{\delta\alpha}{\delta C_L}\frac{\delta C_L}{\delta t} \tag{4.16}$$

The first term is equal to the reciprocal of $C_{L_{/\alpha}}$ and for a parafoil (as for a wing) is positive. This imply obviously that control must operate only when the aerodynamic forces can be considered linearly dependent on α. It is not a limitation because

during the inflation (when linear aerodynamic coefficients assumption is not true) the control is deactivated: to avoid unnecessary overload of the control.

The other term of Equation 4.16 is the time derivative of the lift coefficient. The lift coefficient can be directly related to the lift by the well-known Equation 4.17.

$$C_L = \frac{2L}{\rho V^2 S} \tag{4.17}$$

$$\frac{\delta C_L}{\delta t} = \frac{2L}{\rho S}\frac{\delta}{\delta t}(\frac{1}{V^2}) \tag{4.18}$$

The velocity is not going to change in its modulus, only in its direction, so the Equation 4.18 is equal to zero. The variation of ρ due to density change in the atmosphere model is very slow with respect to the dynamic of the system, this is the reason why they have not been considered in the differentiation.

So Equation 4.15 becomes Equation 4.19.

$$\dot{V}(x) = -(\dot{\mu} - \dot{\theta})(\gamma_{desired} - \gamma) \tag{4.19}$$

Knowing Equation 4.8, the term $\dot{\mu}$ can be substituted with the control law, in this way Equation 4.20 is obtained.

$$\dot{V}(x) = -K_\mu(\gamma_{desired} - \gamma)^2 sign(\gamma_{desired} - \gamma)(\gamma_{desired} - \gamma) \tag{4.20}$$

As it can be noted the Equation 4.20 respects the last condition for the Lyapunov stability: it is always negative if K_μ is more than 0.

Chapter 5

Simulation results

In Chapter 5 the functionalities and the real application of the model are shown. The model can be used to size the aerodynamic decelerator system (parachute and parafoil) and also to test and characterize GNC algorithms. Figure 5.1 shows the overall structure of Chapter 5.

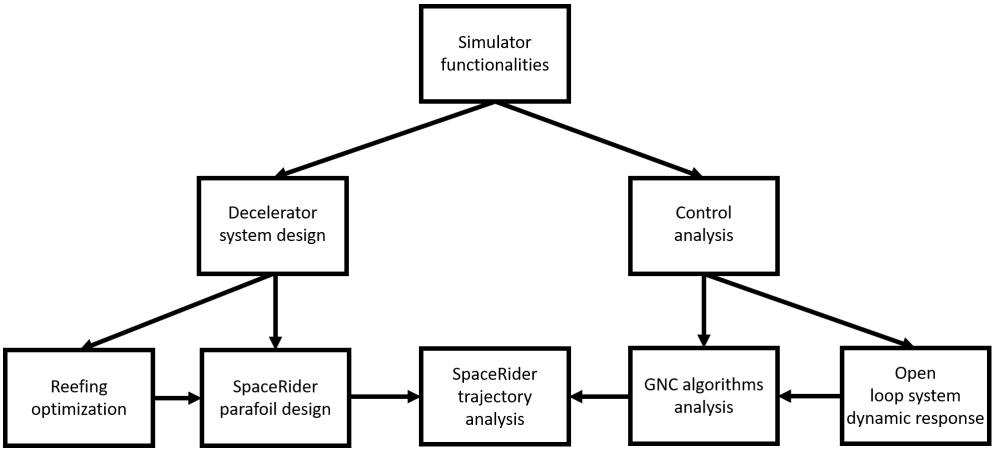

FIGURE 5.1: Chapter 5 structure and logic

5.1 System design

In the present Section the model is used to size the parafoil system. The main design requirements derive from maximum deceleration at the opening (i.e. it do not exceed 3g's to avoid damage to the payload) or flight velocity in steady-state conditions. The main variables are the canopy surface, affecting both requirements, and the reefing technique, affecting only opening loads.

5.1.1 Reefing optimization

The reefing technique is based on two parameters: the surface of the reefed stage (expressed in % with respect to the nominal area) and the time delay between the stage inflation and the initialization of the following stage.

As introduced in Section 2.1.3, the reefing strategy in parafoil has not a linear correlation with experienced inflation loads. The non-linearity of the phenomenon allows to perform an optimization of the reefing parameters to reduce the loads at inflation. Due to software limitation the optimization employed in the present work is a gird-search type: different combinations of time-delays and reefing percentages are simulated and mapped. It is then possible to retrieve the optimal configuration from graphs.

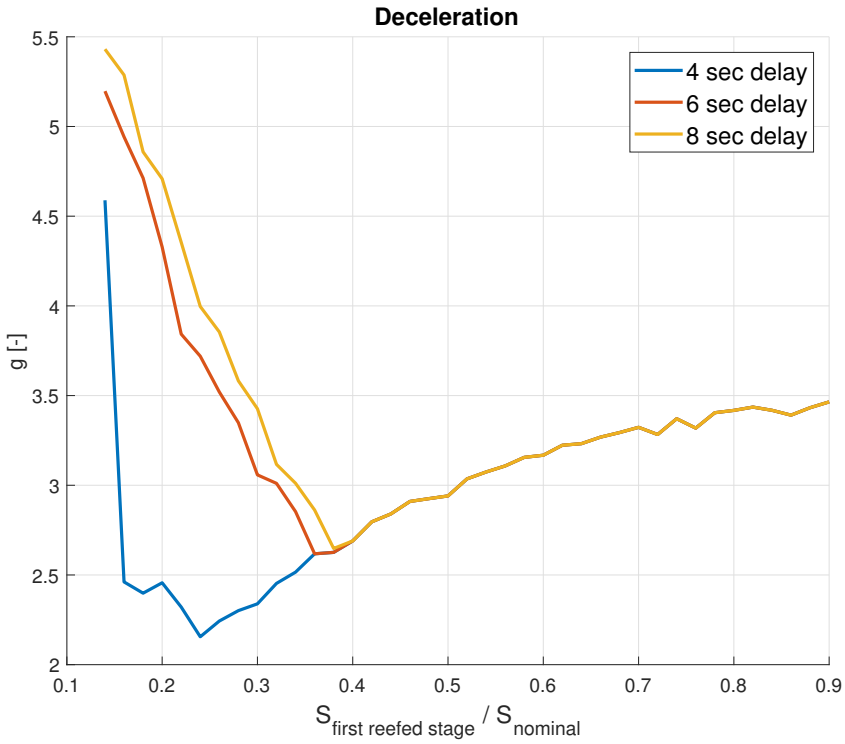

FIGURE 5.2: Gird-search first stage reefing optimization

In Figure 5.2 the results of the optimization process are reported, referring to the following system configuration: SpaceRider (as payload), parafoil (with canopy surface $250m^2$ and aerodynamic properties of the X-38 parafoil, Section 2.1.4). As shown in Figure 5.2 the optimal solution is found at a reefing percentage of 25% with a time-delay of 4 seconds between first stage inflation and full inflation. The time-delays analyzed are only 4,6 and 8 seconds because the reefing cutters are standard pyrotechnics hardware, so they can not be customized from application to application.

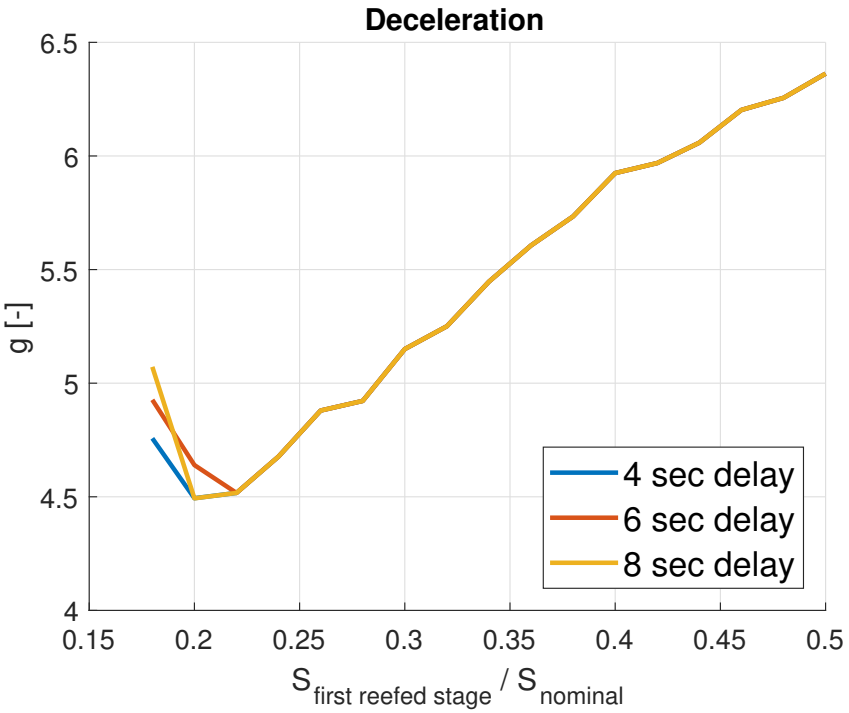

FIGURE 5.3: Gird-search first stage reefing optimization at different deployment conditions

As shown in Figure 5.3 the time-delay effect changes depending on the deployment conditions (velocity and altitude), but in any case a time-delay of 4 seconds remains the lower boundary near the minimum.

Imposing a time-delay of 4 seconds (the best solution for SpaceRider application) and knowing that a design requirement of maximum 3 g's must be met, an operational curve is drawn, Figure 5.4. In Figure 5.4 the y-axis is the dynamic pressure defining a combination of altitudes and velocities, while the x-axis is the reefing percentage. In order to deploy the parafoil without exceeding design requirements the configuration must stay under the operational curve, choosing a combination of reefing percentage, altitude and speed.

To check the validity of this procedure, the grid-search optimization is performed also for the X-38 first stage reefing. As shown in Figure 5.5 the reefing strategy employed by NASA and Pioneer for the first stage is the optimal one: a reefing percentage around 33% and time-delay of 6 seconds. Thus the grid-search technique developed in the frame of this work is a viable procedure to find the actual optimal reefing strategy.

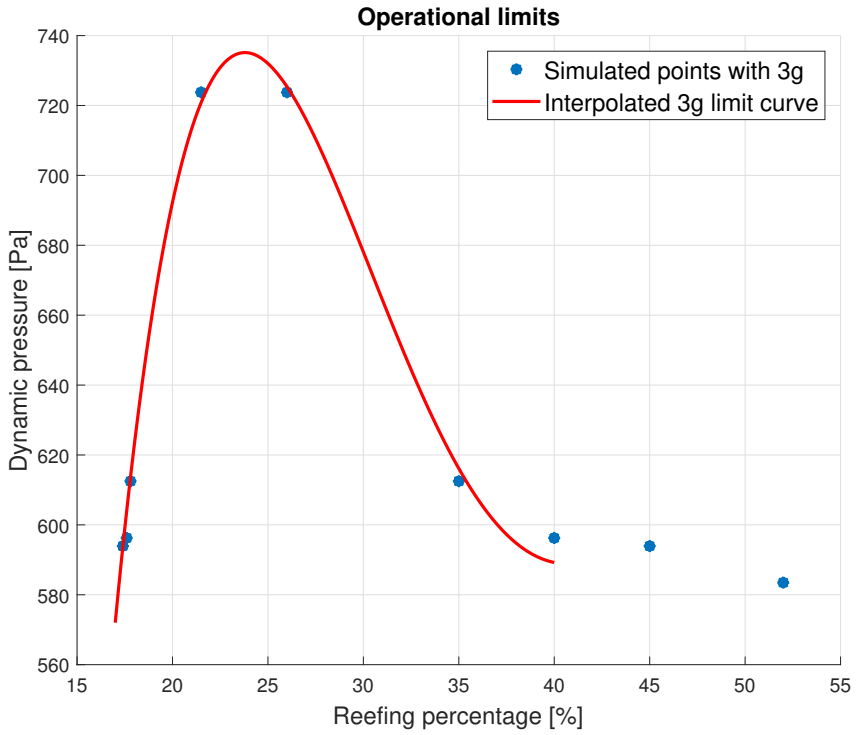

FIGURE 5.4: Safe-to-deploy curve, below the red curve parafoil can be deployed

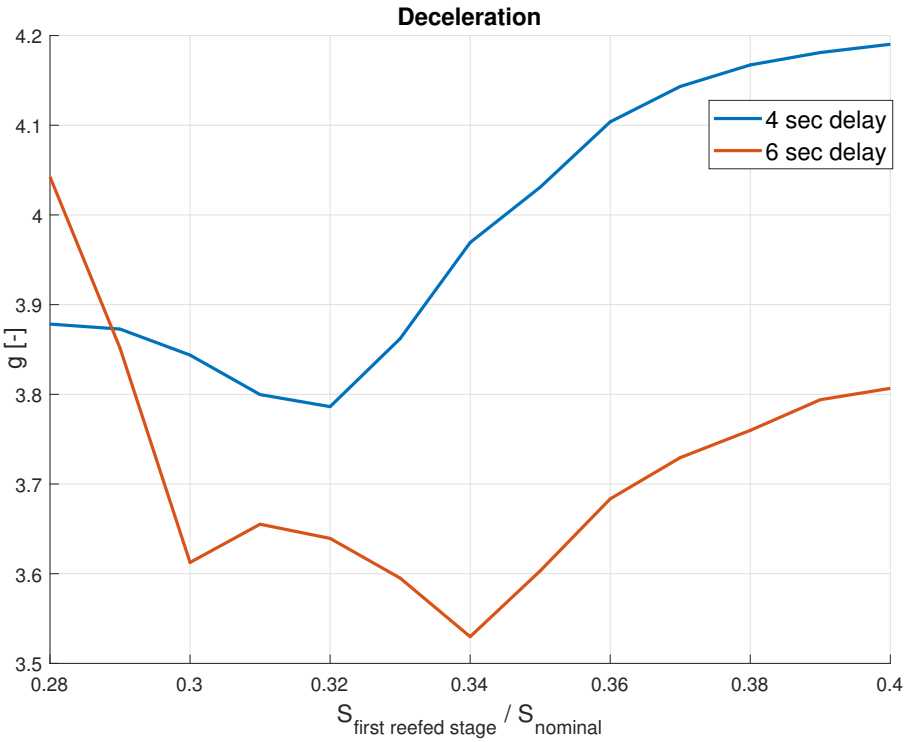

FIGURE 5.5: X-38 first stage reefing optimization

5.1.2 SpaceRider aerodynamic decelerator system design

The parafoil is an element of the wider aerodynamic decelerator system of SpaceRider. It could be possible that the parafoil design requirements come from a terminal velocity constraint. In this way the inflated surface area of the canopy would be fixed (once the aerodynamic properties of the parafoil are known) and, as shown in Section 5.1.1, the reduction of maximum decelerations obtainable with reefing strategy is limited. So it could be necessary to design the previous ballistic parachutes stages in order to have limited loads at the parafoil opening.

A tool has been created to find a combination of ballistic parachute and opening logic through an iterative approach with an optimization-like logic to respect to the maximum load design requirements.

The parameters that can be changed are:

- First stage parachute area
- Second stage parachute area
- Opening altitude of the second stage

The inputs to be given are:

- Initial conditions before first stage deployment
- Parafoil opening altitude (due to cross-range considerations)
- Parafoil canopy surface (the standard SpaceRider parafoil with $250m^2$ canopy is used)
- Maximum load that can be experienced (3gs)

The changing parameter logic of the tool is the following: if the parafoil stage experienced loads are above the design limit the second stage parachute area is increased. In case the second stage loads are higher than the allowable value, the area of the second stage parachute is decreased, the area of the first parachute is increased and the opening altitude is increased too. The first stage instead is exploited not only to maintain the opening loads below the design requirement (if too high the area is decreased) but also to damp the loads excess from the other stages: if the load of the first stage is lower than a certain threshold, its area is increased to avoid overloading the other stages.

TABLE 5.1: Parameters value found that satisfies the design requirements

Parameter	First stage diameter	Second stage diameter	Second stage opening h
Value [m]	4.1	8	8500

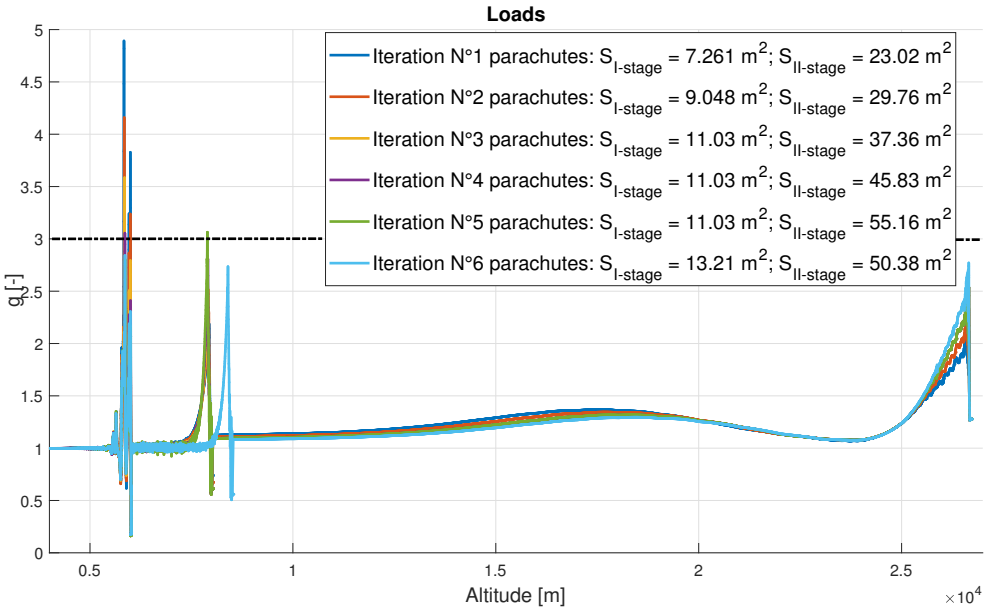

FIGURE 5.6: Loads behavior with the optimization iteration

The results obtained, using this iterative approach, are shown in Figure 5.6, convergence is obtained after 6 iterations. The found values of parachute areas and of the second stage opening altitude are reported in Table 5.1.

5.2 GNC analysis

In the following Section an analysis of the GNC algorithm will be performed. The results presented are always affected by both uncertainties in the states estimation, Section 4.1, and by wind action.

The wind is not presented in the modeling section because it was an already build-in suite in the model. The wind profile is made up of an altitude linear-dependent profile plus a gust modeled as a normal distribution, as shown in Figure 5.7. The wind is stronger at lower altitudes, this is counter intuitive but it is considered even a worst case scenario so it is acceptable.

The wind is supposed to be read on board in real-time by the system. It is however affected by the errors mentioned in Section 4.1.

5.2.1 Dynamic analysis of the system response to control action

To have an idea of how the system behaves when control action is activated, simulations are performed for each control strategy. It is an open loop control cycle aimed to check that the behavior of the system is physically feasible.

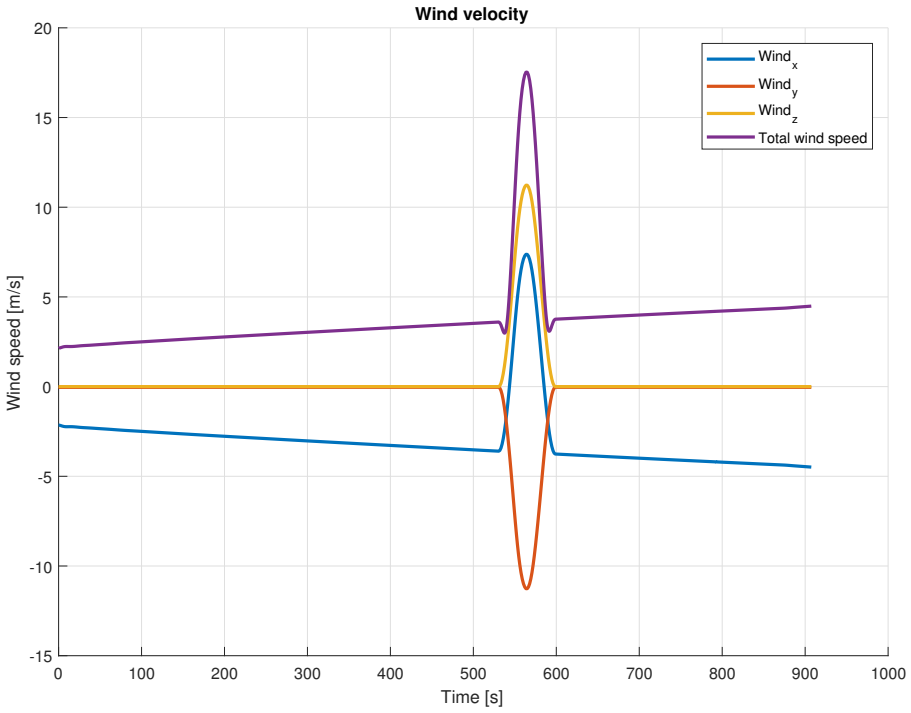

FIGURE 5.7: Built-in wind profile

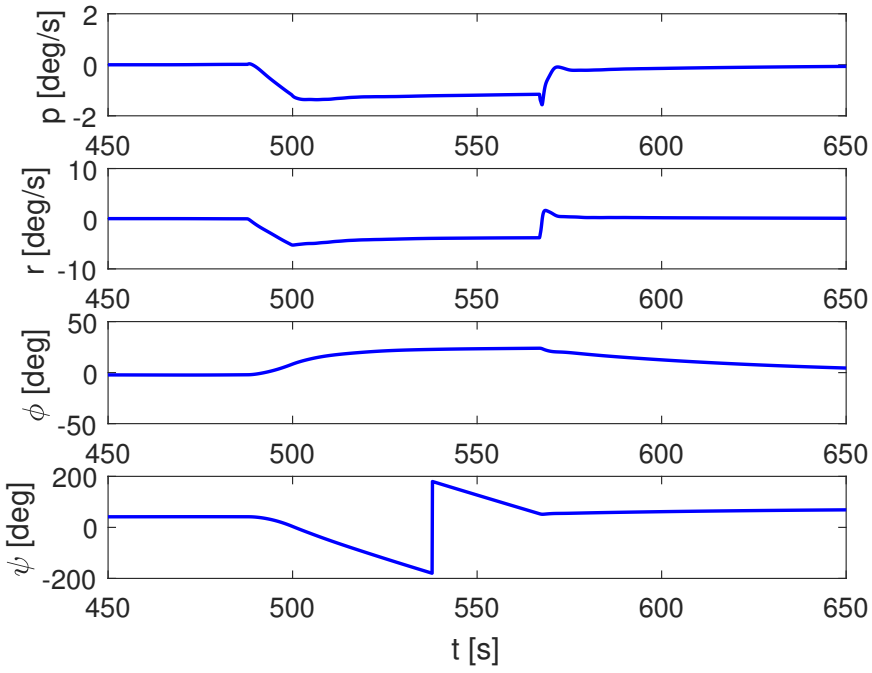

FIGURE 5.8: System response to ailerons asymmetric deflection reported in Figure 5.9

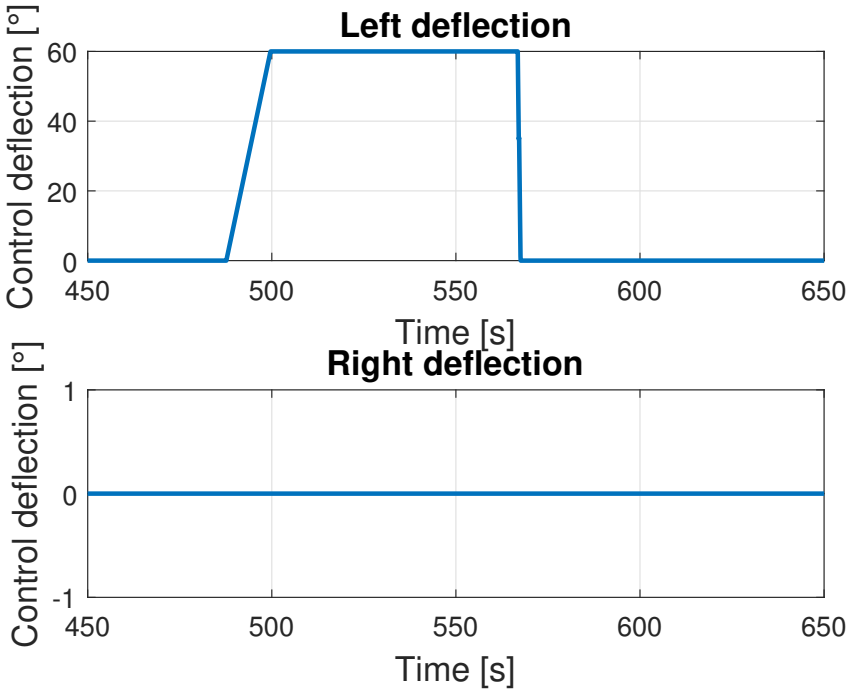

FIGURE 5.9: Asymmetric deflection

As shown in Figure 5.8 the system turns left when undergoes to a left aileron deflection. It shows how the system is turning with a skid steering mode. The trajectory is affected by asymmetric deflection as shown in Figure 5.10.

The system response is studied also in case of longitudinal control action in the case of rigging angle change, Figures from 5.11 to 5.12.

As shown in Figure 5.12 the system response is consistent to what is usually experienced: lowering the leading edge of the canopy leads the system to lower its FpA, to have a more pitch down attitude and consequently to gain speed.

5.2.2 Longitudinal control analysis

The longitudinal control is very useful in the last stages of the flight to reduce the landing error. The non-linear rigging control law presented in Section 4.3.2 is analyzed.

As shown in Figure 5.13 the non-linear control is more effective of the classical linear strategy. The proportional law continues to oscillate around the desired condition, a more complex controller is needed (with also a integrative and derivative part). In any case a PID controller is not well suited as a non-linear controller because it does not take into account the non-linear dynamic of the system.

Even if at steady state the term $\dot{\theta}$ is close to zero, its importance can be seen in Figure 5.14. When the system encounters a gust, the presence of the $\dot{\theta}$ allows to damp quickly the oscillations caused by the gust itself, while its absence leads the system to a divergent oscillatory motion.

As said in Section 2.1.4 a linear parafoil aerodynamic model was also implemented. This was useful to check the flexibility of the longitudinal control law guaranteed by its Lyapunov stability. Figure 5.16 shows how the longitudinal control worked well even when applied to different parafoils.

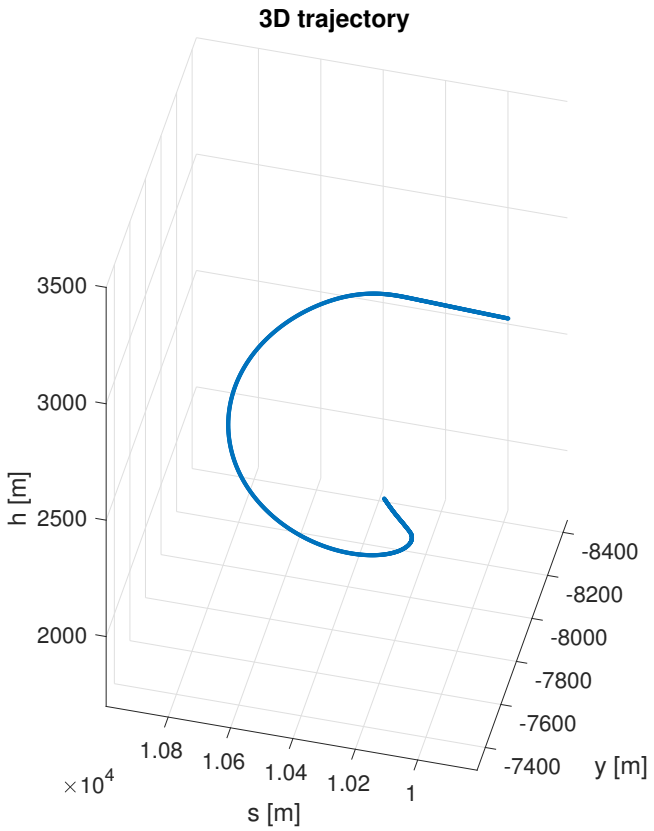

FIGURE 5.10: Trajectory change due to ailerons asymmetric deflection reported in Figure 5.9

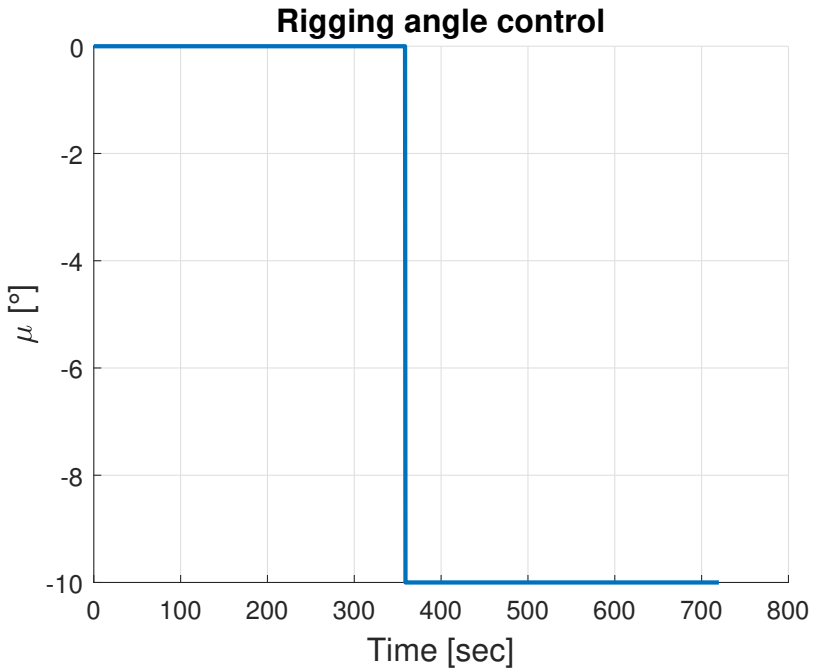

FIGURE 5.11: Rigging angle change

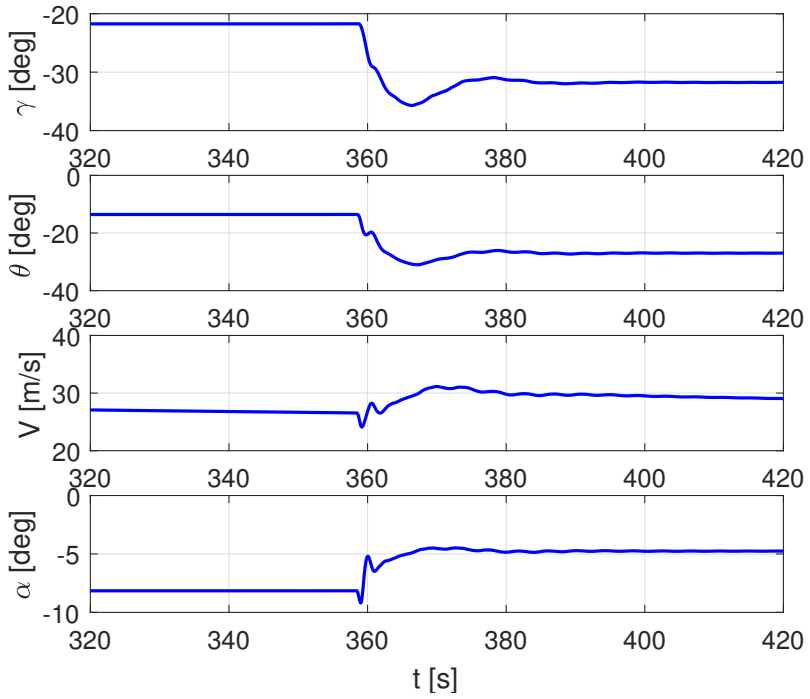

FIGURE 5.12: System response to rigging angle change reported in Figure 5.11

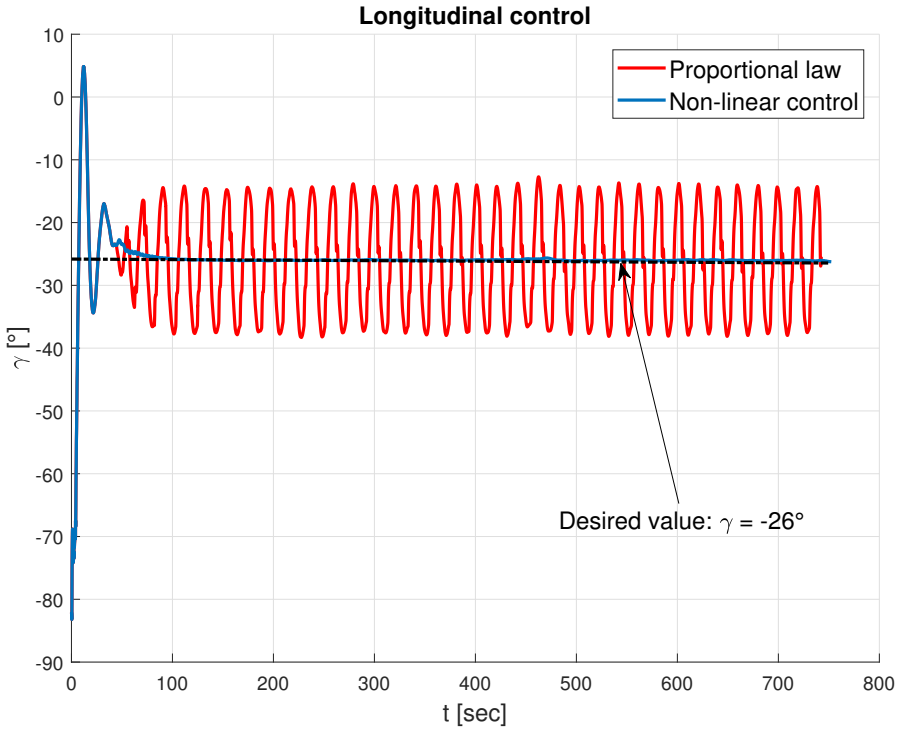

FIGURE 5.13: Linear and non-linear longitudinal control law comparison

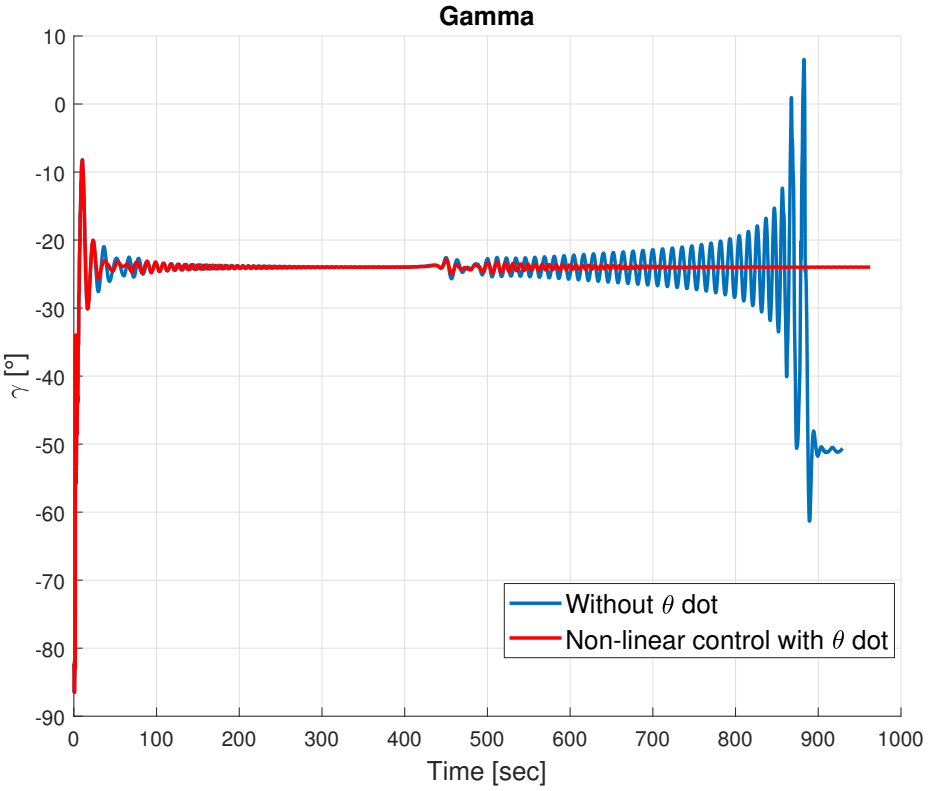

FIGURE 5.14: $\dot{\theta}$ effect on gust response

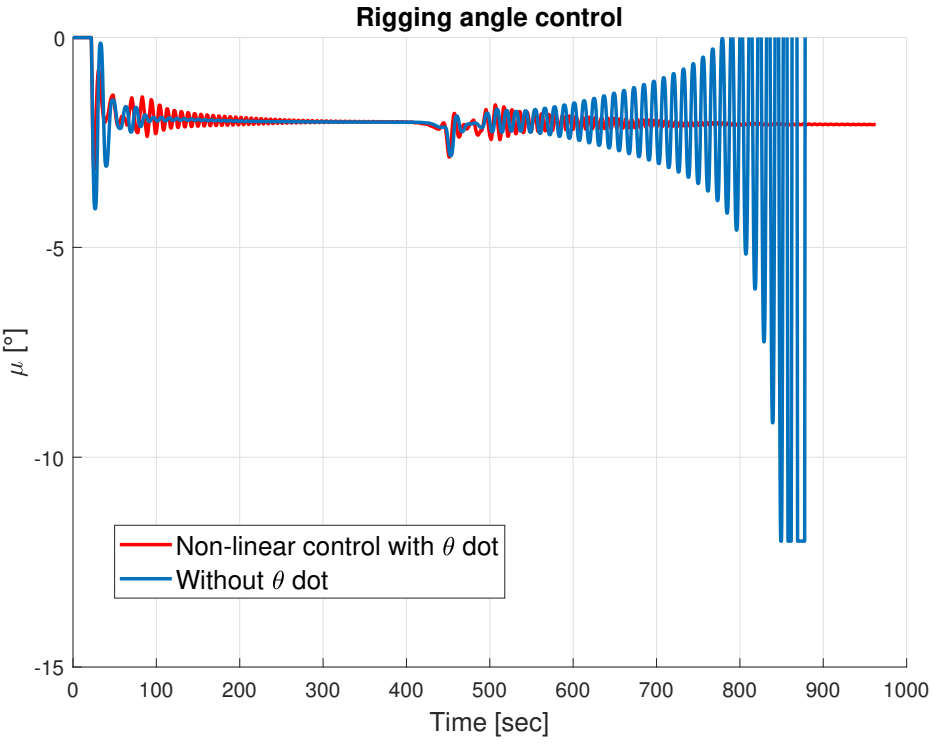

FIGURE 5.15: Control action with respect to the case in Figure 5.14

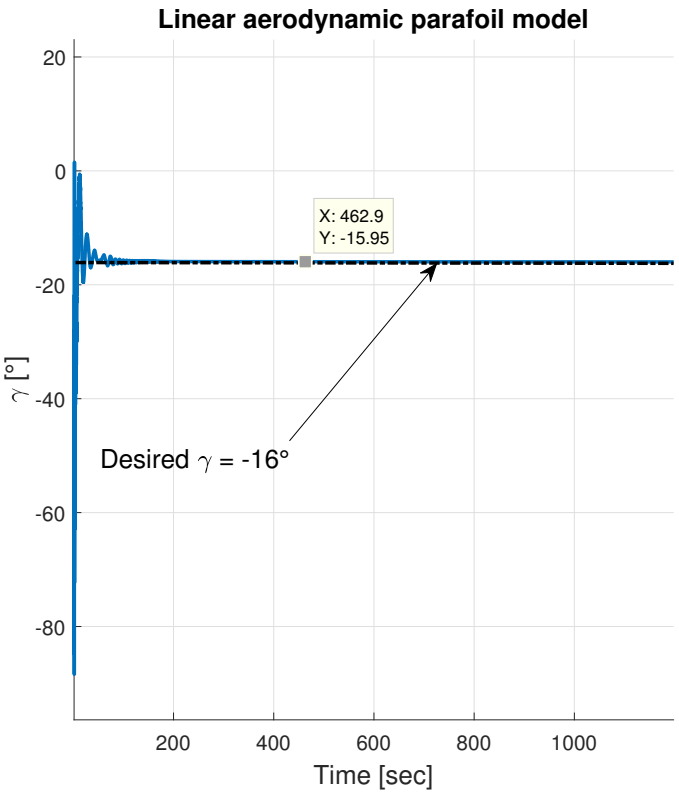

FIGURE 5.16: Rigging control linear parafoil aerodynamic model

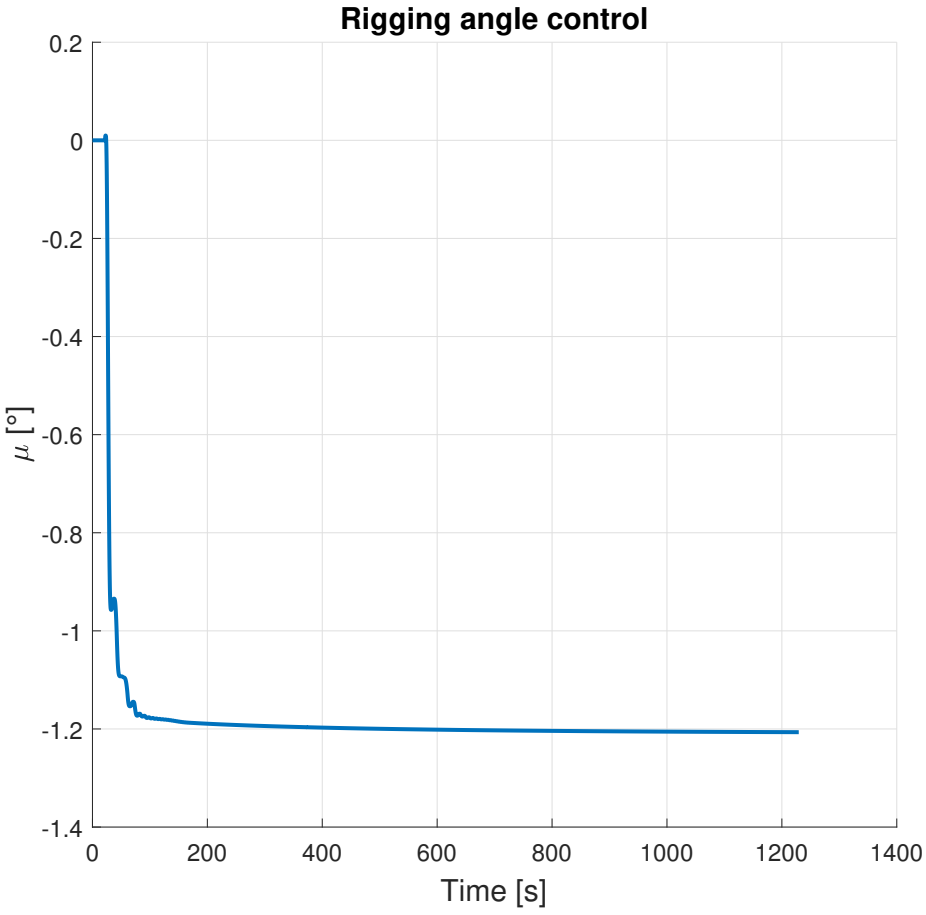

FIGURE 5.17: Rigging values related to simulation showed in Figure 5.16

In the control law showed in Equation 4.8 the term K_μ is present, it is the gain of the control law and it can be an arbitrary value more than zero. An example on how this term is going to affect the dynamic of the system is shown in Figure 5.18.

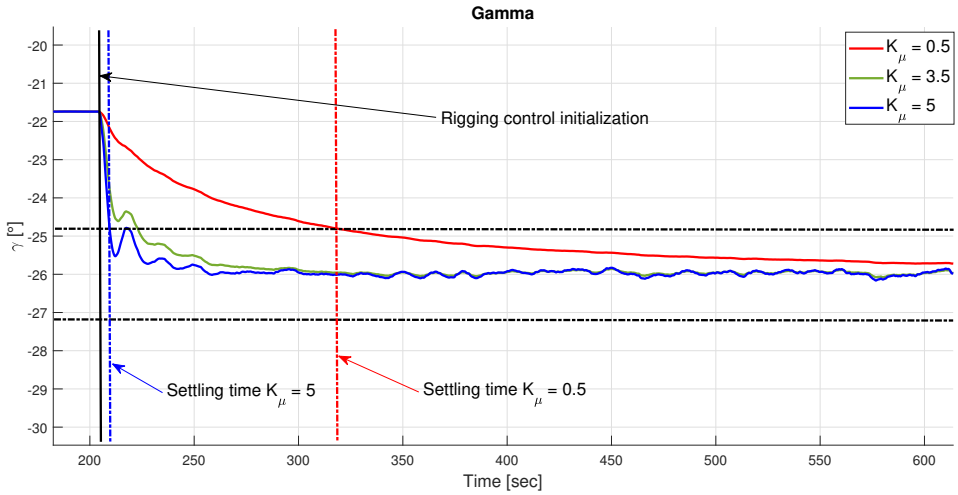

FIGURE 5.18: Different gains effect

Control laws effectiveness can be evaluated mainly looking at two parameters: settling time and amplitude oscillations before the desired conditions are reached. Having this in mind an evaluation of the control law can be performed with respect to different gains.

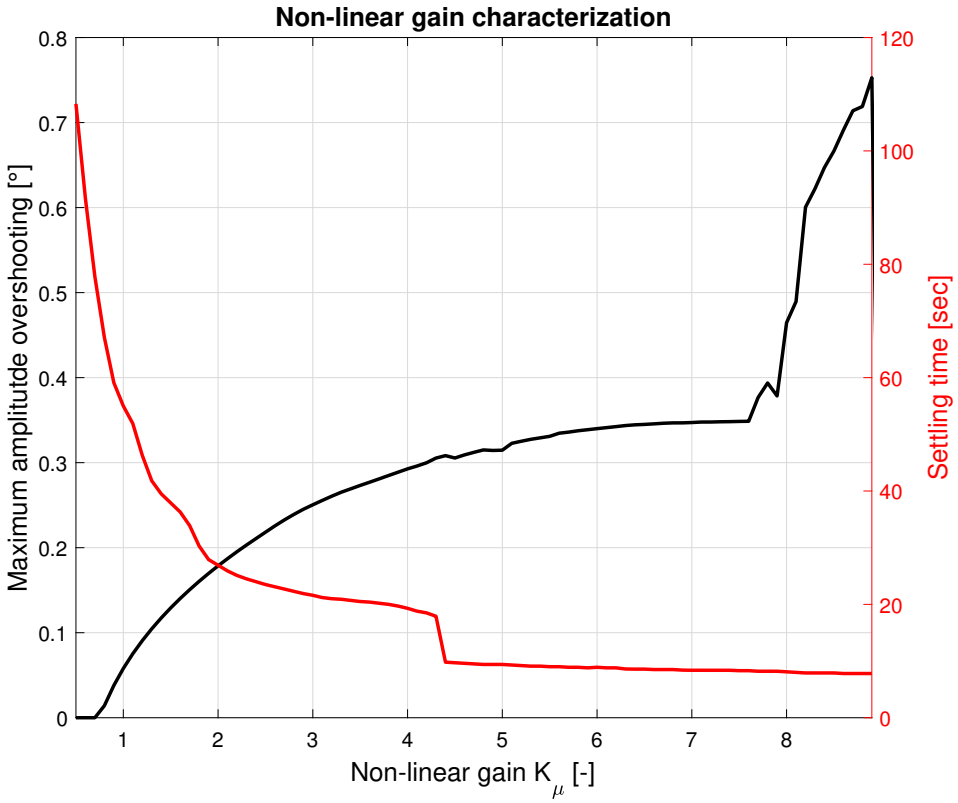

FIGURE 5.19: K_μ analysis

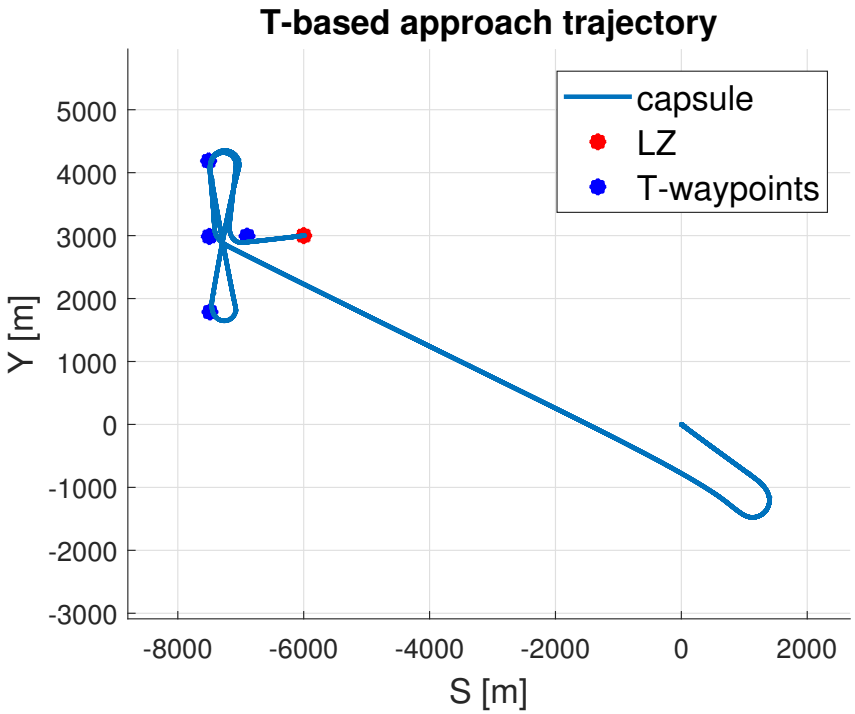

FIGURE 5.20: 2D T-based trajectory

As shown in Figure 5.19 the optimal gain K_μ value could be 5. In this way it maintains the γ oscillations below 5% of error and it has also a settling time below 10 seconds.

5.2.3 Adaptive control

Figures from 5.20 to 5.22 show the results obtained applying an adaptive control guidance with a T-based approach.

The landing error of the reported simulation is 22 meters. The error is very small, considering that it is a large canopy with 200 meter turning radius, thanks also to the glide slope control in the terminal phase of the flight. Figures from 5.23 to 5.24 show how the system realizes to be too high to land at the desired point, thus it commands a rigging angle change.

An additional reduction of the glide slope could not be possible only by rigging angle control means because it reached saturation, Figure 5.24. Removing the saturation, it will lead to a mathematically feasible solution without physical meaning: the canopy would collapse.

A combined action of δ_s and μ could be exploited instead: the use of the rigging angle to control the FpA while the ailerons symmetric deflection is used to control the velocity profile.

CEP computation

To have an idea of the accuracy of the employed GNC algorithm an estimation of the CEP is needed. Circular error probability (CEP) is defined as the radius of the circle where it is expected a determined probability of the population will land. In order to do this estimation some little Monte Carlo simulations are to be performed. Once enough simulations are performed the CEP can be compute with Equations from 5.1 to 5.3. Equation 5.3 can be used only in case $\overline{x}_{LND} \approx \overline{y}_{LND} \approx 0$ and $\sigma_y \approx \sigma_x$, that

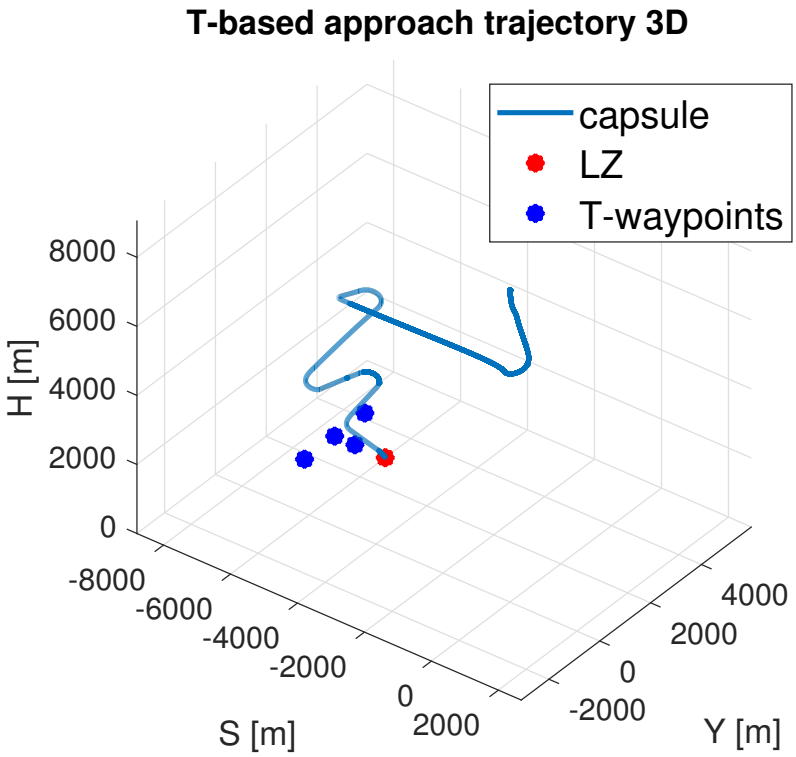

FIGURE 5.21: 3D T-based trajectory

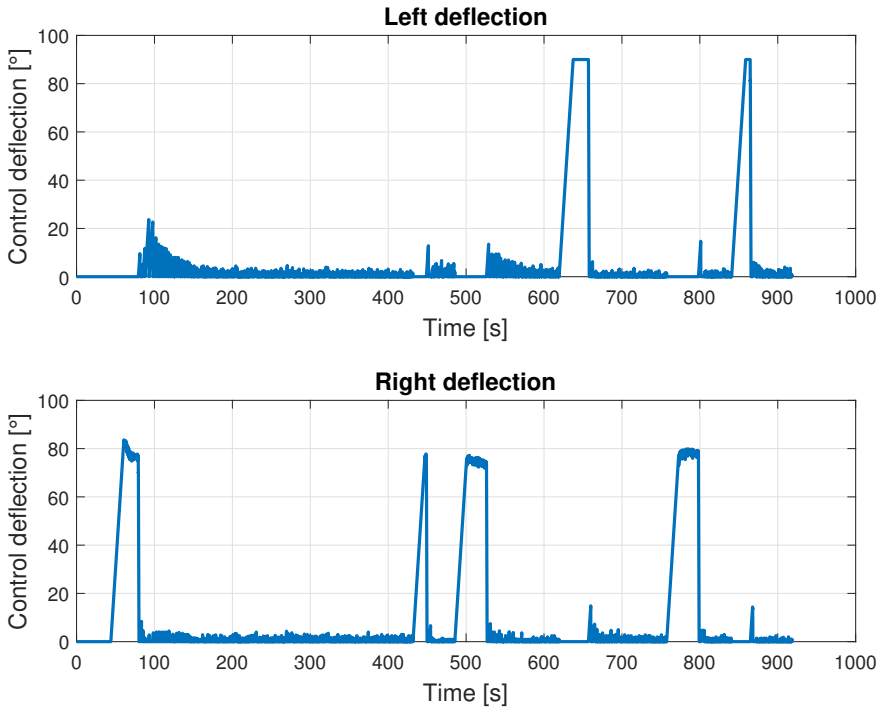

FIGURE 5.22: Ailerons deflection related to trajectory in Figure 5.20

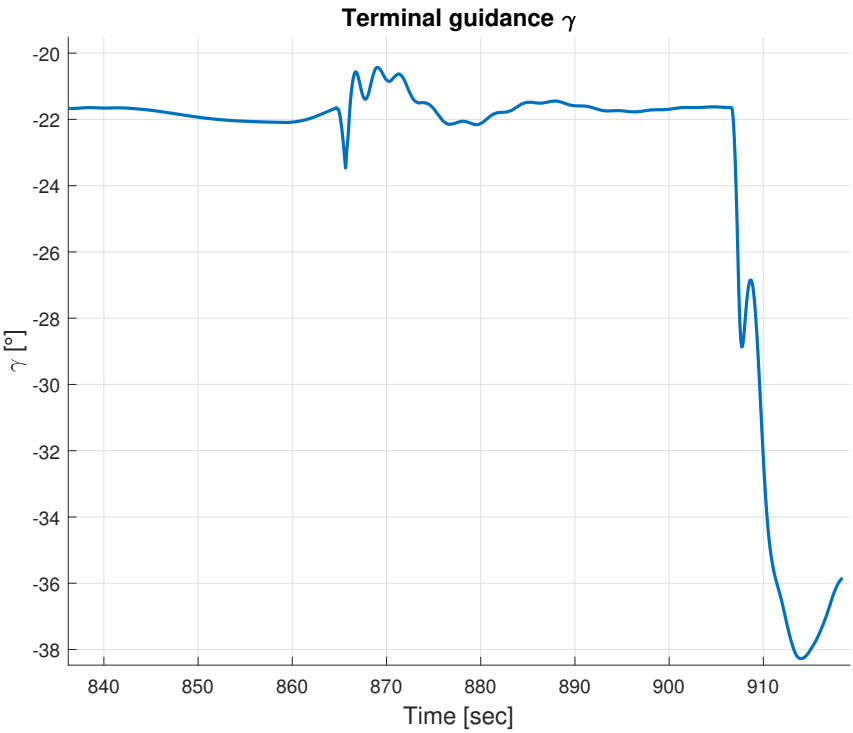

FIGURE 5.23: FpA profile of the lasts moment before landing

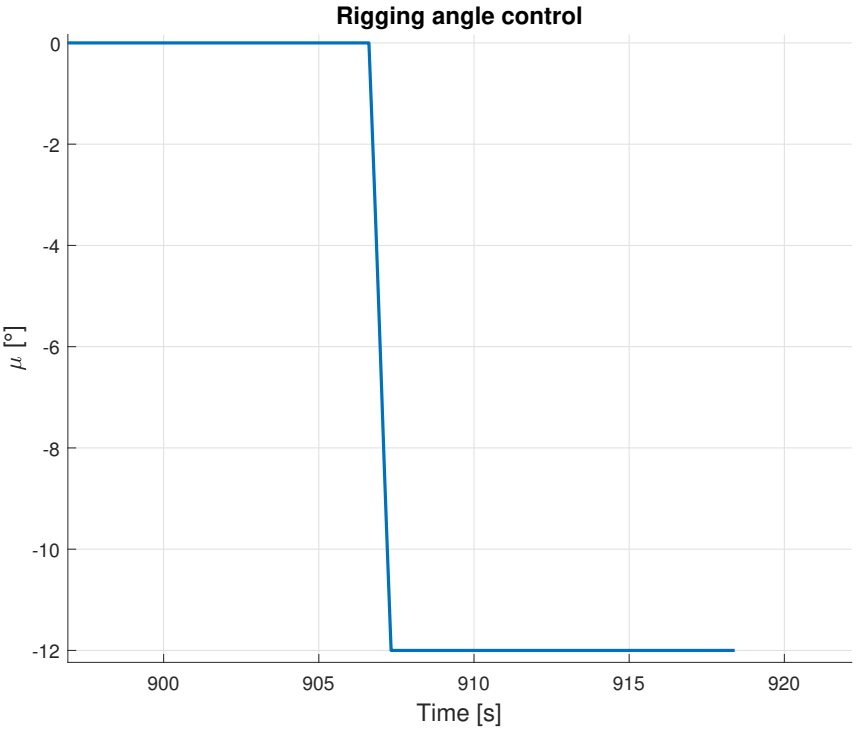

FIGURE 5.24: Rigging angle control, saturation reached

means a no bias and circular probability distribution is observed. So the probability distribution can be assumed to be a Rayleigh one. The term $P_{\%}$ in Equation 5.3 is the level of desired confidence for the CEP computation: in case the CEP must include 50% of the population $P_{\%}$ will be equal to 0.5, in case of 90% is searched $P_{\%}$ will be equal to 0.9.

$$\begin{aligned} \overline{x}_{LND} &= \frac{\sum_{i=1}^{n} x_i}{n} \\ \overline{y}_{LND} &= \frac{\sum_{i=1}^{n} y_i}{n} \end{aligned} \tag{5.1}$$

$$\begin{aligned} \sigma_x^2 &= \frac{(\sum_{i=1}^{n}(x_i - \overline{x}_{LND}))^2}{n} \\ \sigma_y^2 &= \frac{(\sum_{i=1}^{n}(y_i - \overline{y}_{LND}))^2}{n} \end{aligned} \tag{5.2}$$

$$\begin{aligned} CEP_x &= \sqrt{2 \quad ln\left(\frac{1}{1 - P_{\%}}\right)} \quad \sigma_x \\ CEP_y &= \sqrt{2 \quad ln\left(\frac{1}{1 - P_{\%}}\right)} \quad \sigma_y \end{aligned} \tag{5.3}$$

The first analyzed case foresees variable wind direction but always with the same intensity and profile shown in Figure 5.7. The probability the wind came from one direction is equal for each direction, it is a square probability. This because no information on the weather is known yet so there is no "preferential" wind direction known. The T-approach will change the way-point positions accordingly, as shown in Figure 5.25. The CEP is around 60 meters of radius at 50% of probability while it is around 150 meters of radius at 99% of probability, Figure 5.26 and Table 5.2. This is an acceptable result considering the very slow dynamic of large parafoil (the minimum turning radius in this case is of 200 meters). Also, it is a precision error compatible with the X-38 tests [4] and with the literature for large canopies [29].

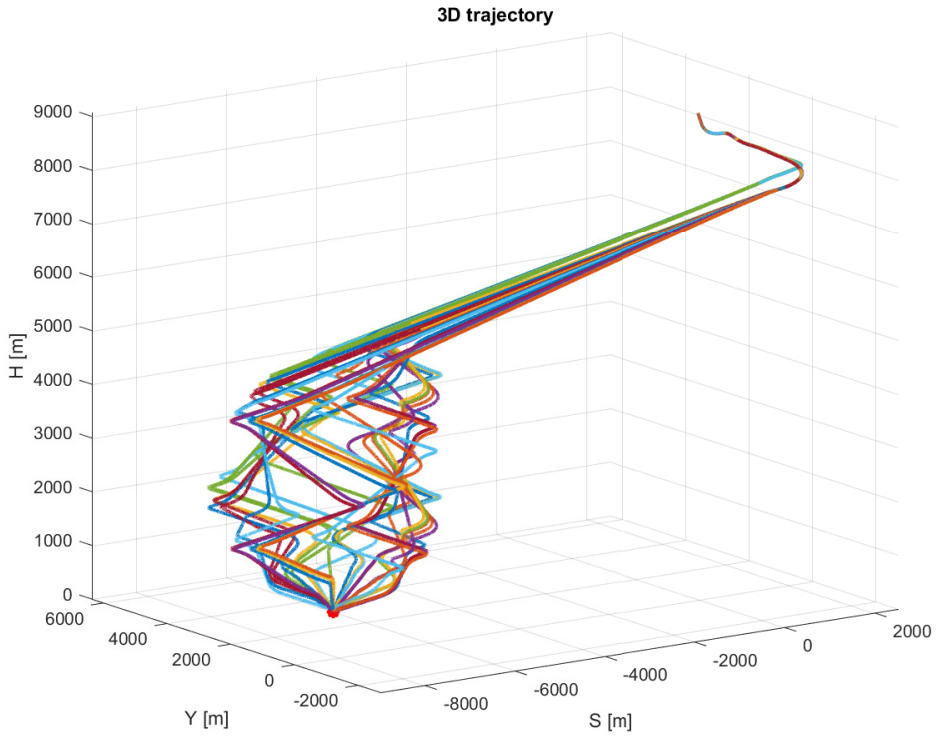

FIGURE 5.25: 30 different trajectories with different wind directions

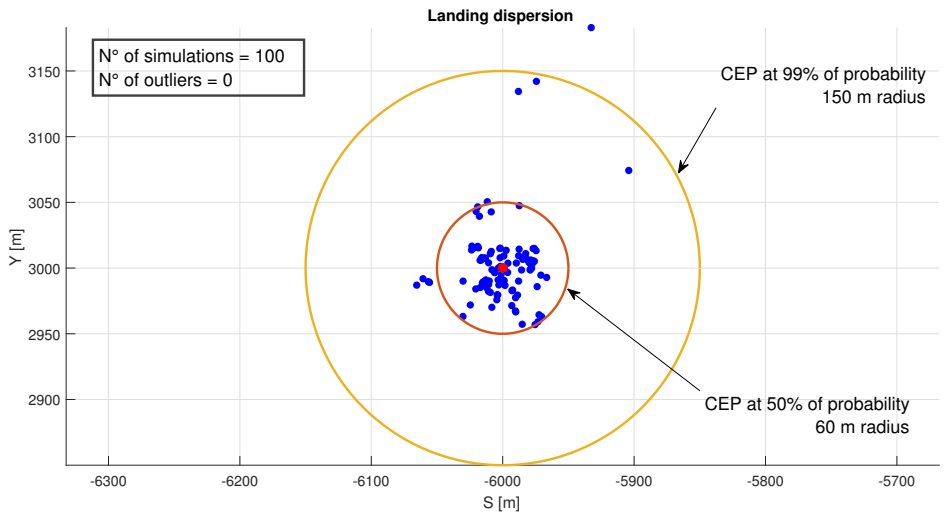

FIGURE 5.26: Landing dispersion for a T-based approach with different wind directions

The design requirement for the SpaceRider mission is a $CEP_{99\%}$ less or equal to 150 meters, so the GNC enables to satisfy this requirement.

An analysis is performed to look at the landing dispersion when the wind has a constant heading but its intensity changes. The wind intensity can assume values from 0 to 1.5 times the value of the wind profile reported in Figure 5.7 (a part from

the gust that is not considered here). These values should be tuned on the weather at the landing zone.

Results are shown in Figure 5.27 and Table 5.2. Computing the mean values of landing error as shown in Equation 5.1 it can be noted that along x there is a bias of 40.8 meters but this is negligible with respect to the magnitude of the standard deviation. Also, it would seem rotated with respect to the X-axis but, performing the computation to highlight any correlation between x-y data, it is clear that the latter conclusion is wrong. Indeed, if the value of $\overline{\rho}$ computed in Equation 5.4 is equal to 0, there is no correlation between x-y dispersion.

$$\overline{\rho} = \frac{\sum_{i=1}^{n}(x_i - \overline{x}_{LND})(x_i - \overline{x}_{LND})}{\sigma_x \sigma_y} = 5.7164e - 30 \approx 0 \tag{5.4}$$

Table 5.2 shows how in this case the landing dispersion has an elliptic shape.

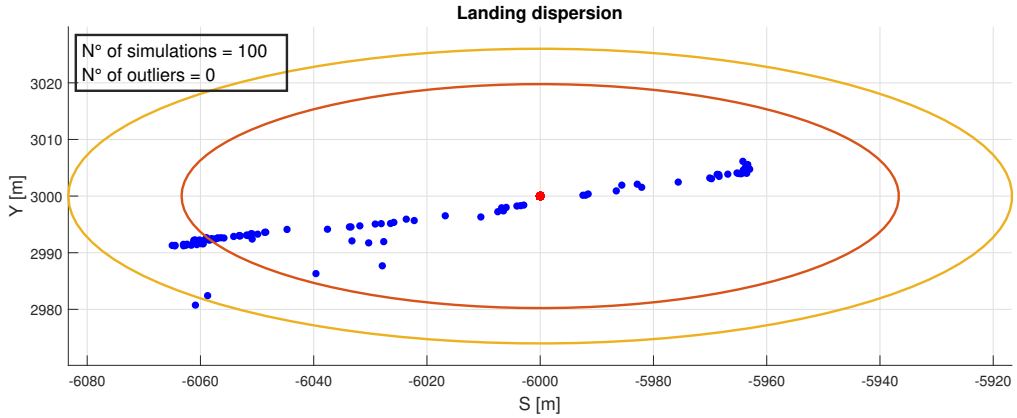

FIGURE 5.27: Landing dispersion for variable wind intensity

Figure 5.27 shows how the dispersion of the landing points is closer to the boundary than in the previous case. That is because wind is in some cases too strong to be compensated by the system with the altitude margin considered in Equation 4.2. Indeed, if the wind intensity is close to the maximum allowable, it is going to be close to $15m/s$ while the system flight velocity is around $20m/s$.

Another possibility is analyzed: T-approach is fixed in space and the wind varies randomly. This is a more realistic scenario, indeed if SpaceRider is going to land on a runway as an aircraft it can not change its approach path due to wind: the runway is of course fixed in space even if the wind moves.

Simulation results are shown in Figure 5.28 and Table 5.2. In addition, along x there is a bias of 20.8 meters but, as in the previous case, the bias is negligible.

It is interesting to note that, as shown in Table 5.2, the landing error dispersion has an elliptic shape with standard deviation values that are compatible with common runways dimensions. This demonstrates that for SpaceRider is feasible to land on a runway in the same fashion of an aircraft.

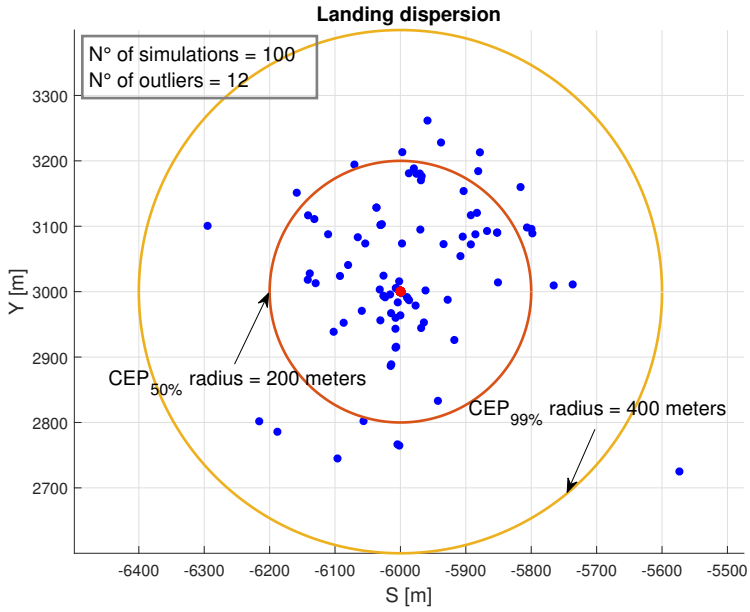

FIGURE 5.29: Landing dispersion in case of turbulence presence at the landing site

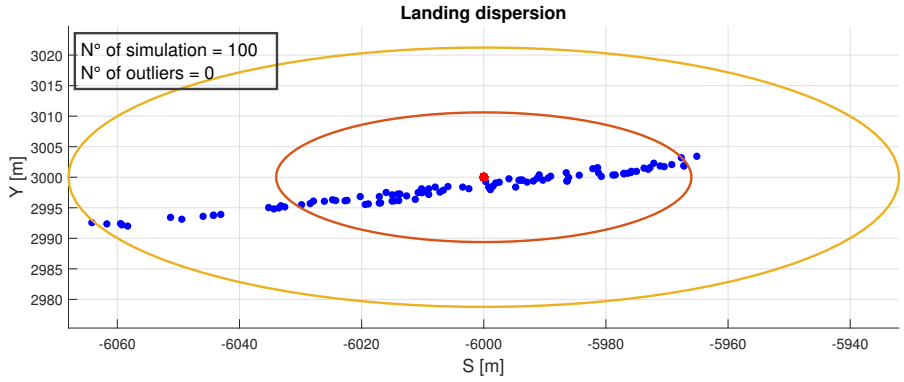

FIGURE 5.28: Landing dispersion for a runway-like landing with variable wind direction

An interesting case to be analyzed is the one with turbulence presence. The turbulence has been modeled with a simple white Gaussian noise [29] directly applied to the wind components, Figure 5.30. The standard deviation along each component is $1 m/s$, this value should be tuned on the expected weather conditions on the landing zone designed, in any case it seems to represent the worst case scenario: wind magnitude and direction vary in decimal of seconds. As shown in Figure 5.29 the dispersion from the desired position is increased with respect to the case of the linear wind. This is in line with literature: parafoil are very susceptible to turbulence. The degradation on the landing accuracy due to turbulence is such that the CEP value does not meet the design requirements.

Looking at Table 5.2 it is clear that the most critical parameters are turbulence intensity and wind intensity. They could lead to impose some operational limits to SpaceRider in order to meet the design requirements: above a determined value of wind and turbulence intensity the atmospheric re-entry should be delayed.

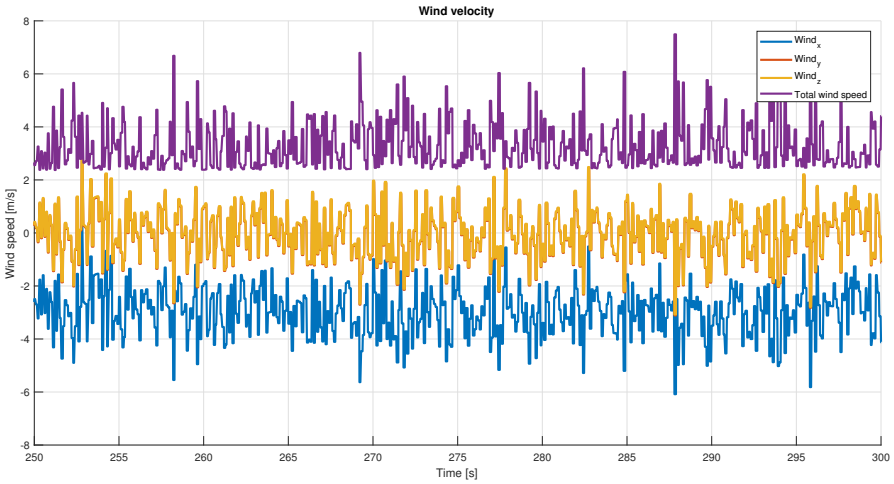

FIGURE 5.30: Turbulence modeled as white Gaussian noise

TABLE 5.2: Different CEP values depending on the operating conditions

	Variable wind direction		Variable wind intensity	
Probability value	50%	99%	50%	99%
CEP_x radius	60 m	150 m	63 m	83 m
CEP_y radius	60 m	150 m	20 m	26 m

	Fixed T with variable wind direction		Turbulence case	
Probability value	50%	99%	50%	99%
CEP_x radius	68 m	176 m	200 m	400 m
CEP_y radius	10 m	25 m	200 m	400 m

5.2.4 SpaceRider parafoil controlled flight

As stated in Section 4.2 the user has the possibility to make the system follow an input trajectory. This is particular useful to test the GNC algorithms to follow a 3D trajectory given by Thales Alenia Space, it could be representative of the real operational environment of SpaceRider. Figure 5.31 shows the 2D trajectory simulated, that is close to the given one (not displayed here for secrecy policy) within a distributed error of $200m$.

The simulation was performed with the nominal parafoil of SpaceRider: canopy surface $250m^2$ and the same aerodynamic characteristics reported in Tables 2.3 and 2.2.

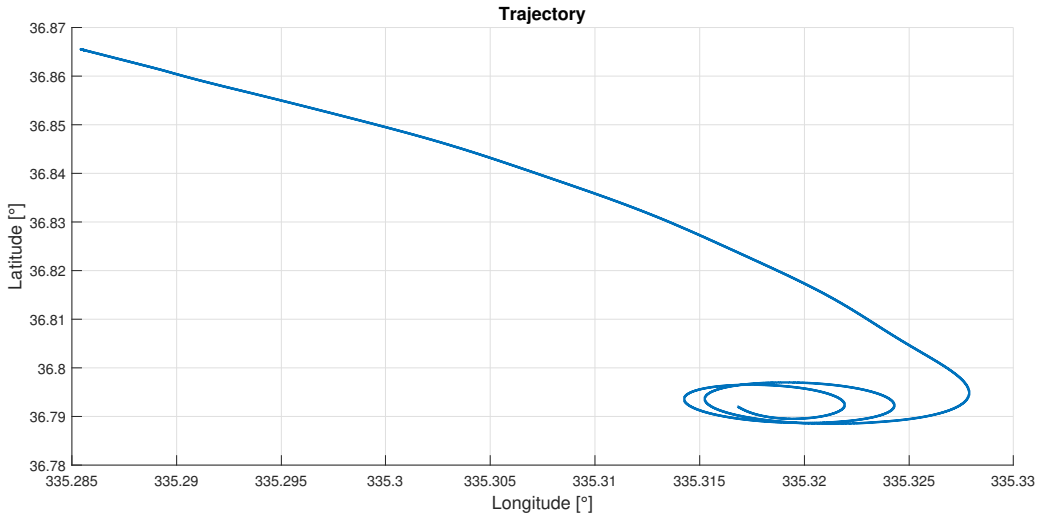

FIGURE 5.31: SpaceRider parafoil-only 2D trajectory

The rigging control is useful to follow a velocity profile, Figure 5.32. The distributed error is below 4%, it is an astonishing result because no parafoil aerodynamic property used to compute the reference trajectory was available.

Figure 5.33 represents a possible complete 3D trajectory of SpaceRider starting from the ballistic parachutes deployment and ending with the parafoil landing.

5.3 Alternative configurations

An alternative configuration to the parafoil landing gear is here analyzed for the SpaceRider mission, Figure 5.34. The MAR (Mid-Air Retrieval) strategy is exploited [9]. Avoiding the system to land by itself it does not only saves weight due to landing gear removal but it also simplifies the GNC system (loiter, terminal guidance and flare phases are discarded) allowing a canopy dimension reduction too.

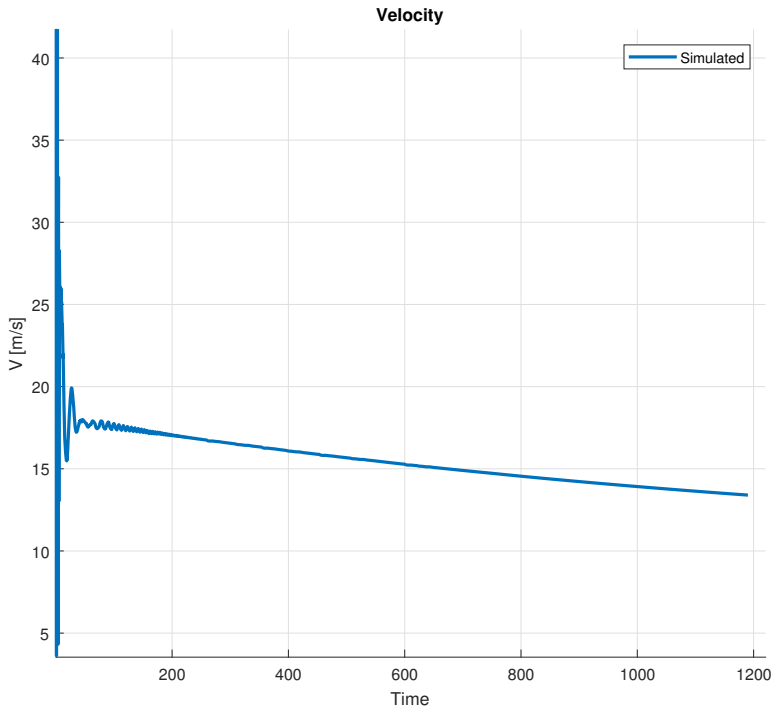

FIGURE 5.32: Velocity profile of the parafoil phase for SpaceRider

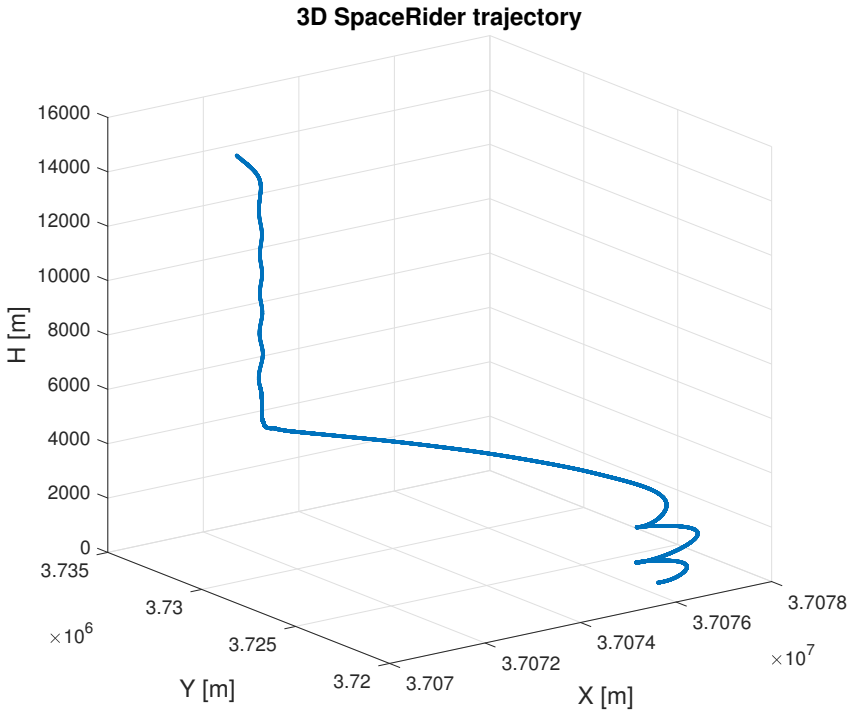

FIGURE 5.33: SpaceRider trajectory from supersonic ballistic parachute deployment to parafoil landing

FIGURE 5.34: MAR system concept of operations for the Space Rider vehicle [9]

The system design requirements are compatible with an helicopter flying at 3 km of altitude. It means:

- to have a system total velocity around 20 m/s at 3 km of altitude
- to have a vertical velocity around -9 m/s at 3 km of altitude
- a maximum deceleration at the opening of the parafoil less than 3g s

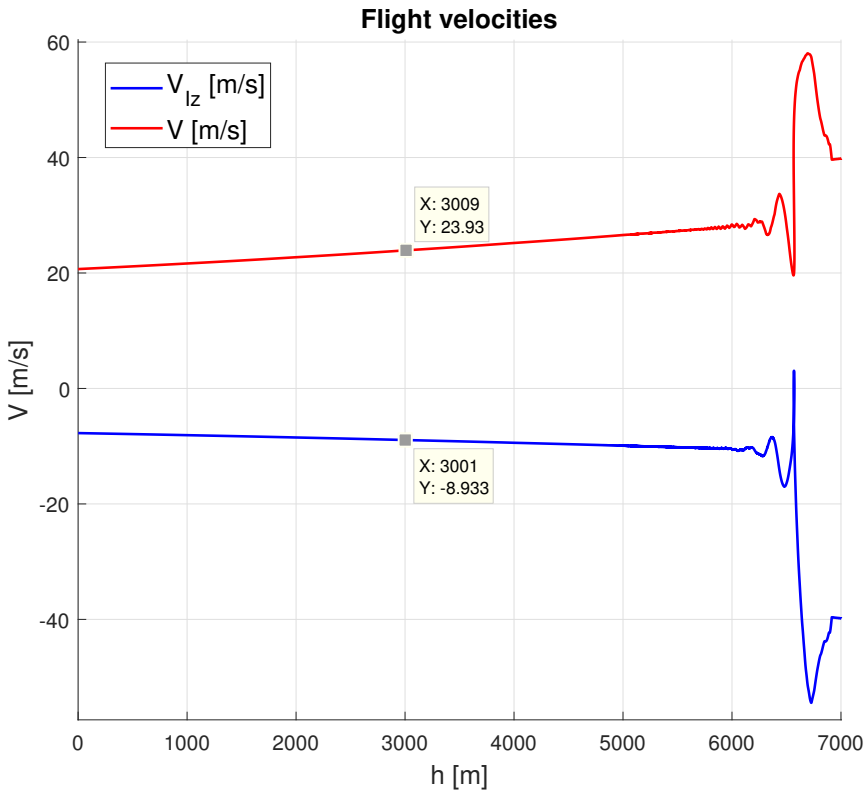

FIGURE 5.35: System velocities vs altitude

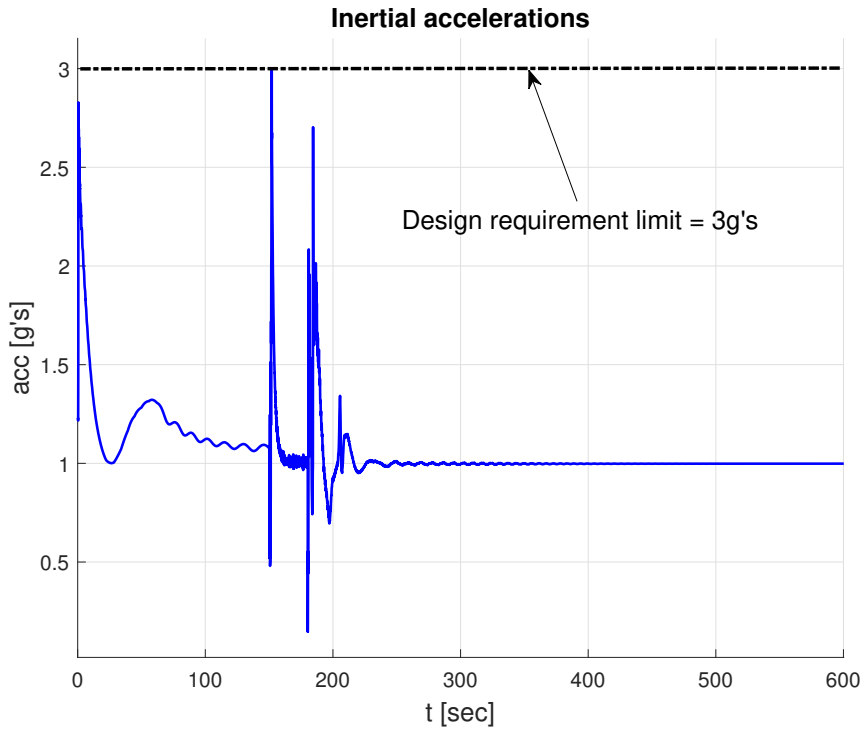

FIGURE 5.36: System decelerations for the entire flight envelope

As shown in Figures 5.35 and 5.36 the mission requirements are met with a

canopy surface of $100m^2$. Even if the subsonic ballistic parachute has around 0% of safety margin from the design requirement, a slightly bigger supersonic parachute should be considered to be safer. Figure 5.37 shows the canopy surface with respect to time, the $100m^2$ parafoil canopy allows a saving of 60% with respect to the nominal surface canopy of $250m^2$ for an aircraft landing-like configuration. This configuration would also save complexity for the GNC system: only the homing phase of the flight would be implemented without loitering, terminal guidance and flare phases.

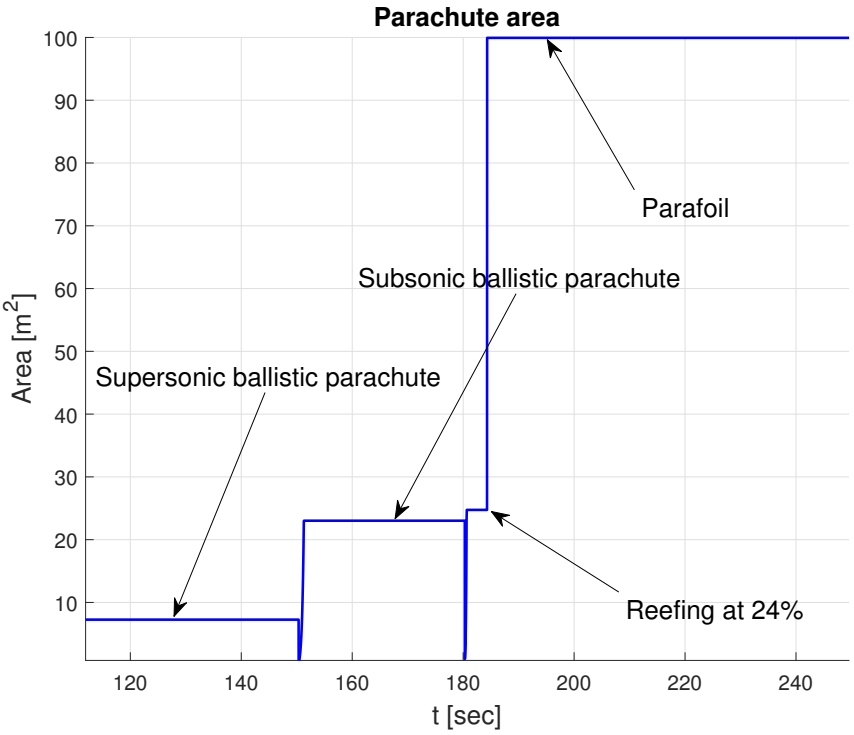

FIGURE 5.37: Parachutes and parafoil area

Evaluating the MAR configuration, the complexity of this configuration should be considered: the possible aerodynamic interactions between the rotor of the helicopter and the canopy of the parafoil before the system is hooked, the additional safety certifications needed if SpaceRider operates combined with a manned helicopter and so on.

Chapter 6

Conclusions & future work

6.1 Conclusions

The present work focused on two aspects that were not deeply analyzed by literature: the inflation analysis and the non-linear Lyapunov stable rigging control law applied to parafoil-payload systems.

The inflation analysis is usually treated with very simplified models aimed to find the correct peak value only (3 DoFs [13] [29]). Using a 12 DoFs model, it was showed a better representation of the inflation loads, representing correctly the experimental data of the X-38 drop test at the inflation, Section 3.2.2. Not only the peak load values were found very accurately but also the general trend of the loads was represented (i.e. the peak load is encountered at the pitch-down movement of the canopy Section 2.1.3). The presence of additional DoFs required the definition of some parameters during the analysis of inflation loads, such as C_{m_q} τ_0, that could affect results even of one order of magnitude, Section 3.2.2. The aerodynamic parameters most important are usually the ones related to the longitudinal motion of the system (C_L, C_D and C_m) must be accurately modeled and considered even at high angles of attack. The representation of the attitude though the quaternions is mandatory to avoid the Euler singularity.

The deep analysis of the inflation loads also showed how the highly dynamic and non-linear phase of parafoil inflation could be exploited to optimize the parafoil reefing technique, Section 5.1.1. This procedure helps to reduce as much as possible the inflation loads with a grid-search technique, using reefing percentage of the stage and time to full deployment as variables. The validity of this methodology was proven by the optimization of the X-38 reefing configuration that found out the values used by Pioneer.

As far as GNC is concerned, the innovation of the present work was the development of non-linear Lyapunov stable longitudinal control laws for the flight path angle control, especially in the terminal guidance phase. Usually PID controllers [29] are used but their linear functioning could lead to instabilities in a non- linear system, Section 5.2.2. The Lyapunov stability demonstration enables the control law to be independent from the parafoil-payload system at which it is applied. Also the non-linear stability proved to be useful when the system encounters a gust. The analytic demonstration, Section 4.3.2, is also a trail for further development of the control law that could be refined in order to meet requirements depending on the dynamic properties of the system and the desired performances.

In the frame of SpaceRider mission the multibody model will be used to design both the aerodynamic decelerator system and the GNC algorithms.

6.2 Future work

Any future work should be aware of the important assumptions made so far: the rigid body assumption for both the canopy and the payload, the limitations in the DoFs of the canopy during inflation, the considered reference system and the right-hand rule regard. Once the model assumptions and limits are clear some improvements can be done to the model itself.

Looking at the droptests report of the X-38 program [4] the percentage of non-nominal canopy aperture tests is striking. One of the biggest improvements in the model would be the possibility to model this kind of failures at dynamic level, even if the model is a rigid body one, and the introduction of random failures in simulations.

To design the GNC system it could be useful to translate the aileron deflection in length of the lines to be pulled. In this way the aileron deflection could be translated in work (knowing the force by the equations used to model the suspension lines) to obtain a certain control action on the system. The work to deflect ailerons can also be used to size the motors of the hinges in order to control the system trajectory.

An improvement of the landing accuracy could be gained if both the rigging control and symmetric ailerons deflection are exploited. Indeed the rigging control could be used to control the FpA profile while the symmetric ailerons deflection could be used to follow a predetermined velocity profile.

The Monte Carlo simulations showed in Section 5.2.3 should be performed with a more significant pool (more than a thousand of runs). For the SpaceRider application the parameters to be changed and their probable distribution should be tuned on the operational scenario identified as nominal: the wind direction and intensity should have a probable distribution that is representative of the weather conditions experienced at the landing zone designated.

The use of gains in the control laws, Equations 4.8 and 4.9, can be considered an additional and useful degree of freedom in the hands of an expert GNC engineer. But, to reduce the parameters to be defined by the user and also to have a good performance of the GNC system, the system could be linearized in the around of the actual states and then a Riccati equation solved to find the optimal gains for the fitness function chosen.

As far as the inflation analysis is concerned, a better definition of the τ_0 and C_{m_q} should be performed, via experiments and/or CFD analysis. Indeed the literature gives a wide range of possible values but these values, changing from parafoil to parafoil, affect heavily the obtained results. The C_{m_q} value for example can assume a value from -6.1 [24] to 0 [26].

In any case before using the model in the real mission environment it should be noted that validation showed in Chapter 3 is not enough. Mainly because most of the comparison was performed with lower DoFs model. A drop test to validate both the GNC algorithms and the loads predicted is therefore mandatory.

Appendix A

Lyapunov stability demonstration of symmetric ailerons deflection

Similar to the rigging angle control, the symmetric ailerons deflection is intended to adjust the FpA too. So it is quite reasonable to assume the same Lyapunov function, 4.10. The difference from the previous case will be on the interaction between the control law (Equation 4.9) and the condition on the Lyapunov derivative.

Equation 4.12 gives the Lyapunov function derivative. Knowing that γ is related to lift-to-drag ratio, Equation 4.6, the term $\dot{\gamma}$ in Equation 4.12 can be written as Equation A.1.

$$\dot{\gamma} = -\frac{1}{(tg(\frac{L}{D}))^2} \quad \frac{1}{cos^2(\frac{L}{D})} \quad \frac{d}{dt}\left(\frac{L}{D}\right) \tag{A.1}$$

The time derivative of the lift-to-drag ratio can be written as Equation A.2.

$$\frac{d}{dt}\left(\frac{L}{D}\right) = \frac{D\dot{L} - L\dot{D}}{D^2} \tag{A.2}$$

Lift and drag variations in time could be supposed to be mainly connected to their variation of aerodynamic proprieties due to ailerons deflection, variation of speed will take place too but this is considered negligible with respect to the C_L and C_D variations.

$$\begin{aligned} \dot{L} &= C_{L_{\delta_s}}\dot{\delta}_s \\ \dot{D} &= C_{D_{\delta_s}}\dot{\delta}_s \end{aligned} \tag{A.3}$$

Thus the derivative of the Lyapunov function can be rewritten as Equation A.4. Where a_{coeff} represents all quantities that are positive because they are powers of 2, such as $-\frac{1}{(tg(\frac{L}{D}))^2} \quad \frac{1}{cos^2(\frac{L}{D})}$.

$$\dot{V} = a_{coeff}\dot{\delta}_s(\gamma - \gamma_{des})\frac{DC_{L_{\delta_s}} - LC_{D_{\delta_s}}}{D^2} \tag{A.4}$$

As already mentioned the FpA control can act only when $\gamma_{des} < \gamma$ (they are both negative), so $\gamma - \gamma_{des}$ is more than 0, therefore the definition of the control action $\dot{\delta}$ reported in Equation 4.9 guarantees the product $\dot{\delta}_s(\gamma - \gamma_{des})$ to be major than 0.

The term enabling the Lyapunov stability is $DC_{L_{\delta_s}} - LC_{D_{\delta_s}} < 0$, it implies the conditions reported in Equation A.5. This condition is automatically satisfied by the aerodynamic coefficients from Table 4.3 but it is usually a general satisfied condition, because the symmetric ailerons deflection is going to diminish the lift-to-drag ratio but also to increase the AoA. The increment of AoA value will increase the lift-to-drag ratio, if linear aerodynamic assumption is valid. Considering this, the decrease

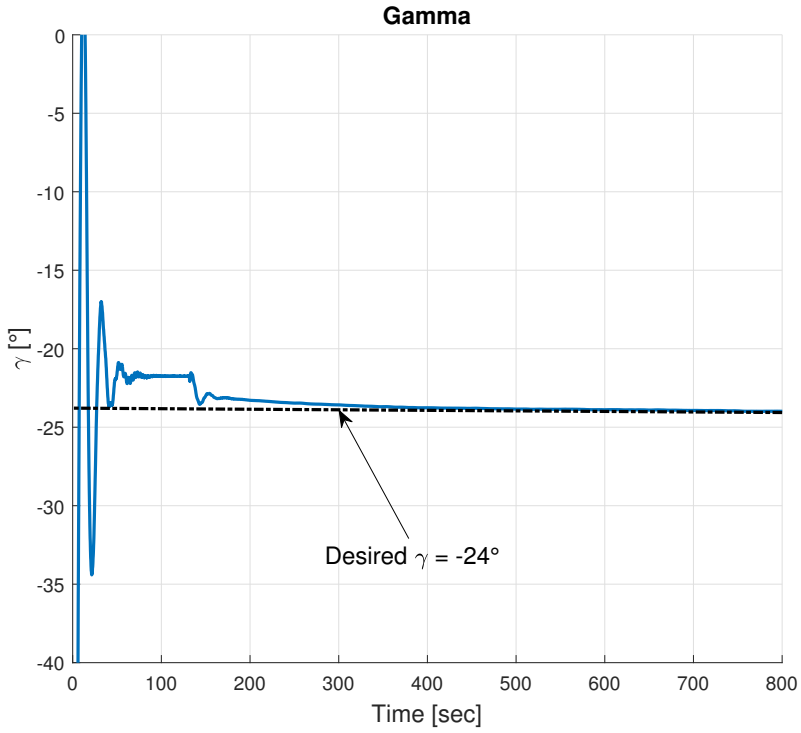

FIGURE A.1: Variation of the FpA due to symmetric ailerons control

of lift-to-drag ratio will be always lower than the ratio of their aerodynamic control derivatives.

$$\frac{C_{L_{\delta_s}}}{C_{D_{\delta_s}}} < \frac{L}{D} \tag{A.5}$$

Figures from A.1 to A.2 show how the symmetric ailerons deflection can be used to control the FpA in the same way of the rigging angle with the control law Equation 4.9.

It can be noted how the velocity of the system decreases, this is the reason why during the flare maneuver a full symmetric aileron deflection is commanded.

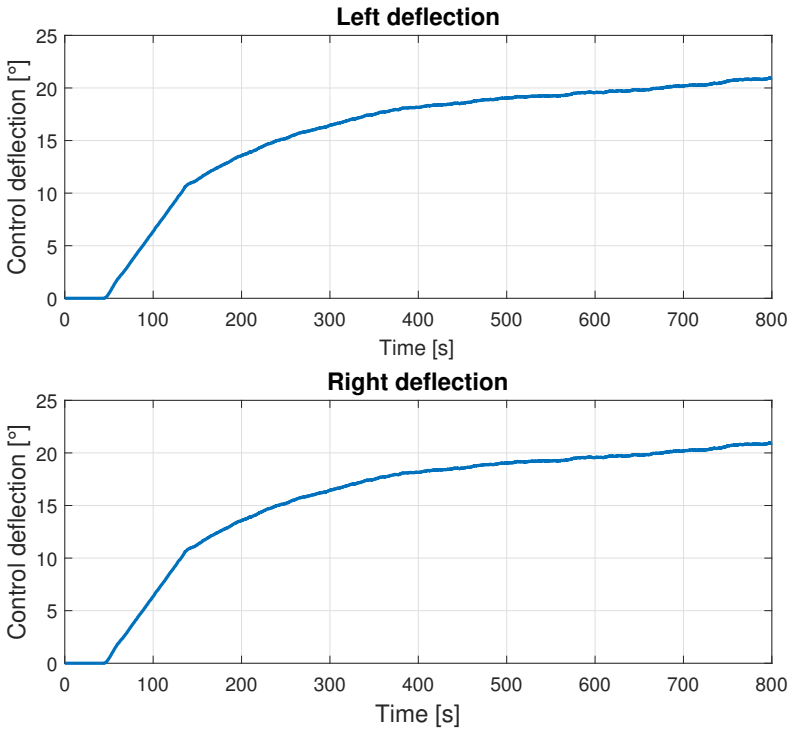

FIGURE A.2: Symmetric ailerons control

Appendix B

Flare

The flare maneuver is initialized few dozen of meters above the ground. It is a very dynamic maneuver: its tuning will change if the dynamic properties of the system change.

The aim of this last control stage is to reduce as much as possible the touch-down velocity, especially the vertical one (that must be dissipated by landing gears or skids). In order to achieve the desired condition an open loop strategy is implemented: the rigging control is set to zero and the ailerons deflection is imposed to be symmetric at 90 degrees.

The symmetric deflection of ailerons aims to reduce the total velocity, the way it will affect the FpA will depend on the values of $C_{D_{\delta_s}}$ and $C_{L_{\delta_s}}$. The rigging control instead is set to 0 in order to have the system not to accelerate and also not to increment the FpA. All that would lead to higher values of vertical velocity, Section 5.2.1.

As shown in Figures from B.1 to B.4, the Terminal Guidance increases the γ with the rigging control because the system is too high with respect to the landing zone. As soon as the flare is initialized, when the system is lower than 75 meters, the velocity decreases and also the absolute value of the FpA. This means that not only the overall landing velocity is lower but, most importantly, the vertical velocity is lowered.

If symmetric ailerons deflection would not have been commanded, the system would have landed at 24.5 m/s (with rigging control still active) or 20 m/s (with rigging angle set to 0). It means a velocity diminish of 25% and 8% respectively, without any flight hardware modification.

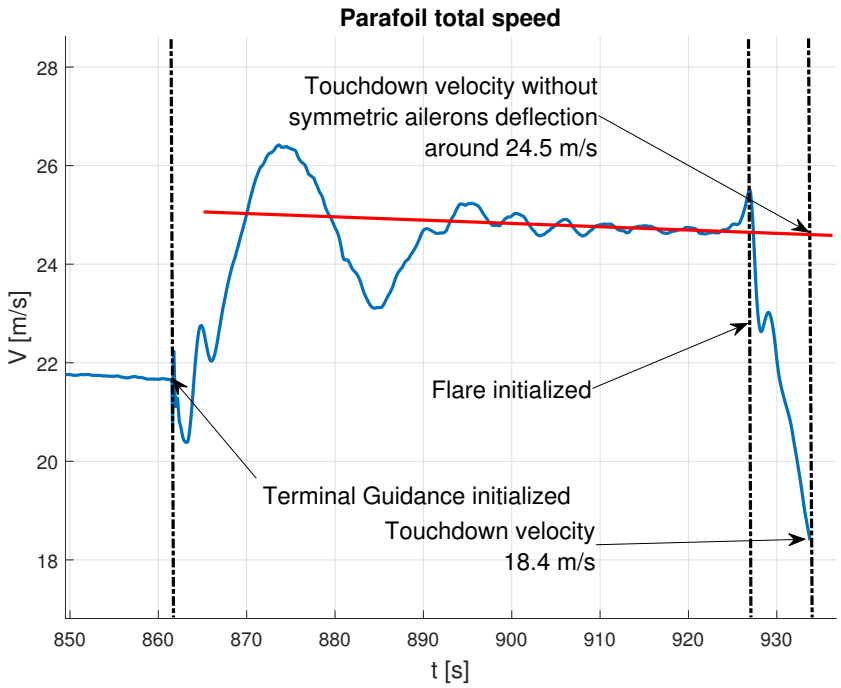

FIGURE B.1: Terminal Guidance and Flare phases velocity change

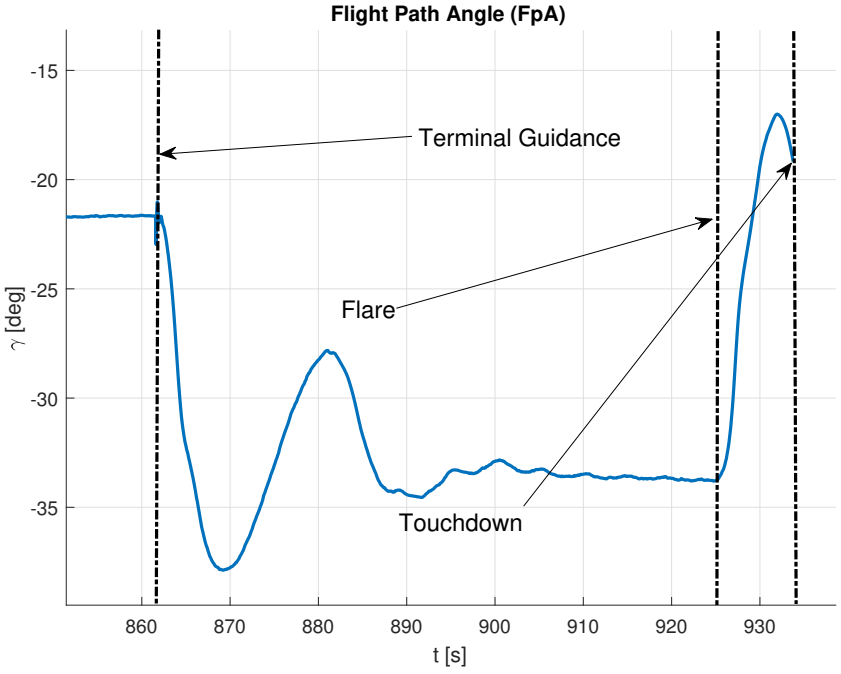

FIGURE B.2: Terminal Guidance and Flare phases FpA change

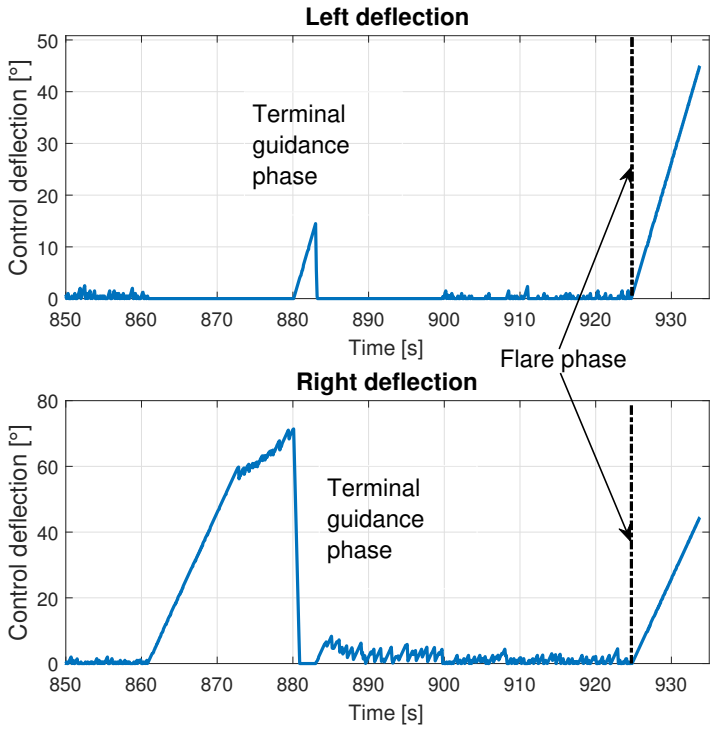

FIGURE B.3: Terminal Guidance and Flare phases ailerons deflection

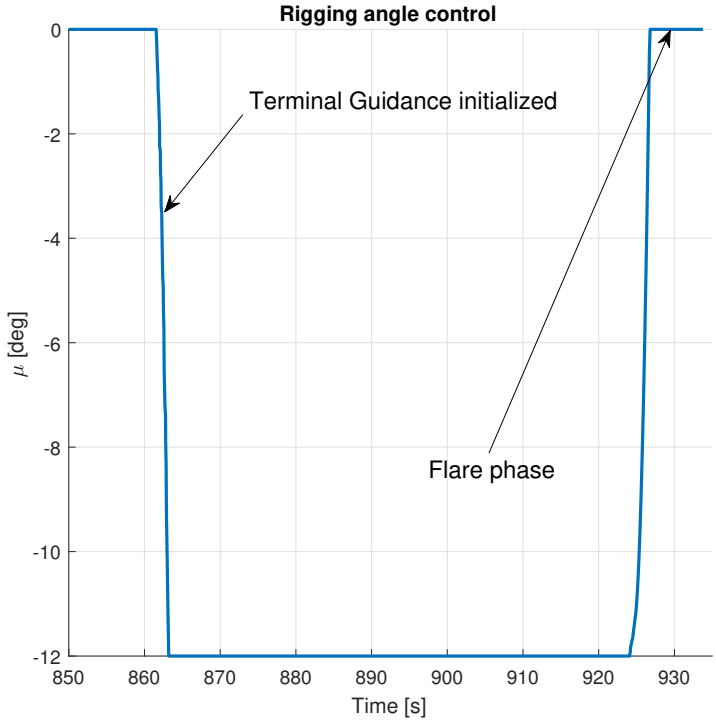

FIGURE B.4: Terminal Guidance and Flare phases rigging angle values

Appendix C

Design features

Being the model very complex (12 DoFs), it is mainly suited for validation purpose. But, in order to allow an higher flexibility and the exploitation of the model during the design of the parafoil, some semi-empirical models are introduced. Semi-empirical models are the ones reported by O. Yakimenko [29] and they can be used to size the main parafoil geometrical properties (surface, aspect ratio and arch radius) relating them to the aerodynamic properties.

With this procedure it can be possible to decide a parafoil airfoil on the base of its flight qualities. Indeed the input data needed for the computations are:

- the angle of attack (coming from the dynamic simulation)
- the aspect ratio of the parafoil wing (AR)
- the $C_{L_\alpha}^{2D}$ of the airfoil section
- the angle of attack at which the airfoil generates zero lift α_0
- the semi-aperture angle of the canopy ϵ_0

Starting from the quantities listed above, the aerodynamic properties of the full 3D parafoil can be computed with Equations from C.1 to C.7.

$$\begin{aligned} k &= AR\pi(C_{L_\alpha}^{2D})^{-1} \\ k_1 &= \frac{\sqrt{k^2+1}+1}{\sqrt{k^2+4}+2} \\ k_2 &= \frac{\sqrt{k^2+4}-1}{\sqrt{k^2+1}+1} \end{aligned} \tag{C.1}$$

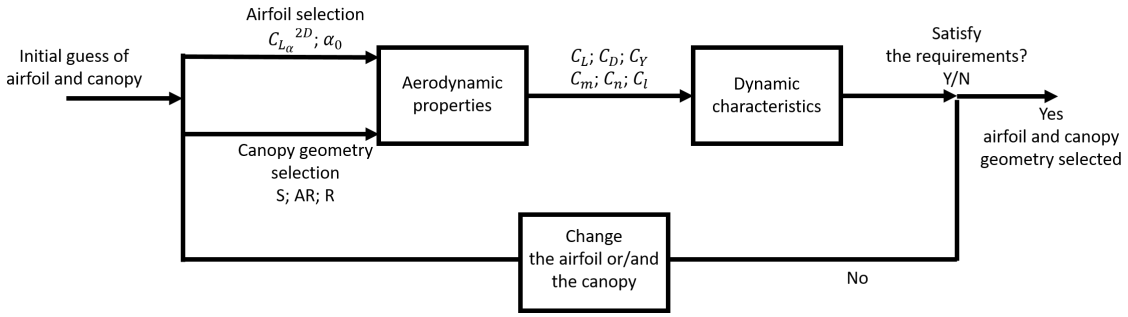

FIGURE C.1: Design process of the parafoil aerodynamic properties

$$C_{L_\alpha} = \frac{\pi AR C_{L_\alpha}^{2D}}{\sqrt{(\pi AR)^2 + (C_{L_\alpha}^{2D})^2} + C_{L_\alpha}^{2D}}$$
$$C_L = C_{L_\alpha}(\alpha cos(\epsilon/2) - \alpha_0) cos(\epsilon/2) \tag{C.2}$$

$$C_{D_{induced}} = \frac{C_{L_\alpha}^2}{e\pi AR}(\alpha cos(\epsilon/2) - \alpha_0)^2$$
$$C_D = C_{D_0} + C_{D_{induced}} \tag{C.3}$$

$$C_{m_q} = -\frac{C_{L_\alpha}}{12}(cos(\epsilon/2))^2$$
$$C_m = C_{m_q}\frac{qc}{2V} \tag{C.4}$$

$$C_{Y_\beta} = -C_{L_\alpha}k_1\frac{\epsilon sin(\epsilon)}{4} - C_{D_0}\frac{1 + 2cos(\epsilon)}{3}$$
$$C_{Y_p} = C_{L_\alpha}k_1\frac{sin(\epsilon)}{4}$$
$$C_{Y_r} = \frac{1}{2}C_{L_\alpha}(sin(\epsilon)\alpha_0 - 2sin(\epsilon)(cos(\epsilon))^2\alpha) \tag{C.5}$$
$$C_Y = C_{Y_\beta}\beta + C_{Y_p}\frac{pb}{2V} + C_{Y_r}\frac{rb}{2V}$$

$$C_{n_\beta} = \frac{1}{8}\epsilon C_{L_\alpha}k_1k_2(sin(\epsilon)\alpha_0 - 2sin(3\epsilon/2)\alpha)$$
$$C_{n_r} = -\frac{C_{D_0}}{3}\left(1 - \frac{1}{5}\epsilon^2\right) + \frac{(C_{L_\alpha})^2}{\pi AR}\left(\frac{1}{2} - \frac{\epsilon}{24}\alpha_0^2\right) + C_{L_\alpha}\frac{k_1\epsilon^2}{24\quad AR^2}$$
$$+ \left(\frac{(C_{L_\alpha})^2}{\pi AR}\left(4 - \frac{7}{12}\epsilon^2\right) - C_{L_\alpha}\left(1 - \frac{5}{12}\epsilon^2\right)\frac{\alpha_0}{4}\right)\alpha \tag{C.6}$$
$$C_{n_p} = \frac{1}{8\epsilon}C_{L_\alpha}k_1k_2(sin(\epsilon)\alpha_0 - 2sin(3\epsilon/2)\alpha)$$
$$C_n = C_{n_\beta}\beta + C_{n_p}\frac{pb}{2V} + C_{n_r}\frac{rb}{2V}$$

$$C_{l_\beta} = C_{L_\alpha}k_1\frac{sin(\epsilon)}{8}$$
$$C_{l_r} = -\frac{1}{4\epsilon}C_{L_\alpha}(sin(\epsilon)\alpha_0 - 2sin(\epsilon/2)(cos(\epsilon/2))^2\alpha) \tag{C.7}$$
$$C_{l_p} = -C_{L_\alpha}k_1\frac{sin(\epsilon)}{8\epsilon}$$
$$C_l = C_{l_\beta}\beta + C_{l_p}\frac{pb}{2V} + C_{l_r}\frac{rb}{2V}$$

In this way it is possible to tune the inputs to have the desired flight qualities of the system: the parafoil airfoil and the canopy geometrical properties (AR,S,ϵ_0) are designed. The logic flow chart of the design process is shown in Figure C.1.

Examples of C_L and C_D with respect to the angle of attack found with these model are given in Figure C.2 and C.3. It worths noting that even if C_L at high angle of attack has a very high value, in practice that value is never met for the no-lift approximation during inflation Section 2.1.3.

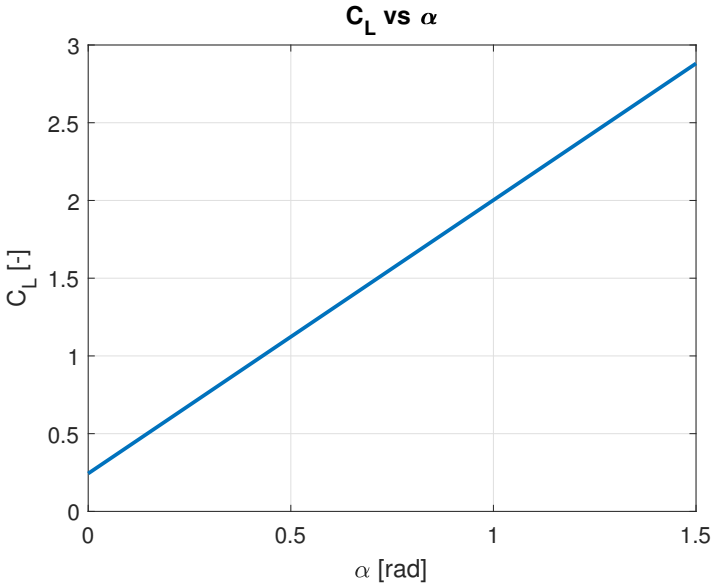

FIGURE C.2: C_L vs α computed with the models presented and the data in Table C.1

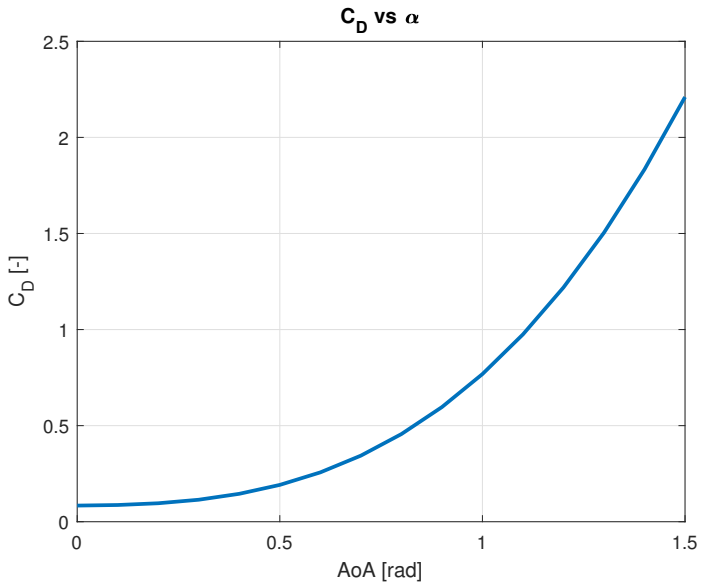

FIGURE C.3: C_D vs α computed with the models presented and the data in Table C.1

TABLE C.1: Canopy and airfoil data used for the model test

Quantity	Value
Canopy surface	100 m^2
Aspect ratio (AR)	3
Canopy radius (R)	0.6 b (span)
$C_{L_\alpha}^{2D}$	π
α_0	-7 deg
C_{D_0}	0.084
e	0.8

Bibliography

[1] Giulio Avanzini, Giorgio Guglieri, and Alberto Torasso. Multibody analysis of terminal phase for a reentry vehicle: a comparative study. *Journal of Aircraft*, 49(6):1940–1952, 2012.

[2] Alessandro Balossino, Luciano Battocchio, Matteo Giacci, Giuseppe Giudotti, Giuseppe Rufolo, Angelo Denaro, and Nicola Paletta. Conceptual design of the descent subsystem for the safe atmospheric re-entry flight of space rider. *7TH European Conference for Aeronautics and Space Sciences (EUCASS)*, 2017.

[3] Timothy M Barrows. Apparent mass of parafoils with spanwise camber. *Journal of Aircraft*, 39(3):445–451, 2002.

[4] Thomas Bennett and Roy Fox. Design, development & flight testing of the nasa x-38 7500 ft2 parafoil recovery system. In *17th AIAA Aerodynamic Decelerator Systems Technology Conference and Seminar*, page 2107, 2003.

[5] Thomas Bennett and Roy Fox. Design, development and flight-testing of the us army 4200 ft2 parafoil recovery system. In *18th AIAA Aerodynamic Decelerator Systems Technology Conference and Seminar*, page 1628, 2005.

[6] Van der Kolf Gideon. *Flight control system for an autonomous parafoil*. PhD thesis, Stellenbosch: Stellenbosch University, 2013.

[7] Lester E Dubins. On curves of minimal length with a constraint on average curvature, and with prescribed initial and terminal positions and tangents. *American Journal of mathematics*, 79(3):497–516, 1957.

[8] Gonzalez Garcia Esteban, G. Sacco Carlos, Ortega Enrique, and Flores Roberto. Development of computational tools for analysis and evaluation of autonomous parafoil systems. 2010.

[9] A. Godfrey. Space rider - developing esa's autonomous space vehicle capability. 2017.

[10] Kowaleczko Grzegorz. Apparent masses and inertia moments of the parafoil. *Journal of Theoretical and Applied Mechanics*, 52, 2014.

[11] Thomas Jann. Advanced features for autonomous parafoil guidance, navigation and control. In *18th AIAA Aerodynamic Decelerator Systems Technology Conference and Seminar*, page 1642, 2005.

[12] Chun Li, Hai-shan Teng, Yan-hua Zhu, Wan-song Jiang, Peng Zhou, Wei Huang, Xu Chen, and Jing-lei Liu. Design and simulation for large parafoil fix line object homing algorithm. *Journal of Central South University*, 23(9):2276–2283, 2016.

[13] J.Stephen Lingard. Precision aerial delivery seminar. 1995.

[14] P Lissaman and Glen Brown. Apparent mass effects on parafoil dynamics. In *Aerospace Design Conference*, page 1236, 1993.

[15] Chris Madsen, Ronald Sostaric, and Chris Cerimele. Flight performance, aerodynamics, and simulation development for the x-38 parafoil test program. In *17th AIAA Aerodynamic Decelerator Systems Technology Conference and Seminar*, page 2108, 2003.

[16] Erwin Mooij, Quirien Wijnands, and Bart Schat. 9 dof parafoil/payload simulator development and validation. In *AIAA Modeling and Simulation Technologies Conference and Exhibit*, page 5459, 2003.

[17] Sanghyuk Park, John Deyst, and Jonathan P How. Performance and lyapunov stability of a nonlinear path following guidance method. *Journal of Guidance, Control, and Dynamics*, 30(6):1718–1728, 2007.

[18] Branden J Rademacher, Ping Lu, Alan L Strahan, and Christopher J Cerimele. In-flight trajectory planning and guidance for autonomous parafoils. *Journal of guidance, control, and dynamics*, 32(6):1697–1712, 2009.

[19] Chris Ranier. The analysis and modeling of the deployment of nasa's x-38 parafoil. 2001.

[20] Edward J Scheuermann. *Autonomous control of parafoil and payload systems using upper surface canopy spoilers*. PhD thesis, Georgia Institute of Technology, 2015.

[21] Nathan Slegers and Mark Costello. On the use of rigging angle and canopy tilt for control of a parafoil and payload system. In *AIAA Atmospheric Flight Mechanics Conference and Exhibit*, page 5609, 2003.

[22] Nathan J Slegers. Dynamic modeling, control aspects and model predictive control of a parafoil and payload system. 2004.

[23] Chiara Toglia and Marilena Vendittelli. Modeling and motion analysis of autonomous paragliders. *Department of computer and system sciences Antonio Ruberti technical reports*, 2(5), 2010.

[24] Damian Toohey. Development of a small parafoil vehicle for precision delivery. Master's thesis, Massachusetts Institute of Technology, 2005.

[25] Michael Ward and Mark Costello. Adaptive glide slope control for parafoil and payload aircraft. *Journal of Guidance, Control, and Dynamics*, 36(4):1019–1034, 2013.

[26] Michael Ward, Sean Culpepper, and Mark Costello. Parafoil control using payload weight shift. *Journal of Aircraft*, 51(1):204–215, 2014.

[27] Michael Ward, Alek Gavrilovski, and Mark Costello. Glide slope control authority for parafoil canopies with variable incidence angle. *Journal of Aircraft*, 50(5):1504–1513, 2013.

[28] Wim Wegereef, Franciscus Doejaaren, Simon Benolol, and Jose Francisco Zapirain. Fastwing cl flight tests with a high-glide ram-air parachute for 6000kg payloads. In *21st AIAA Aerodynamic Decelerator Systems Technology Conference and Seminar*, page 2596, 2011.

[29] Oleg Yakimenko. Precision aerial delivery systems: Modeling, dynamics, and control. *American Institute of Aeronautics and Astronautics*, 248(1244):1579–1583, 2017.